OBSERVATIONS OF INTERMEDIATE MASS STARS AND THEIR CIRCUMSTELLAR ENVIRONMENTS WITH NULLING INTERFEROMETRY

by

Wilson Michael Liu

A Dissertation Submitted to the Faculty of the

DEPARTMENT OF ASTRONOMY

In Partial Fulfillment of the Requirements
For the Degree of

DOCTOR OF PHILOSOPHY

In the Graduate College

THE UNIVERSITY OF ARIZONA

2007

THE UNIVERSITY OF ARIZONA
GRADUATE COLLEGE

As members of the Dissertation Committee, we certify that we have read the dissertation prepared by Wilson Michael Liu entitled "Observations of Intermediate Mass Stars and Their Circumstellar Environments with Nulling Interferometry" and recommend that it be accepted as fulfilling the dissertation requirement for the Degree of Doctor of Philosophy.

_____ Date: 29 May 2007
Philip Hinz

_____ Date: 29 May 2007
Donald McCarthy

_____ Date: 29 May 2007
Michael R. Meyer

_____ Date: 29 May 2007
Joan Najita

Final approval and acceptance of this dissertation is contingent upon the candidate's submission of the final copies of the dissertation to the Graduate College.

I hereby certify that I have read this dissertation prepared under my direction and recommend that it be accepted as fulfilling the dissertation requirement.

_____ Date: 29 May 2007
Dissertation Director: Philip Hinz

STATEMENT BY AUTHOR

This dissertation has been submitted in partial fulfillment of requirements for an advanced degree at The University of Arizona and is deposited in the University Library to be made available to borrowers under rules of the Library.

Brief quotations from this dissertation are allowable without special permission, provided that accurate acknowledgment of source is made. Requests for permission for extended quotation from or reproduction of this manuscript in whole or in part may be granted by the head of the major department or the Dean of the Graduate College when in his or her judgment the proposed use of the material is in the interests of scholarship. In all other instances, however, permission must be obtained from the author.

SIGNED: Wilson Michael Liu

ACKNOWLEDGMENTS

One does not make it this far in grad school (or in life) without help from others.

I thank my collaborators and colleagues, without whom I would not have been able to complete this work. First and foremost, I thank my advisor, Phil Hinz, who helped guide me through all the ins and outs of this dissertation. Others provided me with assistance and valuable scientific discussion as well: Michael Meyer, Eric Mamajek and Bill Hoffmann. I am especially grateful to Don McCarthy for his words of encouragement and advice, and being a mentor throughout my years in graduate school. Thanks also to another member of my committee, Joan Najita, who has provided insights and advice in parts of this dissertation. I am grateful to Scott Kenyon, who provided some results from his debris disk models. Finally, I thank the Michelson Graduate Student Fellowship Program, which supported me through much of this project.

My observations would not have been completed without valuable support from members of the MMT adaptive optics group who supported and ran the AO system during observations. This group includes Doug Miller, Guido Brusa, Matt Kenworthy, Francois Wildi, and Vidhya Vaitheeswaran. For technical support of the BLINC-MIRAC instrument during runs I thank Brian Duffy and Andy Breuninger. I also would like to thank the telescope operators at the MMT, Ale Milone, Mike Alegria, and John McAfee.

My moral support came from my close friends throughout my years here at Steward Observatory: Andy Marble (and the entire Marble family), Kris Eriksen, Jenn Donley, Joannah Hinz, Nick Siegler, Jane Rigby, Andrea Leistra, Casey Meakin, and Yeechi Chen. Your kind words and ability to listen are deeply appreciated.

I wish to thank the Department of Physics and Astronomy at Dartmouth College, and particulary Professors Brian Chaboyer and Rick Watkins. Your guidance in the first couple years of my career was invaluable. The atmosphere in the department at Dartmouth was positive, encouraging, and nurturing, qualities not found in abundance in big departments at large research universities. During my undergraduate studies, I built up the enthusiasm for astronomy that was necessary to make it through grad school.

Last but not least, I thank my family for their love and unwavering support in everything I do. Most of all, my loving wife, Ana, who always believes in me even when I don't.

Dedication

To Ana.

Table of Contents

List of Figures

List of Tables

ABSTRACT

In this dissertation, I present nulling interferometric observations of intermediate mass stars and their circumstellar environments. The observations constrain physical processes with regard to the evolution of circumstellar dust in primordial disks, as well as debris disks in main sequence objects. Observations were made in the N-band (near 10 μm) which traces primarily thermal emission from warm dust, and take advantage of the high spatial resolution afforded by nulling interferometry. The first part of the dissertation includes observations of 13 Herbig Ae stars using the BLINC-MIRAC instrument on the MMT and Magellan I (Baade) Telescopes. Three of the 13 objects were spatially resolved (AB Aurigae, HD 100546, and HD 179218). It appears that inferred disk sizes and limits are correlated to the submillimeter SED slope and fractional infrared luminosity of the objects. This implies that disk flaring may have an effect on the resolvability. Further examination of the results reveals evidence for a large inner gap in the HD 100546 disk, possibly resulting in the large inferred disk size. The second part of the dissertation includes observations of six nearby main sequence targets, all of which show no evidence for a positive detection of warm debris. Using a scaled up model of solar zodiacal emission, upper limits on dust density range from 500 to 10^4 Zody (1 Zody = the density of our own solar zodiacal cloud) depending on the particular star, which corresponds to limits of 10^{-6} to $5 \times 10^{-5} M_{\oplus}$ of micron-sized dust. The well studied nature of the debris disks around Vega, ϵ Eridani, and ζ Leporis allows us to place these observations in the context of previous studies at other wavelengths to determine the physical processes responsible for shaping the debris disk in these systems.

CHAPTER 1

INTRODUCTION

Although a general picture of star and planet formation has been developed in recent years, many unanswered questions remain. The earliest stages of the process involve the collapse of dense molecular clouds into protostellar cores and subsequently protostars (Andre et al., 2000, and ref. therein). During the pre-main sequence (PMS) lifetime of a star, it is surrounded by large amounts of material, both gas and dust. Recent studies have shown that the distribution of this material is in the form of a circumstellar disk surrounding objects with masses less than about 5 M_* (Natta et al., 2000). The evolution of gas and dust in these disks is still an area of intense study. For example, it is during the PMS phase, which is thought to last at most 30 Myr for a solar-type star, that the formation of giant planets is believed to occur. It has not been unambiguously established how these giant planets form, and different mechanisms (e.g., gravitational fragmentation of the disk, core accretion, etc.) have been proposed (Wuchterl et al., 2000), each with their own timescales and observational predictions. During this time, dusty material may begin to gravitationally agglomerate, forming larger solid bodies, a foundation for terrestrial planets or the cores of giant planets. The presence of planets will, in turn, affect the distribution of material in the disk, opening gaps and creating substructure. Another question related to primordial disk evolution is how these disks are eventually dispersed as the star finishes its PMS phase. Many mechanisms have been hypothesized, from accretion onto the central star, to photoevaporation, to stellar encounters (Hollenbach et al., 2000), again each with different timescales and qualitative differences (e.g., inside-out or outside-in clearing). A clear understanding of this stage of stellar evolution is necessary,

as it forms the foundation for the system that will develop as the star matures.

When stars evolve onto the main sequence, the natal disk is dispersed. Any remaining circumstellar material is generally in the form of gas-poor solid debris. This dust debris must be constantly regenerated due to the short timescales of dust removal, which may be from Poynting-Robertson drag, radiation blowout, collisions, etc. (Lagrange et al., 2000). As in the case with the primordial disks, the distribution and amount of dust in debris disks are affected by several physical processes. These include, but may not be limited to, the presence of giant planets, collisional events, and radiation effects. We are interested in these systems because their evolution provides insight into the formation and evolution of our own solar system - the physical processes that occur, and the initial conditions necessary for the formation and stability of terrestrial planets in the habitable zone, and life.

High spatial resolution, mid-infrared observations of nearby stars have a great deal to contribute to the study of PMS objects and mature main sequence systems. Of particular interest is the inner region of these circumstellar environments, the regions that lie within 10 AU from the host star. Evidence of planet formation opening gaps in a primordial disk, or the presence of terrestrial planets and dusty debris point toward planetary systems similar to our own solar system (Kenyon & Bromley, 2004, 2002; Lagrange et al., 2000; Natta et al., 2000). Determining the dust distributions in this region will help constrain theoretical models, and thus provide insight into the physical processes occurring in these systems. For example, in a primordial disk, a gap in the warm dust could be indicative of a giant planet or other form of disk dispersal. In a main sequence system, the presence of warm debris implies the existence of a reservoir of solid material undergoing collisions, or even a giant planetary perturber. For these studies, high spatial

resolutions, capable of resolving the inner few AU of disks at distances of many parsecs, are absolutely essential. The mid-infrared, specifically 10 μm emission, is also a particularly interesting wavelength because it traces the thermal emission from warm dust, at temperatures of about 300K. This corresponds to the inner separations (<10 AU), or the habitable zones, of these systems. In main sequence systems, terrestrial planets lying in this region could harbor liquid water, a necessary (if not sufficient) ingredient for life as we know it.

This dissertation presents observations of circumstellar environments, using observational techniques capable of spatially resolving the inner parts of systems. In most cases, intermediate mass stars (between 2 and 4 solar masses) are observed , because their intrinsic luminosities are high enough to make their environments bright enough to observe, while their masses are low enough to produce systems which are still analogous to their lower mass counterparts, such as our own solar system. The observations are comprised of two surveys, a study of intermediate-mass PMS stars, also known as Herbig Ae stars, and secondly, observations of older main sequence stars. The former study seeks to obtain spatially resolved observations of primordial circumstellar disks, in order to ascertain the distribution, physical characteristics, and physical processes occurring in the disk. The latter survey attempts to detect debris in the habitable zones of mature stars (so called 'exozodiacal dust'). The presence or absence of such debris can indicate the presence of planets or help to constrain physical models of the system.

The remainder of this chapter will present the reader with additional background about the types of science targets observed, as well as our observational techniques, specifically, nulling interferometry. Chapter 2 will present the results from the observations of Herbig Ae stars, and Chapter 3 will describe observa-

tions and results from the main sequence observations. I will summarize the findings of this study, as well as discuss the implications of these results for future observations in Chapter 4.

1.1 Herbig Ae Stars and their Disks

Circumstellar disks have now been observed surrounding numerous PMS stars of intermediate mass. Herbig Ae (HAe) stars are of particular interest, as they are the evolutionary precursors to stars such as Vega, which are known to harbor solid material in their circumstellar environments. The earliest identification of candidate PMS stars of intermediate and high mass was made by Herbig (1960), and included 26 stars. A subsequent study of candidate stars by Strom et al. (1972) confirmed the PMS nature of several of these stars, identified the presence of circumstellar dust, and suggested a disk-like morphology for the dust. Observations of HAe stars can provide us with information regarding planet formation and the evolution of the circumstellar disks as the stars evolve onto the main-sequence. High spatial resolution studies at wavelengths near 10 μm are especially useful, as they probe material in the inner parts (few AU) of these disks, allowing one to directly observe regions where planets could form in the habitable zones of such stars.

Following the pioneering studies by Herbig (1960) and Strom et al. (1972) infrared (IR) excess emission from HAe stars was explained by the presence of geometrically thin, optically thick disks (Lada & Adams, 1992; Hillenbrand et al., 1992). This model has been subsequently modified to include central star irradiation (Calvet et al., 1991), disk flaring (Chiang & Goldreich, 1997; Kenyon & Hartmann, 1987), and other structures to explain features in the spectral energy distributions (SED), such as an inner hole, inner wall heating, and self-shadowing

(Dullemond, 2002; Dullemond et al., 2001). Alternative explanations for circumstellar emission take the form of dusty envelopes or envelope plus disk models (Miroshnichenko et al., 1999; Hartmann, Kenyon, & Calvet, 1993) as well as optically thin "haloes" in combination with disks (Vinković et al., 2006, 2003).

A review of observational results prior to 2000 can be found in Natta et al. (2000). More recently, a study by Meeus et al. (2001, hereafter M01) based on ISO spectroscopy of HAe stars suggests that they may be classified into two groups based on the shape of the SED, and that this classification may be understood by differences in disk geometry. Recent years have also seen the growth of interferometric observations of HAe stars (see Millan-Gabet et al. (2001) for a review). Leinert et al. (2004) completed a long-baseline, spectrally resolved survey of seven HAe stars using the *Very Large Telescope Interferometer* at a wavelength of 10 μm. Their study found the 10 μm emission regions to be 1-10 AU in size, and determined a correlation between the mid-IR SED slope and the physical size of the disk, where objects with larger emitting regions had redder SEDs. They have attributed this correlation to differences in disk geometry. Additional interferometric observations of HAe stars have been done in the near-IR and include the studies of Eisner et al. (2003) and Millan-Gabet et al. (2001). Eisner et al. used the Palomar Testbed Interferometer at 2.2 μm and inferred the spatial structure and orientation of the near-IR disks surrounding several stars. In a study using the Infrared Optical Telescope Array, Millan-Gabet et al. successfully resolved several near-IR emitting regions surround HAe stars, establishing a size scale for the near-IR region of 0.5 to 5.9 AU, and finding that the distribution of material surrounding resolved objects (including AB Aur) seem to favor a circularly symmetric geometry. We will compare our results to those of previous studies in §2.3.

1.2 Main Sequence Stars and Exozodiacal Dust

As the Herbig Ae stars described above evolve onto the main sequence, they shed their natal gas-rich disks. The material that remains around mature main sequence stars is often referred to as a "debris disk," which are gas poor and are composed of solid dust particles. This dust must be constantly regenerated by collisions between larger objects, as its removal timescale due to various physical processes is short (Lagrange et al., 2000). Circumstellar material around main sequence stars was first discovered in 1983 by the *Infrared Astronomical Satellite* (*IRAS*), when observations of α Lyr (Vega) showed far-infrared (far-IR) emission in excess of that expected from the stellar photosphere (Aumann et al., 1984). These detections were made at 60 and 100 μm and were followed by similar discoveries around other stars, including β Pic and α PsA (Gillett, 1986). Since then, many stars have been found to have excess far-IR emission, and this emission has been thought to be associated with thermal emission from cold circumstellar debris, similar in nature to the Kuiper disk surrounding our solar system.

These "second generation" debris disks are necessarily shaped and changed over time by internal interactions as well as interactions with planetary bodies, and can thus be a powerful tool in determining the structure and evolution of planetary systems. As mentioned above, a variety of physical processes alter the distribution of solid matter in main sequence systems. For debris disks greater than $10^{-3}M_{\oplus}$ in mass, it is believed that dust destruction is dominated by energetic collisions between grains (Dominik & Decin, 2003). Collisional cascades and subsequent radiation pressure blowout of the resulting small grains has also been hypothesized to explain observations of Vega by *Spitzer Space Telescope* (Su et al., 2005), and may be important in systems with intrinsically luminous parent stars. Icy grains may also be removed by sublimation, and systems with late

type parent stars and/or a low disk mass may be subject to Poynting-Robertson drag as a dominant removal mechanism (Dominik & Decin, 2003). Regardless of the removal mechanism, timescales for dust survival are generally short compared to the lifetime of the star, and therefore necessitates regeneration of dust via collisions of larger bodies, such as comets or asteroids (Lagrange et al., 2000).

Though several cases of cold dust at far-IR wavelengths have been confirmed, to date there have been no spatially resolved detections of mid-infrared (mid-IR) emission (at 10 μm) surrounding main-sequence stars older than a few tens of millions of years. Whether this is a result of a need for greater sensitivity and/or spatial resolution in the observations, or due to a physical reason in the observed systems is not known. We address this question by using nulling interferometry to achieve improved spatial resolution and the contrast necessary to begin probing whether warm debris is present in nearby main sequence systems. A positive detection would be indicative of warm ("room-temperature"; 300 K) dust close to the star, analogous to the zodiacal dust in our own solar system. Any material emitting at 10 μm would be in the "habitable zone" of a system where liquid water could exist. The presence of dust would also necessitate the presence of planetesimals which would, through collisions, regenerate the dust that is normally depleted on fast timescales. Resolved mid-IR disks have been detected around the main-sequence A-type stars β Pic (Pantin et al., 1997; Weinberger et al., 2003) and HR 4796A (Jayawardhana et al., 1998; Jura et al., 1998), though HR 4796A is thought to be very young, with an age less than 10 Myr and β Pic is estimated to be less than 30 Myr old (Barrado y Navascués et al., 1999). Detection of a mid-IR disk around an older star like those in our sample (a few hundred Myr) proves to be more difficult, since densities of the solid material are substantially lower than those in primordial disks, thus optically thin.

The power of using circumstellar debris disks to investigate the nature of a planetary system is evident from our own solar system's debris. The Kuiper Belt, provides readily observable constraints on models of planetary formation (Moro-Martín & Malhotra, 2003; Jewitt & Luu, 2000; Malhotra et al., 2000) as well as constraints for n-body simulations that model the rich dynamical history of our solar system (Gomes et al., 2005). In the same way, observations of debris around nearby stars can be used to infer the history and physical structure of exosolar systems, with the additional benefit that this material is more easily detected directly than exosolar planets themselves (e.g., the warm debris in our solar system is 100 more luminous at 10 μm than Jupiter, due to a larger total emitting surface). The overall purpose of the observations presented in this dissertation is the characterization of dust and planets in systems outside our own, thus gaining insight into the physical processes determining the creation and distribution of dusty debris.

1.3 Nulling Interferometry

1.3.1 Nulling Basics

Nulling interferometry is a technique used to study spatially resolved circumstellar material in the presence of unresolved flux, and represents an ideal opportunity to observe the circumstellar environments of intermediate-mass stars. The technique, first proposed by Bracewell (1978) is implemented by overlapping the pupils of two telescopes (or two subapertures on a single aperture telescope) with an optical path length difference of one-half λ between the beams. The result of such a configuration is a sinusoidal transmission function with the functional form

$$T(\theta) = sin^2(\pi b\theta/\lambda) \tag{1.1}$$

where b is the baseline of the interferometer, λ is the wavelength of observations and θ is the angular distance from the observed object to the pointing center of the interferometer (Hinz et al., 1998). During observations, the central destructive fringe is placed on the unresolved point source. This allows us to detect spatially resolved emission, effectively isolating it from the unresolved stellar flux. In observing HAe stars at wavelengths near 10 μm, where the circumstellar emission dominates the stellar flux (often by more than 2 orders of magnitude), isolating the resolved disk emission from the unresolved disk emission gives us valuable information about the spatial distribution of circumstellar dust. Additionally, nulling interferometry provides the necessary contrast to observe faint circumstellar material in the presence of a much brighter star, currently achieving contrast ratios of about 100. This is essential when observing debris disks surrounding main sequence stars, where stellar flux outshines the debris, usually by at least a factor of several hundred. This technique can detect material as close to the star as one-quarter of the fringe spacing where the light is neither suppressed nor enhanced. This corresponds to 0.12 arcseconds for the configuration used on the MMT, or 12 AU about a star at 100 pc. This is between 2 and 3 times finer spatial resolution than the diffraction limit at the wavelengths observed in these observations (8 to 13 μm).

1.3.2 The BLINC-MIRAC Instrument

The BracewelL Infrared Nulling Cryostat (BLINC) is the instrument containing the optics which allows a single aperture telescope to be used as a nulling interferometer. Figure 1.1 (Hinz , 2001) shows the optical layout of BLINC. The telescope beam is first re-imaged into the appropriate focal ratio required by the science camera (described below) and divided into two separate beams with two flat mirrors. In one arm of the interferometer, a piezo-translator allows the path

length of the arm to be adjusted, in order to achieve the phase difference in the beams necessary to produce destructive interference. The two beams, now out of phase, are reflected onto opposite sides of a 50% beam splitter which combines the beams. The interfered image is sent to the Mid-Infrared Array Camera 3 (MIRAC3; Hoffmann et al. (1998)) for imaging. The optics of BLINC are liquid nitrogen cooled to reduce the thermal emissivity of the optical components of the interfereometer.

MIRAC3 uses a liquid helium cooled 128 x 128 arsenic-doped silicon array to image at mid-IR wavelengths. The camera allows for very rapid exposures (tens of milliseconds), which is necessary for the non-adaptive optics implementation of nulling interferometry (see §2.1.2). In science observations with MIRAC3 at the MMT, we were able to achieve a signal-to-noise of 20 with a one second integration on a 10 Jy source in the N-band.

1.3.3 Nulling Interferometry with Adaptive Optics

In more recent observations at the MMT, nulling interferometry was implemented in combination with the MMT's natural guide star adaptive optics system (MMTAO). MMTAO is capable of producing diffraction limited images in the N-band. The deformable mirror, also the telescope's secondary mirror (Figure 1.2), consists of a shell 2 mm thick and 0.64 m in diameter, which is deformed with 336 actuators attached to the rear of the shell.

MMTAO also has several specific benefits when used with nulling interferometry. First, wavefront aberrations introduced by the atmosphere that might affect the suppression level of the null are significantly reduced or eliminated. The stabilization of the incoming wavefront therefore allows us to precisely tune the path length between the arms of the interferometerby adujusting the voltage on the piezo-translator, allowing for the best possible suppression of light. Hence

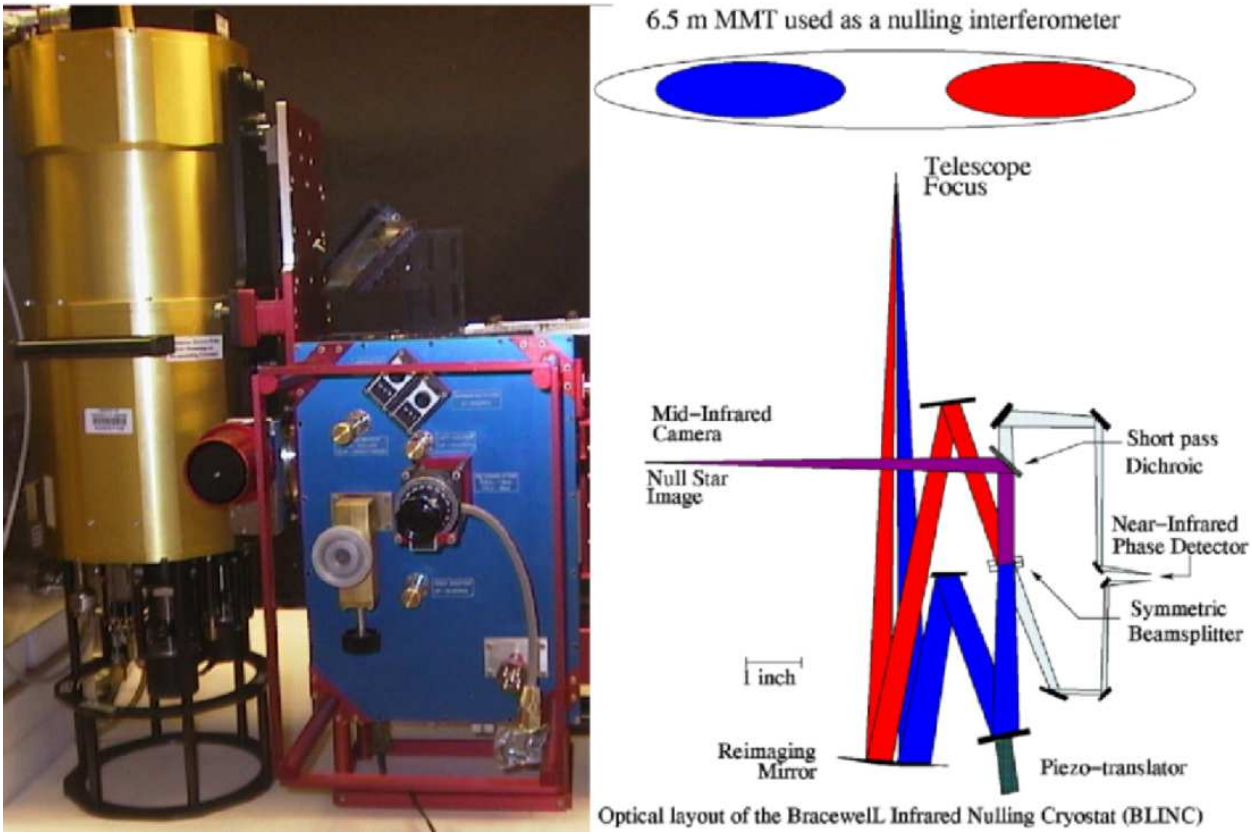

Figure 1.1 *Left:* The BLINC-MIRAC instrument. The blue housing is the BLINC instrument, and the gold cylinder is the MIRAC3 camera. The height of MIRAC3 is approximately 1 meter. *Right:* The optical layout of BLINC. Both images reproduced from Hinz (2001)

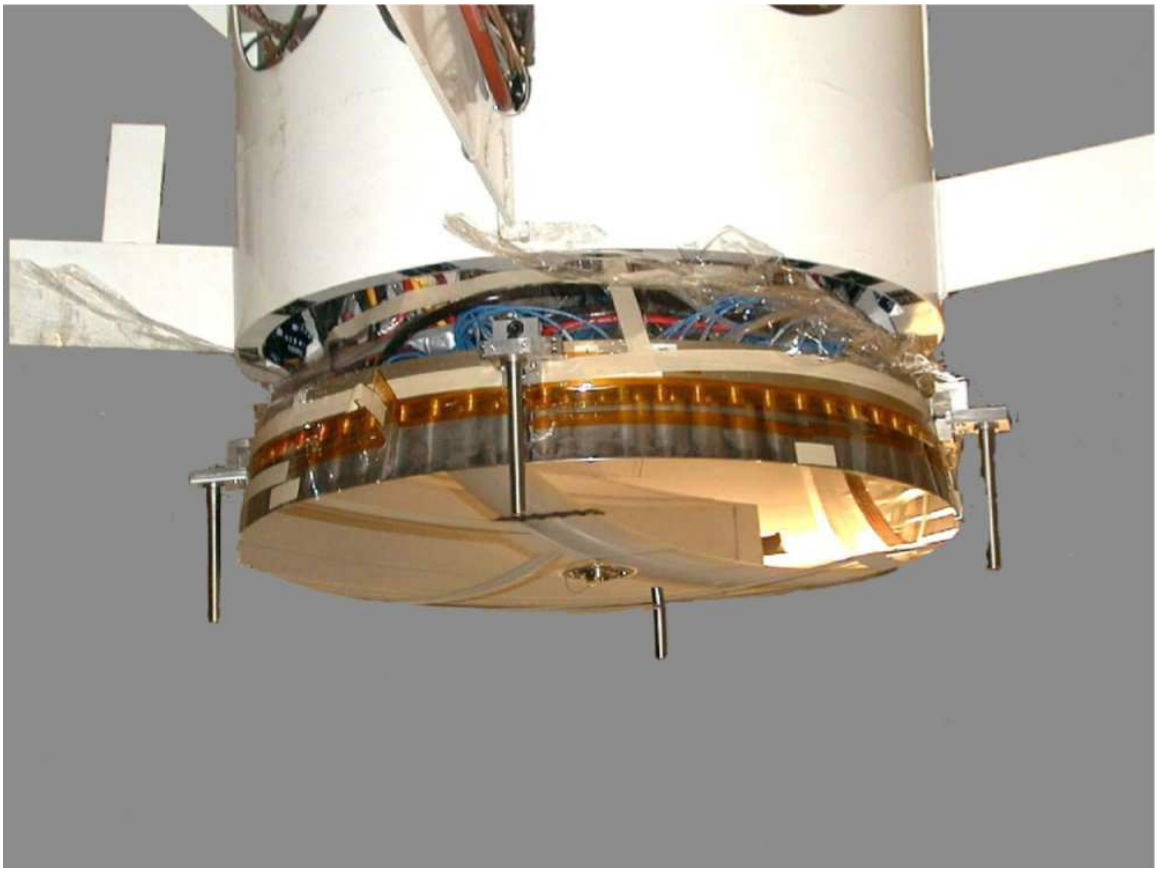

Figure 1.2 The MMT's adaptive optics secondary mirror. (Photo courtesy Center for Astronomical Adaptive Optics)

observations are made more efficient (see §2.1). Additionally, a stable wavefront and image allows us to integrate for greater periods of time, making fainter resolved flux detectable. The addition of wavefront correction also lessens the amplitude of phase variations from frame to frame, resulting in smaller errors in calibration. The unique nature of the deformable secondary also has benefits in mid-infrared observations. Since the secondary mirror of the telescope is the deformable mirror, there is no need for an intermediate set of correcting optics between the telescope and science camera. This reduces the number of warm surfaces in the optical path, minimizing background and maximizing throughput. Conventional AO systems typically have a background emissivity of about 20 %, compared to a deformable secondary system which can have emissivities in the range of 5 to 7 %. This can translate to a 3 to 4$\times$ speed improvement in mid-IR observations. More technical details regarding the MMT adaptive secondary can be found in Brusa et al. (2003).

CHAPTER 2

OBSERVATIONS OF HERBIG AE STARS AND DISKS

This chapter presents results from observations of intermediate mass pre-main sequence stars, also called Herbig Ae (HAe) stars. The overall goal of these observations is to spatially resolve the primordial circumstellar disks of the target stars and to infer their physical characteristics (e.g. size, orientation, distribution, radial temperature profiles, etc.). The physical nature of resolved disks is determined by using a combination of models, from simple Gaussian density and uniform ring distributions, to flared disk models based upon Chiang & Goldreich (1997), to interpret the significance of our observational data. Doing so allows us to gain insight into the physical processes which affect the evolution of primordial circumstellar dust and to find signs of any trends in disk characteristics. We will also discuss our results in the context of previous observations at other wavelengths to form a more complete picture of these disks at different spatial scales, as well as compare and contrast individual objects in our sample.

2.1 Observations and Data Reduction

2.1.1 Target Selection

Targets for this survey were taken from a catalog of Herbig Ae/Be stars by The et al. (1994). The objects were chosen to include stars with a spectral type of B8 or later, as HAe stars have been found to have a significantly higher incidence of circumstellar disks than Herbig Be stars (Natta et al., 2000). All objects (except one, HD 98922) were chosen to be within 250 pc, to ensure our ability to spatially resolve a circumstellar disk, should one be present. All targets also have a 12 μm flux (IRAS) greater than 10 Jy, to ensure sensitivity to any resolved emission.

A large flux is necessary for non-AO observations, as we are limited to short integration times (see §2.1.4). The final sample of 13 stars, along with their stellar characteristics, is shown in Table 2.1.

Observations of 13 HAe stars were made in 2001 August and 2002 May at the 6.5 m Magellan I (Baade) telescope at the Las Campanas Observatory, Chile and 2002 November, 2004 January, and 2005 June at the 6.5 m MMT at Mt. Hopkins, Arizona. On these single-aperture telescopes, nulling interferometry is implemented by dividing the aperture into two identical elliptical subapertures, each 2.5 x 5 m (at the MMT; Magellan observations completed without AO used two 2.5 m diameter circular apertures) with a baseline of 4 m. Observations were taken at 10.3, 11.7, and in a few cases 12.5 μm, each with a bandwidth of 10%, and a wide 10.6 μm (N-band) filter with a 50% bandpass. Additionally, observations of HD 100546 taken at Magellan I included direct imaging taken with BLINC-MIRAC at longer wavelengths (18.0 and 24.5 μm).

2.1.2 Non-AO Observations

Observations taken at Magellan and during the 2002 MMT run were done without AO. Without wavefront correction, atmospheric aberrations randomize the path difference between the two arms of the interferometer. Thus data must be taken with frame times (50 ms) shorter than the timescale of atmospheric variation, in order to freeze out the seeing effects. In this case, images are taken contiguously in large sets, typically 500 to a set. This number of frames was empirically determined to be sufficient to sample the phase between the beams, and thus include several frames with a phase difference close enough to one-half wave that higher order spatial errors dominate the level of residual flux in the focal plane. The images with the best null (destructive interference) and constructive interference in each set are selected in order to evaluate the "instrumental

Table 2.1. Herbig Ae Target List

Name	Spec. Type	d(pc)	log Age(Myr)	Group*	Refs.
HR 5999	A5-7	210 ± 40	5.7 ± 0.3		1,3,4,6
KK Oph	A6	160 ± 30	6.5 ± 0.5	II	2
DK Cha	A	~ 200			1,3
HD 150193	A1	150 ± 30	> 6.3	II	1,4,6
HD 98922	B9	> 540			1,4
HD 104237	A4	116 ± 8	6.3 ± 0.1	II	1,4,6
51 Oph	A0	131 ± 15	5.5 ± 0.2	II	1,2,6
R CrA	B8	~ 130			3
AB Aur	A0	144 ± 20	6.4 ± 0.2	I	3,4,5,6
V892 Tau	A6	150 ± 10	> 7		3,5
HD 100546	B9	103 ± 7	$> 7^{\dagger}$	I	1,2,4,6
HD 163296	A3	122 ± 15	6.6 ± 0.4	II	2,6
HD 179218	B9	244 ± 55	5.0 ± 0.6	I	2,6

Note. — References- 1) SIMBAD; 2) Leinert et al. (2004); 3) Hamaguchi et al. (2005); 4) van den Ancker et al. (1998); 5) Natta et al. (2000, and ref. therein), 6) Perryman et al. (1997).

*Meeus et al. (2001) SED Group

†HD 100546 attributed to Lower Centaurus-Crux OB association by de Zeeuw et al. (1999) with an association age of 16 Myr (Mamajek et al., 2002).

null" (see below). Ten off-source sky frames, used to subtract out the sky background, are taken after each set of frames on-source. For each science object we take several sets of frames (usually between 4 and 10), so that we are able to estimate the variation in the best null from set to set and hence derive an error in the null. From the lowest and highest fluxes in each set of frames, we calculate the *instrumental null* which is defined as:

$$N = Flux_{nulled}/Flux_{constructive} \tag{2.1}$$

and expressed as a percent.

Observations of each science object are followed by 2 to 4 sets of 500 frames of a point source (spatially unresolved) calibrator star in order to establish a baseline for goodness of null achieved in the most recent science observations. Calibrator nulls generally ranged between 5% and 15%. We use the null achieved on the calibrator to calculate the *source null* defined as the difference between the instrumental null on the science object and the calibrator:

$$S = N_{science} - N_{calibrator} \tag{2.2}$$

This represents the resolved flux as a percentage of the full flux of the target. A source null of zero means that the science object is spatially unresolved.

Additionally, observations are taken with different rotations of the interferometer baseline relative to the sky. Typically, two sets of 500 frames are taken at each rotation. This allows us to probe for the presence of an elongated or flattened structure (such as an inclined disk) if resolved emission is detected, which is accomplished in the following manner. The output of the interferometer is a transmission pattern superimposed on the stellar image. This transmission pattern has a sinusoidal functional form shown in §1, with the destructive interference fringe directly on axis, and aligned perpendicular to the baseline of the interferometer.

If a flattened extended structure is present surrounding our science target, and the major axis of the emission is aligned parallel to the destructive interference fringe, we would expect a deeper null (smaller N) than when the fringe and the major axis are orthogonal. The resulting dependence of N vs. the rotation of the interferometer would be sinusoidal with a period of 180°,

$$S = a + bsin(PA + \theta) \tag{2.3}$$

The parameters a, b, PA, and θ are determined by the size of the emitting region, its inclination, the position angle of its major axis, and rotation of the interferometer baseline, respectively.

2.1.3 Observations with AO

Observations taken in 2004 January and 2005 June at the MMT were done with the AO secondary. As described in the Introduction, the use of AO significantly increases the efficiency of observations. Since, with AO, we are able to precisely tune the path difference between the arms of the interferometer, large sets of fast frames to freeze-out atmospheric effects are unnecessary. AO also stabilizes the image, generally resulting in smaller errors in the null. In this case, we take sets of 10 frames (usually ~ 1 s integration) of the object tuned to destructive interference, followed by 10 frames of the object in constructive interference. Observations of the calibrator are taken in the same manner, with off-source sky frames taken after each destructive-constructive pair. An example of a series of calibrator measurements is shown in Figure 2.1, and plots the calibrator null vs. time during observations utilizing AO. Calibrator nulls typically ranged between 3% and 6% with AO, indicating an improvement in both null depth and stability compared to non-AO observations, which often varied by 5 to 10% over several hours.

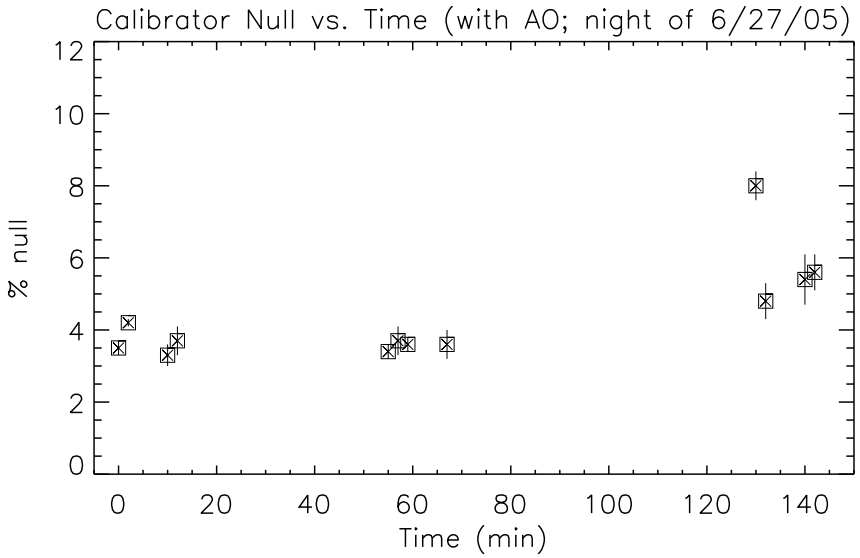

Figure 2.1 A typical series of calibrator null measurements taken over the course of about 2.5 hours. The calibrator in this case was γ Dra, and the observations were taken with AO on the night of 26 June 2007 during science observations of HD 179218. Each data point and error bar represents an average of three sets of images. The decrease in null depth toward the end of the series is a result of degrading observing conditions (i.e., poor seeing).

Table 2.2 summarizes all observations of science targets, taken with and without AO.

Table 2.2. Herbig Ae Summary of Observations

Set	Star	λ (μm)	# Frames	Intgr./frame (s)	PA (or rotation*)(°)	Tel.	Ref.
1-2	HR 5999	11.7	1000	0.5	-165(rot.)	Mag.	1
3-4	″	″	″	″	110(rot.)	″	1
5-6	KK Oph	11.7	1000	0.5	-150(rot.)	Mag.	1
7-8	″	″	″	″	120(rot.)	″	1
9-10	DK Cha	11.7	1000	0.45	-170(rot.)	Mag.	1
11	HD 150193	11.7	1000	0.45	145(rot.)	Mag.	1
12	″	10.3	500	0.5	97	MMT	2
13-14	HD 98922	11.7	1000	0.55	-40(rot.)	Mag.	1
15-16	″	10.3	″	0.55	″	″	1
17-18	HD 104237	11.7	1000	0.55	-60(rot.)	″	1
19-20	″	10.3	″	″	″	″	1
20-21	51 Oph	11.7	1000	0.11	135(rot.)	″	1
22	″	″	500	″	45(rot.)	″	1
23	R CrA	11.7	1000	0.11	0(rot.)	″	1
24	″	″	″	″	30(rot.)	″	1
25-27	AB Aur	10.3	60	1.0	170	MMTAO	3
28-30	″	″	″	″	107	″	3
31-33	″	″	″	″	71	″	3
34-36	″	″	″	″	131	″	3
37-39	″	″	″	″	4	″	3
40-41	V892 Tau	11.7	1000	0.5	164	MMT	3
42-43	″	″	″	″	116	″	3
44-46	″	10.3	60	1.0	160	MMTAO	3
47-48	HD 100546	10.3	1000	0.5	-80(rot.)	MMT	4
49-50	″	″	″	″	-50(rot.)	″	4
51-52	″	″	″	″	-24(rot.)	″	4
53-54	″	″	″	″	10(rot.)	″	4
55-56	″	″	″	″	40(rot.)	″	4
57-58	″	11.7	1000	0.5	-80(rot.)	MMT	4
59-60	″	″	″	″	-50(rot.)	″	4
61-62	″	″	″	″	-24(rot.)	″	4
63-64	″	″	″	″	10(rot.)	″	4

Table 2.2—Continued

Set	Star	λ (μm)	# Frames	Intgr./frame (s)	PA (or rotation*)(°)	Tel.	Ref.
65-66	″	″	″	″	40(rot.)	″	4
67-68	″	12.5	1000	0.5	-80(rot.)	MMT	4
69-70	″	″	″	″	-50(rot.)	″	4
71-72	″	″	″	″	-24(rot.)	″	4
73-74	″	″	″	″	10(rot.)	″	4
75-76	″	″	″	″	40(rot.)	″	4
77	HD 163296	10.3	500	0.5	94	MMT	2
78	″	″	″	″	10	″	2
79	HD 179218	10.3	500	0.5	162	MMT	2
80	″	″	″	″	87	″	2
81-89	″	10.6	90	1.0	50	MMTAO	1
90-98	″	″	″	1.0	60	MMTAO	1
99-104	HD 179218	10.6	60	1.0	99	MMTAO	1
105-110	″	″	″	1.0	103	MMTAO	1

Note. — References- 1) this paper; 2) Hinz et al. (2001); 3) Liu et al. (2005); 4) Liu et al. (2003)

*The PA probed by the nulling observation depends on both the rotation of the interferometer baseline and the paralactic angle of the object when observed. For objects denoted 'rot.' the paralactic angle was not recorded, so the rotation of the interferometer (degrees from an arbitrary position) is noted so the reader can estimate the relative value of the PA for observations of each object.

2.1.4 Nulling Data Reduction

For non-AO observations, each on-source frame is sky subtracted using a sky frame created by median combining the 10 off-source frames taken immediately after the science frames. A custom IDL program is used to extract aperture photometry from each sky subtracted frame. The aperture size for each set of frames is chosen by determining the radius at which the source flux disappears into the noise. The noise level is assessed in an annular region several pixels wide, well outside the aperture. For each set of 500 frames, we identify the frame with the smallest residual flux (best null) and the brightest constructive image. These two

frames are used to evaluate the instrumental null. The null for each set of calibrator images is evaluated in an identical way.

For the frames taken with AO, the best destructive frame in each set is determined using aperture photometry in a manner identical to the non-AO procedure described above. The instrumental null is determined by using the best nulled image and a median combined composite image of the constructive frames. Instrumental nulls for calibrator stars, taken in between science objects, were evaluated in an identical manner.

Source nulls were evaluated for all data by subtracting the instrumental null of the calibrator from the instrumental null achieved on the science object. A table of instrumental, calibrator, source nulls, and errors is shown in Table 2.3. The values of the nulls represent an average of the data sets taken at each wavelength and position angle, and errors are the 1 σ dispersion in the values. A summary of the data reduction pipeline can be found in Appendix A.

2.2 Results

Out of 13 objects observed, we have conclusively resolved three of the objects, HD 100546 (at 3 different wavelengths and 5 different rotations) and AB Aur (at one wavelength and 5 different rotations) and HD 179218 (at one wavelength and 2 rotations). Additionally, we have marginally resolved (at about the 2.5 σ level) two stars, V892 Tau and R CrA. Source nulls for all objects can be found in Table 2.3.

Table 2.3. Herbig Ae Instrumental and Source Nulls

Star	Instr. Null (%)	Cal. Null (%)	Source Null (%)	PA (or rotation)(°)	λ (μm)	Ref.
HR 5999	5.7 ± 4.6	5.6 ± 2.5	0.1 ± 5.2	-165(rot.)	11.7	1
″	1.1 ± 1.1	″	-4.5 ± 2.7	110(rot.)	″	1
KK Oph	7.5 ± 4.2	5.6 ± 2.5	1.9 ± 4.9	-150(rot.)	11.7	1
″	4.3 ± 2.9	″	-1.3 ± 3.8	120(rot.)	″	1
DK Cha	10.3 ± 4.2	8.4 ± 1.5	1.9 ± 4.4	-170(rot)	11.7	1
HD 150193	10.6 ± 2.6	6.9 ± 0.2	3.7 ± 2.6	145(rot.)	11.7	1
″	13 ± 5	13 ± 2	0 ± 5	97	10.3	2
HD 98922	5.9 ± 3.3	24.1 ± 7.6	-18.2 ± 8.3	-40(rot.)	11.7	1
″	15.2 ± 5.8	12.3 ± 3.9	2.9 ± 7.0	″	10.3	1
HD 104237	9.2 ± 6.7	15.5 ± 1.0	-6.3 ± 6.7	-60(rot.)	11.7	1
″	10.3 ± 1.9	15.4 ± 3.2	-5.1 ± 3.7	″	10.3	1
51 Oph	11.9 ± 1.1	22.9 ± 10.4	-11.0 ± 10.5	1	11.7	1
″	7.3 ± 5.0	″	-15.6 ± 11.5	2	″	1
R CrA	19.8 ± 5.1	18.1 ± 2.7	1.7 ± 5.8	1	11.7	1
″	26.4 ± 1.9	″	8.3 ± 3.3	2	11.7	1
AB Aur	25.9 ± 1.5	5.1 ± 0.2	20.8 ± 1.5	170	10.3	3
″	18.3 ± 1.4	″	13.2 ± 1.4	107	″	3
″	24.1 ± 2.9	″	19.0 ± 2.9	71	″	3
″	20.9 ± 1.5	″	15.8 ± 1.5	131	″	3
″	31.7 ± 3.1	″	26.6 ± 3.1	4	″	3
V892 Tau	24.2 ± 2.2	18.5 ± 0.8	5.7 ± 2.3	164	10.3	3
″	37.9 ± 7.2	22.0 ± 1.3	15.9 ± 7.3	116	11.7	3
″	36.4 ± 0.2	″	14.4 ± 1.3	160	11.7	3
HD 100546	45.5 ± 1.6	8.6 ± 0.1	36.9 ± 1.6	-80(rot)	10.3	4
″	39.9 ± 7.0	″	31.3 ± 7.0	-50(rot)	″	4
″	41.9 ± 2.8	″	33.3 ± 2.8	-24(rot)	″	4
″	29.8 ± 8.9	″	21.2 ± 8.9	10(rot)	″	4
″	31.6 ± 0.6	12.5 ± 1.8	19.1 ± 1.9	40(rot)	″	4
″	40.0 ± 2.3	6.4 ± 2.4	33.6 ± 3.3	-80(rot)	11.7	4
″	26.1 ± 2.7	″	19.7 ± 3.6	-50(rot)	″	4
″	37.4 ± 2.5	8.6 ± 2.0	28.8 ± 3.2	-24(rot)	″	4
″	31.8 ± 2.6	″	23.2 ± 3.3	10(rot)	″	4

Table 2.3—Continued

Star	Instr. Null (%)	Cal. Null (%)	Source Null (%)	PA (or rotation)(°)	λ (μm)	Ref.
″	24.3 ± 2.0	9.8 ± 2.2	14.5 ± 3.0	40(rot)	″	4
″	35.5 ± 2.8	5.6 ± 1.8	29.9 ± 3.3	-80(rot)	12.5	4
″	48.8 ± 1.3	″	43.2 ± 2.2	-50(rot)	″	4
″	30.9 ± 1.7	6.1 ± 0.1	24.8 ± 1.7	-24(rot)	″	4
″	26.4 ± 1.6	″	20.3 ± 1.6	10(rot)	″	4
″	16.3 ± 5.9	10.3 ± 2.1	6.0 ± 6.3	40(rot)	″	4
HD 163296	12 ± 7	13 ± 2	-1 ± 7	94	10.3	2
″	16 ± 2	″	3 ± 3	10	″	2
HD 179218	16 ± 2	13 ± 2	3 ± 3	162	10.3	2
″	14 ± 2	″	1 ± 3	87	″	2
″	10.5 ± 2.4	3.7 ± 0.6	6.8 ± 2.5	50	10.6	1
″	8.5 ± 1.8	3.6 ± 0.8	4.9 ± 2.0	60	″	1
HD 179218	7.2 ± 1.2	3.6 ± 0.8	3.6 ± 1.4	99	10.6	1
″	11.4 ± 2.5	5.9 ± 1.2	5.5 ± 2.8	103	″	1

Note. — References- 1) this paper; 2) Hinz et al. (2001); 3) Liu et al. (2005); 4) Liu et al. (2003)

2.2.1 A Note about Errors and Negative Nulls

In determining the errors for each set of data, we consider two sources of error, variation in the instrumental null as a result of minor phase variations between the two beams, and photometric error. The former is caused by small variations in the phase between each frame and set of frames, which changes the best null derived for each set. This effect, likely the result of small vibrations in the telescope, is exacerbated by poor seeing conditions which increase the amplitude of phase differences between each set of frames. Our errors in Table 2.3 account for this effect. The average error in source nulls for all wavelengths and rotations in the HD 100546 observations was $\pm 3.2\%$ with the largest variation in null between sets taken at the same wavelength and orientation being $\pm 8.9\%$. AO observations

decreased the variation in the null, and hence the overall error. The average value for the error in source null for AB Aur observations taken with AO is $\pm 2.1\%$ with a maximum variation of $\pm 3.1\%$. Photometric errors in bright objects such as those in our sample were generally small and contributed at most, at an equal level to variations in the null. This was not the case with the main sequence sample, where photometric errors often dominated over phase variation (see §3.1).

One may note that source nulls are negative at a significant level ($> 2\sigma$) for one set of data. Negative source nulls are unphysical, hence the appearance here necessitates an explanation. The negative value for the set in question (HD 98922, 11.7 μm) can be attributed to an inaccurate measurement of the calibrator null taken immediately after the science object. Analysis of the calibrator images shows a slightly "dual-peaked" image of the star, indicating a slight misalignment in the beams of the interferometer and/or a temporary degradation in observing conditions (i.e., bad seeing). This results in a poor null (abnormally large value) for the calibrator null, hence a negative value for a source null. It is important to note that a poor null in the calibrator cannot result in a false positive detection of resolved material, and any detections of resolved emission are checked to ensure that they are not a result of poor seeing or misalignment. This is done by visually inspecting each image for signs of misalignment or degredation in seeing, which would manifest itself as the aforementioned "dual-peaked" images or a slight elongation in the image. One would expect a misalignment of one or two pixels to have an effect on the null (decreased suppression) of well under one percent; thus, any misalignment large enough to have a significant effect on the null would be noticed by inspection of the frames. The negative source nulls are included here for the sake of completeness in presenting data. Other negative source nulls are present in the results, but their significance is marginal, as the

values are negative at less than a 2 σ significance. The large values of calibrator nulls and errors in these cases are likely due to short-lived poor seeing affecting a single observation of the calibrator (two or more observations of the same calibrator are averaged to produce the quoted value for the calibrator null). Again, the inclusion of these results is for the sake of completeness and transparency in our methodology.

2.2.2 Simple Disk Models - Assessing Size and Flaring

In order to infer the size of the emitting region for each resolved object, we use two simple disk models: 1) the intensity of the disk is a Gaussian function with the peak at the center; and 2) the source of the emission is confined to an annulus of uniform intensity around the star. The models are placed at the distance of the object and convolved with the transmission pattern of the interferometer, and a theoretical source null is calculated. The size of the emitting region in the model is adjusted until the results best match the observationally determined source null. Models are fit for each wavelength at which an object was observed. For any object which we have data at several rotations of the interferometer baseline, we fit a sinusoidal function of the form described in §2.1.2 to the S vs. PA relation determined from our nulling observations.

The extent of the 10 μm emitting region in each of the resolved objects is a powerful tool for determining the physical structure of warm dust in the system. Several factors contribute to the spatial extent of emission. One factor is the degree of disk flaring, thus we explore the effect of flaring on the nulling observations. Another factor affecting the extent of the emitting region is grain size, as larger blackbody grains would tend to result in an emitting region closer to the star, due to the relative efficiency in emission compared to small grains. We also examine the effect of grain size on our observations.

In order to assess the effect that the degree of disk flaring has on the resolvability of a target, we construct a simple face-on flared disk model based on the model of Chiang & Goldreich (1997, hereafter CG97). In our model we vary the degree of flaring by adjusting the power-law dependence of the flaring term, H/a (Eq. 10, CG97, where H is the height of the disk above the midplane and a is the radial separation between the star and a point on the midplane of the disk). The exponent of a is varied from 0 (the flat disk case, i.e. constant H/a) to 2/7 (the vertical hydrostatic equilibrium case, i.e. $H/a \sim a^{2/7}$). Other parameters assumed in the CG97 model include a dust mass of 1% of the gas mass, uniformly mixed, a grain size of 0.1 μm, and a mass density of 2 g cm^{-3}. The CG97 model was used to determine the brightness from a hypothetical disk, using canonical stellar parameters (effective temperature, mass, radius and luminosity) (Cox, 2000) appropriate for the spectral types of the targets' parent stars, while varying the amount of flaring in the disk. This brightness signature is then convolved with the transmission function of the interferometer to predict the source nulls expected for varying degrees of flaring. Figure 2.2 shows the predicted values of the source null as a function of the degree of flaring (represented by the value of the exponent of a) for a range of spectral types. We see that the model predicts very large source nulls (40-75%) for the maximally flared disks in all cases. This holds true also for the outer part of the model (Dullemond et al., 2001, Eq.5) which predicts flaring as the disk emerges from the shadowed region. The largest source null for our resolved objects approaches 40% for HD 100546, a B9 star. Thus, it appears that if one considers flaring as the only factor affecting the observed source null, none of the objects display flaring to the degree of the hydrostatic equilibrium case. It is a possibility that this is an indication that the warm dust may be in a flatter distribution than expected (possibly due to dust settling toward the disk

midplane). However, one must keep in mind that other factors (such as the orientation of the dust relative to the rotation of the interferometer baseline) can have a significant effect on the source null.

Spatial information about the emission regions surrounding these stars is also important in breaking degeneracies in interpreting the SEDs with regard to grain size. For example, large grains, with sizes similar to the wavelength of emission, at closer separations the star can mimic the emission from small, ISM-sized grains in a more extended distribution. In the model based on CG97 described above, the assumed grain size is 0.1 μm, or ISM-sized grains. Thus, for resolved objects, if grain sizes are actually larger than the assumed size, this would require a greater degree of flaring than the actual values calculated with the model, in order to account for the same level of resolved flux. When comparing the relative effect that grain size and flaring have on the temperature profile of the dust, we see that varying the flaring has a greater effect on the power law dependence of the effective temperature vs. separation from the star. Increasing the flaring from a flat distribution to a flared distribution (at vertical hydrostatic equilibrium) results in a change from a $T \sim r^{-0.75}$ relation to $T \sim r^{-0.4}$, and to a change in source null of 40-70%, depending on the luminosity of the star.

Table 2.4 summarizes the sizes and flaring parameters that best fit the nulling data, with the errors representing the error in source null shown in Table 2.3. For unresolved objects, a maximum size for the emitting region is shown, calculated using the error in the source null. Further information regarding the fitting procedures used in this section can be found in Appendix B.

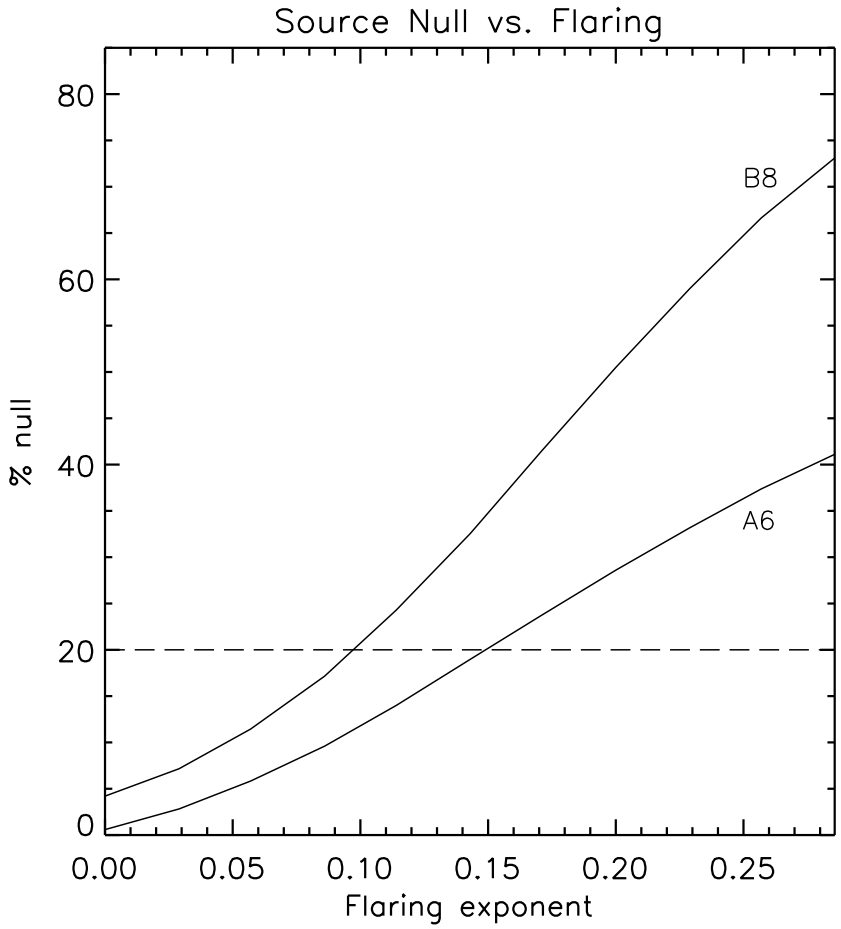

Figure 2.2 Predicted source null vs. degree of flaring for a Herbig Ae star at 140 pc. The degree of flaring is represented by varying the exponent of a in Chiang & Goldreich (1997, Eq.10) from 0 (the flat disk case) to 2/7 (the vertical hydrostatic equilibrium case). Spectral types A6 and B8 are shown; intermediate types lie between the two curves. The horizontal dashed line represents the median (and mean) source null (20%) for all spatially resolved measurements.

Table 2.4. Herbig Ae Disks: Best Fit Models

Name	λ (μm)	Gaussian FWHM (AU)	Ring diameter (AU)	Flaring Exp.*	Ref.
HR 5999	11.7	< 19	< 26	< 0.06	1
KK Oph	11.7	< 14	< 19	< 0.06	1
DK Cha	11.7	< 17	< 23	< 0.05	1
HD 150193	11.7	< 12	< 16	< 0.01	2
HD 98922	11.7	< 48	< 68	< 0.04	1
HD 104237	11.7	< 12	< 16	< 0.07	1
51 Oph	11.7	< 17	< 23	< 0.08	1
R CrA	11.7	15 ± 4	20 ± 4	0.02-0.07	1
AB Aur	10.3	27 ± 3	30 ± 3	0.1-0.15	3
V892 Tau	10.3	14 ± 2	20 ± 3	0.05-0.15	3
″	11.7	23 ± 5	31 ± 6	0.05-0.15	3
HD 100546	10.3	24 ± 3	26 ± 3	0.08-0.18	4
″	11.7	25 ± 3	27 ± 3	0.07-0.18	4

2.3 Discussion - Trends in the Full Sample

In selecting our HAe targets, we included objects with a range of spectral types and ages, in the hope that any evidence of evolution in the PMS environment, or differences in the circumstellar region due to the stellar mass of the parent star could be probed. However, we have found that the resolved objects in our sample appear to have a range of stellar characteristics. The resolved objects have spectral types ranging from late B-type (HD 100546 and HD 179218) to A6 (V892 Tau), and ages ranging from approximately 0.1 (HD 179218) to > 10 Myr (HD 100546). Therefore, there seems to be no distinguishing characteristic between unresolved and resolved sources in terms of age or spectral type. A plot of the inferred disk size (see §2.2.2) vs. the stellar age (for those objects with age determinations in the literature) is shown in Figure 2.3a and shows no obvious trend. This could be due to either: 1) errors in age estimates for these stars or 2) the fact that time is not the sole or dominant factor affecting disk evolution.

An analysis of the spectral energy distributions (SED) of the observed stars, however, does suggest a trend in the resolved objects. Meeus et al. (2001, hereafter M01) categorizes HAe stars into two major groups: Group I with large amounts of mid-infrared excess, and Group II with moderate quantities of mid-IR excess, descending at longer wavelengths. For those objects with classifications in the literature, we find that two out of three Group I objects were resolved in our initial observations (we do not include HD 179218 as a resolved object here since it was unresolved in our initial, non-AO observations), while zero of five Group II objects showed resolved emission. This trend is evident in a plot of disk size vs. the submillimeter SED slope (Fig. 2.3b), which M01 finds correlates well with the mid-IR SED grouping of the star and could be considered a surrogate for the evolutionary state of the disk. Objects with steeper sub-mm slopes (in-

Table 2.4—Continued

Name	λ (μm)	Gaussian FWHM (AU)	Ring diameter (AU)	Flaring Exp.*	Ref.
″	12.5	30 ± 3	33 ± 3	0.02-0.2	4
HD 163296	11.7	< 11	< 15	< 0.08	2
HD 179218	10.6	20 ± 4	27 ± 5	0.01-0.05	1

Note. — References- 1) this paper; 2) Hinz et al. (2001); 3) Liu et al. (2005); 4) Liu et al. (2003)

* in the range 0 to 2/7; see §2.2.2

dex $<$ -3) appear to have larger, resolvable disks. A calculation of the Kendall's τ correlation coefficient (Press et al., 1992) for the SED slope vs. disk size relation yields a correlation probability of 94%, whereas the stellar age vs. disk size relation discussed in the previous paragraph yields a correlation probability of 43%. We also see a correlation (87% probability) between the fractional IR luminosity (calculated by M01) and the disk size (Fig. 2.3c).

M01 attributes the difference in the SED between these two groups to disk geometry, with Group I objects displaying a significant amount of flaring outside of the inner disk, while disks in a Group II source have less flaring, a result of shielding from an optically thick inner disk, or perhaps self-shadowing from a puffed up inner wall (Dullemond et al., 2001). It is conceivable that the flaring in the Group I objects results in the disk intercepting more radiation at greater radii, making it easier to spatially resolve the dust disk. M01 correlates the amount of mid-IR excess to the scale height of the disk, with greater excesses a result of more substantial flaring in the disk, consistent with the observed trend in our survey. In contrast, the 10 μm emission in the Group II shadowed disk will be confined to the inner few AU, making it more difficult for resolved emission to be detected. Thus our results are in good agreement with those of Leinert et al. (2004) who found that the mid-IR emitting regions were larger for the redder, Group I objects.

We also note that M01 further subdivides the Group I and II SED classifications into subgroups 'a' and 'b'. These subgroups are determined by the presence or absence of silicate emission bands in the SED. In other words, given a Group Ia and Ib object, both display a large amount of mid-IR excess, but the former includes emission peaks indicative of silicates while the latter does not. The study by M01 does not identify any Group IIb objects, and our nulling sample does not

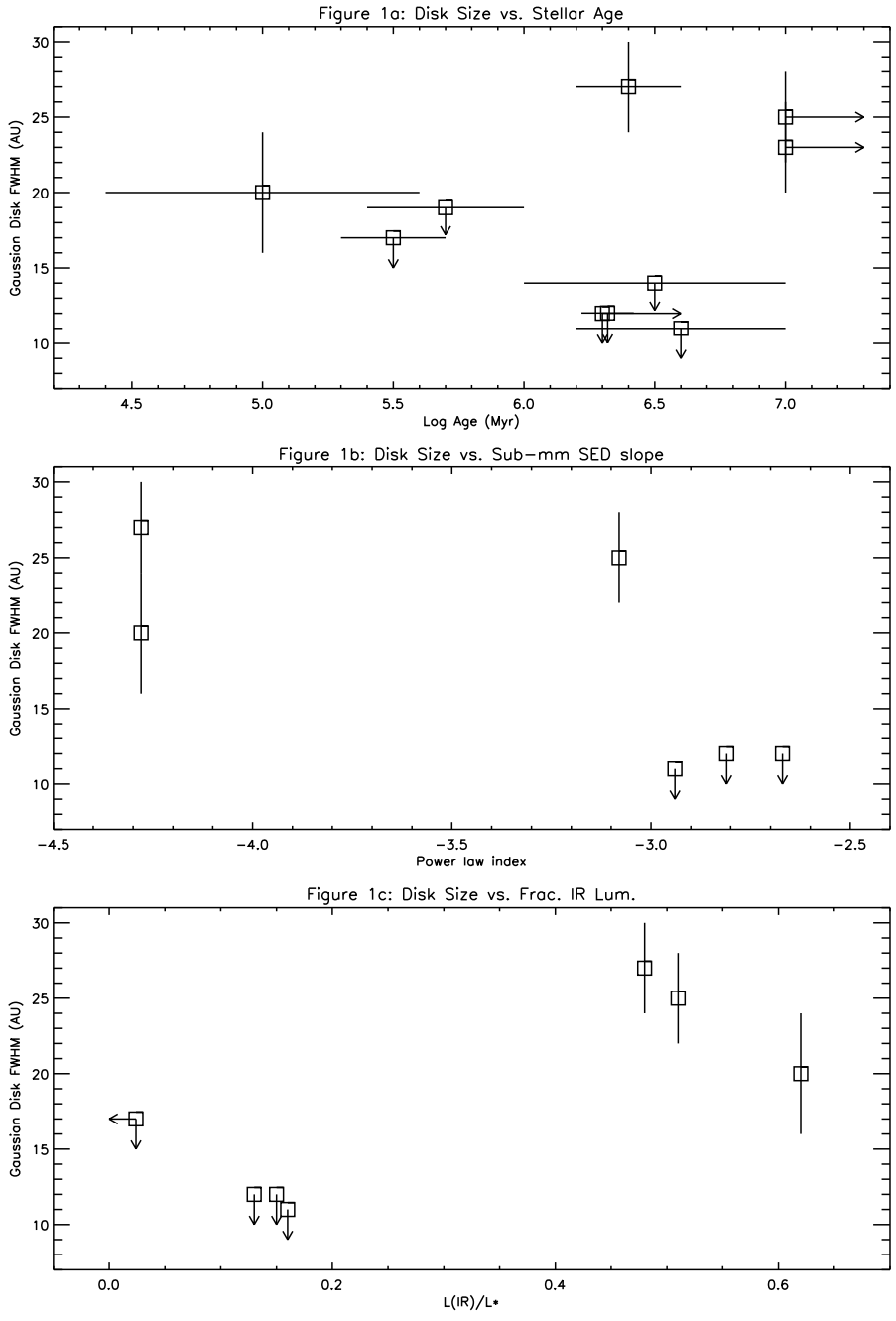

Figure 2.3 **(a)** Disk size (inferred from fitting a Gaussian intensity distribution to the source null) vs. stellar age (for ten objects with age determinations in the literature) for our sample. Sizes plotted are derived from the 11.7 μm observations except AB Aur (10.3 μm) and HD 179218 (10.6 μm). No clear age trend is apparent in the data. **(b)** Disk size vs. sub-mm SED slope (for the six objects with values determined in M01). Objects with steeper SEDs in the sub-mm (index $<$ -3.0) correlate with Group I objects and appear to have larger, resolvable disks. **(c)** Disk size vs. fractional IR luminosity (seven objects from M01). A larger IR excess correlates to larger disk size. Given the poor constraint on the distance to HD 98922, it is not included in any of the plots.

include any Group Ib objects, so we do not make any conclusions regarding the effect of silicate emission on the resolvability of objects. However, if the Group Ib objects have a similar geometry to the Group Ia objects, one might expect Ib objects to be resolvable as well, and would make those objects promising targets for future observations.

Despite the trends outlined above, there is reason to be cautious before attributing the characteristics of the SED groupings to an all-encompassing physical model. M01 make the assertion that Group II objects show evidence that they are more evolved, due to large grain sizes. This would seem to imply that older objects are less likely to be resolved than younger ones, if time is the dominant factor in the evolution of these systems. In our sample, we do not find any trends in resolved objects with age. This would imply that either the age of the system is a poor indicator of the evolutionary state of the system, or that the ages attributed to the stars are in error. We can gain insight into this issue by comparing HD 100546 and AB Aur, the two most conclusively resolved objects. By comparing observations at different wavelengths for each object from this and other studies, we find that the temperature vs. radius relation for the stars is dramatically different. The temperature profile suggests that AB Aur and HD 100546 do not have similar circumstellar environments despite the similarity in the 10 μm resolved emission. The former is consistent with the $T \sim r^{-0.5}$ relation expected from a simple flared disk CG97 while the latter shows evidence for a inner disk gap (see details in §2.4.1 and Liu et al. (2003)). Thus, the evidence here suggests that our ability to resolve an object may be due to different circumstances in each system and cannot necessarily be attributed to similar physical models.

2.4 Results from Individual Resolved Objects

2.4.1 HD 100546

The nearby (∼100 pc) HAe star HD 100546 has been the focus of several studies. This object is perhaps the oldest star in our sample, with an estimated age exceeding 10 Myr (see footnote, Table 2.1). Malfait et al. (1998) characterized the spectrum of the star in the IR, and identified several spectral features indicative of silicate and polycyclic aromatic hydrocarbon (PAH) species in the circumstellar environment. They also found features in the spectrum of HD 100546 to be very similar to those in comet Hale-Bopp, indicating the presence of cometary material in the system, and hypothesize that the system could harbor giant protoplanets to explain the presence of crystalline silicates in the cometary material. The presence of crystalline silicates is also evidence that the system is more evolved than others in our sample. A recent study by Bouwman et al. (2003) found the spectrum of HD 100546 to be dramatically different from other HAe stars, and propose a model with a circumstellar disk with an inner gap of 10 AU and a giant protoplanet. Three studies, Grady et al. (1999); Augereau et al. (2001) and Pantin, Waelkens, & Lagage (2000), used coronagraphic observations at near-IR wavelengths to image the dust disk in scattered light and characterize its spatial structure. These studies detect evidence of an inclined dust disk, and are in good agreement as to its inclination ($\approx 40^\circ$ from face-on), and position angle of its semimajor axis (130° to 160° E of N). Extended emission has also been detected at 3.4 mm (Wilner et al., 2002), and far-ultraviolet observations of warm molecular hydrogen are also consistent with the presence of an inclined disk (Lecavelier des Etangs et al., 2003).

Our observations of this objects were done without AO, and included both nulling interferometric (10.3, 11.7 and 12.5 μm) and direct imaging (11.7, 18.0 and

24.5μm) observations. Nulling data of the object were taken at seven different rotations of the interferometer baseline with respect to the sky in order to probe the geometry of the circumstellar dust (discussed in Section 2.1.2). Thirty-seven sets of 500 frames were taken (2 sets at each combination of wavelength and rotation for all but one of the combinations; see Table 2.2). Direct images were taken with a 3 Hz chop of $8''$ in the horizontal direction of the detector, and a nod of $8''$ in the vertical direction after every 15 s of integration. The 18.0 and 24.5 μm images were taken with the purpose of detecting resolved material at longer wavelengths and characterizing emission from cooler dust. Total integration times were 170 s at 18.0 μm and 210 s at 24.5 μm. Aperture photometry was performed on the direct images of HD 100546 and calibrator stars and relative fluxes for the science object were transformed to absolute fluxes using calibrator fluxes taken from Gezari et al. (1993). The absolute fluxes are 67 Jy at 11.7 μm, 123 Jy at 18.0 μm, and 165 Jy at 24.5 μm, and are good to 10%.

2.4.1.1 Nulling - HD 100546

Our results show that the source null of the object varies as a function of rotation of interferometer baseline with respect to the sky (Figure 2.4). At all three wavelengths, the null varies by a factor of 2 or more and appears to have roughly the same dependence, consistent with the sinusoidal function given in Equation 2.3. Using this function, we perform a fit to the data, resulting in the parameters listed in Table 2.5 and shown as a solid line in the plots in Fig. 2.4.

In order to interpret these fits physically, we have calculated the physical parameters which would yield these fit parameters for two simple disk distributions: an inclined Gaussian disk and a ring. Table 2.6 shows the best fit physical parameters for the nulling data. The best fit position angle of the semimajor axis of the disk is 140° to 160° (E of N), which is in agreement with the values derived

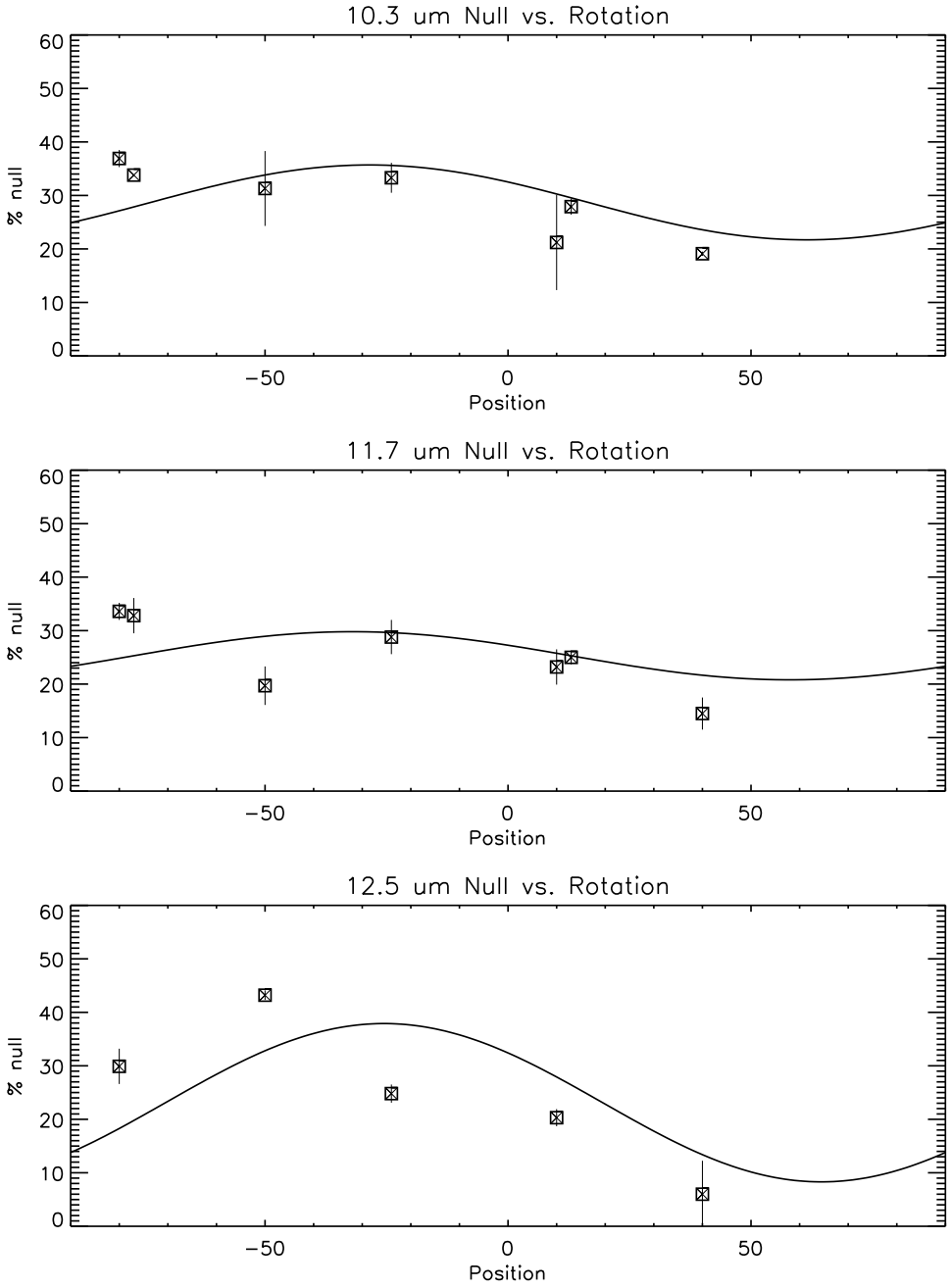

Figure 2.4 Source null vs. position angle for the three wavelengths of nulling observations (top to bottom: 10.3 μm, 11.7 μm, and 12.5 μm) The solid line indicates the best fit curve with the functional form $S = a + bsin(PA + \theta)$ as described in §2.1.2

Table 2.5. Best fit Sine Function Parameters for HD 100546

Parameter	10.3 μm	11.7 μm	12.5 μm
a	0.287	0.253	0.231
b	0.070	0.045	0.148
PA (E of N)	147	154	141

Table 2.6. Physical Parameters of HD 100546 Disk from Nulling Data

λ (μm)	FWHM (Gauss.)	Inclination (Gauss.)	Diameter (Ring)	Incl. (Ring)	PA (°)
10.3	24 AU	40°	26 AU	37°	147
11.7	25	34	27	32	154
12.5	30	63	33	60	141

from near-IR coronagraphic studies (Grady et al., 1999; Augereau et al., 2001; Pantin, Waelkens, & Lagage, 2000). The inclination of the disk at 10.3 and 11.7 μm is derived to be 30° to 40° from face-on, also in agreement with the aforementioned studies, but these fits are only marginally better than a face-on disk when comparing the reduced χ^2 (= 1.5 and 2.2 for the 10.3 and 11.7 μm fits, respectively) of the fits. The 12.5 μm data show a larger amplitude in the variation of the null, hence the inclination derived is greater, $\approx 60^\circ$ from face-on. In this case, there is significant inclination of the disk, as the fit yields reduced $\chi^2 = 2.4$ as opposed to 7.5 for a face-on disk.

The multiwavelength nature of our observations also allow us to probe dif-

ferences between the distribution of different species (silicates, PAH, etc.) and the thermal continuum. Our observations at 10.3 μm and 11.7 μm probe emission from silicates and PAH species, while the continuum emission is roughly probed by the 12.5 μm band (Malfait et al., 1998), although the bandpass of this filter may result in significant emission from PAH and silicates. Our results indicate that the emitting structure is more inclined at 12.5 μm than at the other two wavelengths. This suggests that emission from the thermal continuum may have a more inclined structure than the flux from emission lines of silicates and PAH.

2.4.1.2 Direct Imaging - HD 100546

The 11.7 μm images verify the presence of resolved emission detected in the nulling data. The images of HD 100546 show an average full-width at half-maximum (FWHM) of $\sim 0.5''$, while the calibrator star shows a FWHM about 20% smaller. This implies a disk size of about 30 AU, which confirms the disk sizes derived from the nulling data.

The 18.0 and 24.5 μm direct images show evidence for extended emission as well, with the FWHM values for HD 100546 images on average about 8 - 10% larger than those of the calibrator stars. In order to determine the spatial extent of the extended emission, we constructed an artificial source by convolving an artificial face-on disk signature in the form of a two-dimensional Gaussian, with the PSF from the calibrator star. The artificial image was subtracted from the actual image of HD 100546. The width of the artificial Gaussian disk was varied in steps of 0.1 pix (equivalently $0.012''$, or 1.2 AU at 100 pc). We adopt the disk size which resulted in the smallest residual when subtracted from the image of HD 100546. Figure 2.5 shows a typical image before and after subtractions of the artificial source, plotted with the same greyscale. The top-left image shows HD 100546 at 24.5 μm in an unsubtracted image. The top-right image shows

Table 2.7. Results from Direct Imaging

λ (μm)	Disk FWHM (pix)	Angular size (arcsec)	Physical size (AU)
18.0	2.85 ± 0.20	0.34 ± 0.02	34 ± 2
24.5	3.55 ± 0.20	0.43 ± 0.02	43 ± 2

the subtracted frame with the smallest residual. The center frames shows the subtraction residuals where the Gaussian disk was about 0.5 pix (FWHM) too small (left), and too large (right). Table 2.7 shows the results of the model fitting at each wavelength. The disk size adopted for each wavelength is the average of the sizes determined from the observations at the two epochs, with the error bars adopted as the difference in sizes derived for the two epochs.

At these wavelengths, we are probing both the thermal continuum and emission from silicates. As expected from cooler dust, the 24.5 μm emission extends farther out than the 18.0 μm dust. We do note the 24.5 μm band contains a strong emission line from silicates (Malfait et al., 1998) that may contribute significantly on top of the thermal emission. The images also show that there may be evidence for an inclined disk in the subtracted images, as the best subtracted image still shows a roughly symmetric oversubtraction above and below the center of the star. In images at both wavelengths and both epochs, the residuals showed this type of symmetric structure, with peak of the positive residuals on a line orthogonal to the trough of the negative residuals (see center panels, Fig. 2.5). This structure in the residuals would be expected if the image of HD 100546 was slightly elliptical, perhaps as a result of a resolved inclined disk. We attempted

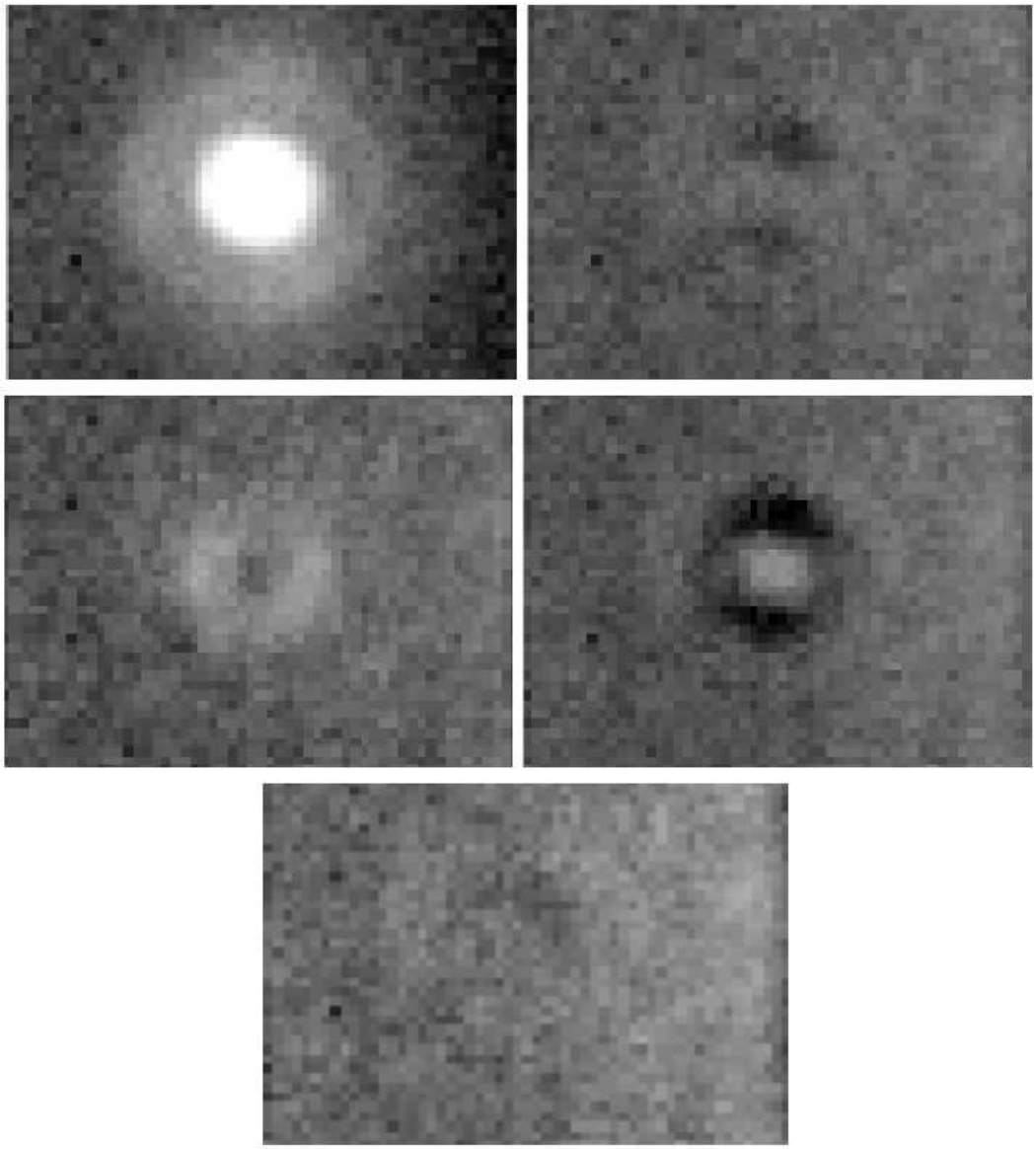

Figure 2.5 *Top-left*: 24.5 μm image of HD 100546, 60 s integration. *Top-right*: Residual from the best subtraction of an artificial image (with a face-on disk). *Center-left*: Residual resulting from an artificial disk 0.5 pix (FWHM) too small. *Center-right*: Residual from an artificial disk 0.5 pix too large. *Bottom*: Residual from a subtraction of an artificial source with an inclined disk.

subtractions with artificial sources incorporating an inclined (and rotated) Gaussian disk, rather than a face-on disk. The bottom panel of Figure 2.5 shows the outcome of this subtraction, resulting in a smaller residual than the best subtraction with a face-on disk (top-right panel). The position angle of the artificial disk was changed in steps of 10°, and the inclination was varied in steps of 5° in order to determine the orientation of the artificial disk which resulted in the smallest residual when subtracted from the image of HD 100546. The position angle of the semimajor axis was found to be between 130° and 170°, and the inclination was 30° to 40° from face-on, all roughly consistent with the orientation derived by previous studies in the near-IR (Augereau et al., 2001; Pantin, Waelkens, & Lagage, 2000; Grady et al., 1999).

2.4.1.3 Discussion - HD 100546

We are confident that we have resolved circumstellar emission from HD 100546 at all wavelengths probed in our observations. We wish to compare the physical parameters we have derived for this emission to current models for the circumstellar environments of Herbig Ae stars. Recent models we consider include those described in the Introduction. While observations at all three wavelengths show evidence for an inclined disk, our observations at 10.3 and 11.7 μm are also consistent with a face-on or spherical emitting body. However, the 12.5 μm null variation does provide convincing evidence for an inclined disk. Furthermore, the derived sizes at these wavelengths are increasing with increasing wavelength (equivalently, decreasing temperature), as one might expect. Somewhat puzzling are the derived sizes of the 18.0 and 24.5 μm disks. One would expect the thermal emission at these longer wavelengths to be spatially several times larger than the emission at the shorter wavelengths. If the source of the emission is a geometrically flat or continuous flared disk, this relation would be given by T $\sim$ $r^{-0.75}$ or

T $\sim$ $r^{-0.4}$, respectively (Chiang & Goldreich, 1997). However, the disks at 18.0 and 24.5 μm show that the relative sizes of the emission regions do not fall within this range (Figure 2.6.

This discrepancy suggests that a continuous disk that extends all the way into the dust sublimation radius may not be an accurate model for the detected emission. Instead we prefer a model with a large inner disk gap, possibly cleared out by a giant protoplanet, as suggested in Bouwman et al. (2003). This would result in the shorter wavelength emission being detected further from the star than expected from a continuous disk, and make the relative sizes of the 10 and 20 μm disks more similar than expected from a T $\sim$ $r^{-0.5}$ relation. Regardless of the clearing mechanism, the lack of dusty material in the inner system points toward a evolution in the disk where clearing proceeds from the inside and moves outward.

Here we also consider the possibility that the relative sizes of the emission regions may be a consequence of an inner self-shadowed region in the disk, instead of an actual physical clearing. In the models of Dullemond et al. (2001), one sees that for the shadowing to extend out to the radii of the detected 10 μm emission (>10 AU), the height of the inner rim would have to be enhanced relative to the height expected, due to direct normal incidence radiation. If this was the case, the models also predict a significant decrease in the strength of the 10μm emission feature. As HD 100546 shows a strong emission feature, it appears that self-shadowing is not a significant effect in determining the relative sizes of the the resolved emission regions in this system. The relatively large source nulls of HD 100546 suggestive a moderate degree of flaring even with the smallest grain sizes. This result supports the fact that self-shadowing is not a factor in the regions we observe and is also in agreement with the SED analysis of Bouwman et

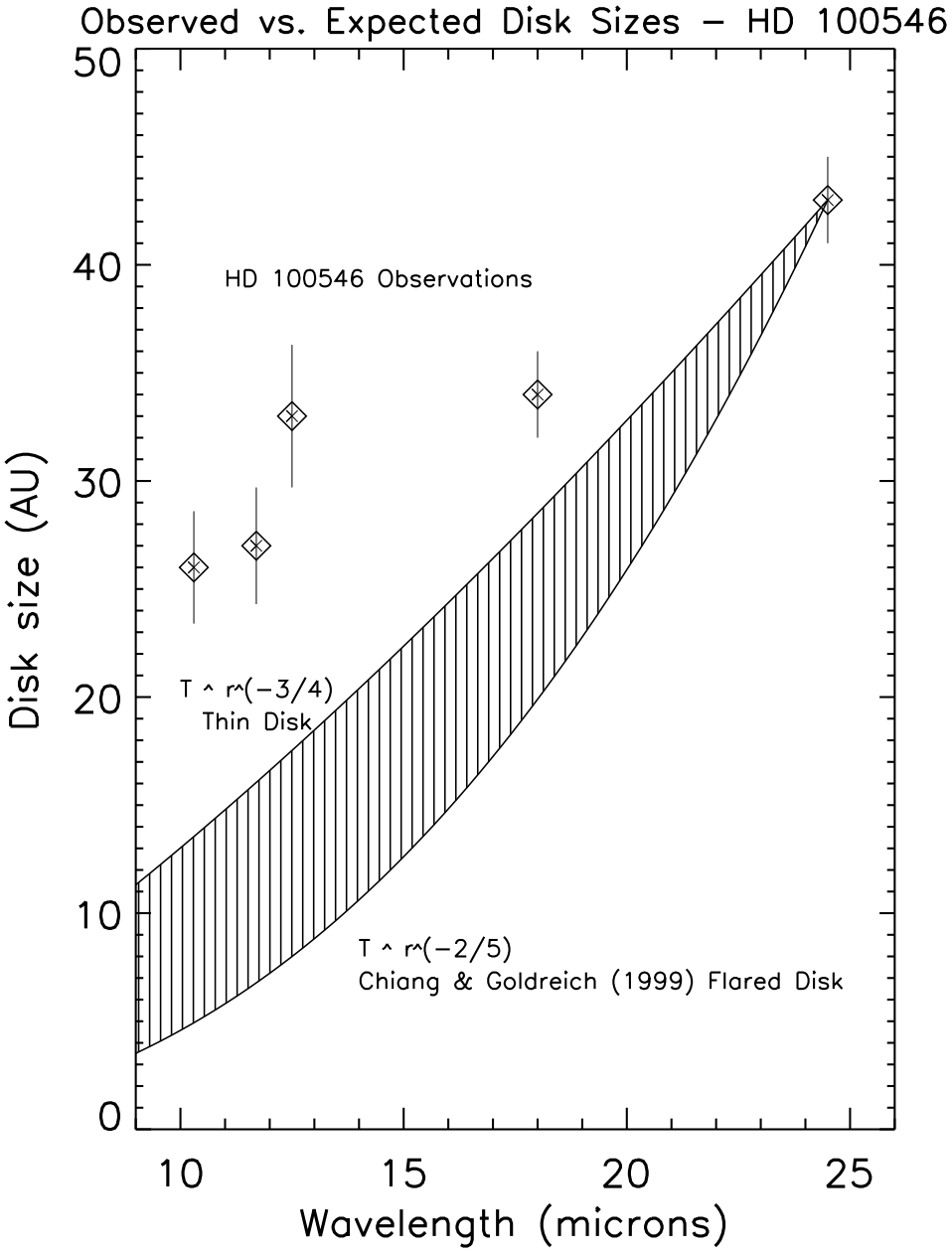

Figure 2.6 The data points show the sizes of the emission regions inferred from observations at each wavelength. The shaded region represents the expected size vs. wavelength relation, bounded by a geometrically flat and a flared disk. The observations and models are normalized to the 24.5 μm point.

al. (2003), which implies that the vertical height of the disk must be enhanced at ~ 10 AU.

2.4.2 AB Aurigae

The star AB Aurigae (A0; $d = 144$ pc (van den Ancker et al., 1998)) has been the subject of many studies based upon observations at several different wavelengths. The star has an estimated age of 2-5 Myr (Mannings & Sargent, 1997; van den Ancker et al., 1998), significantly younger and less evolved than HD 100546, supported by the fact that its SED shows no evidence for crystalline silicates (M01). Near-IR emission from the AB Aur circumstellar region has been observed, probing thermal emission in the inner AU of the disk using long-baseline interferometry (Eisner et al., 2003; Millan-Gabet et al., 2001). Both studies suggest the presence of a slightly inclined distribution of dust with an empty or optically thin inner region (i.e., a ring-like structure). Another recent study in the near-IR has detected scattered light from the disk at greater separations (out to 580 AU) and finds the disk to have a small inclination (Fukagawa et al., 2004). Observations in the mid-IR suggest evidence for resolved circumstellar material at 12 and 18μm at several tens of AU from the star (Chen & Jura, 2003; Marsh et al., 1995). Longer wavelength observations of AB Aur in the millimeter were shown to have spatially resolved molecular line emission at a few hundred AU (Mannings & Sargent, 1997). Reflection nebulosity has also been detected in the optical by Grady et al. (1999) who find material out to 1300 AU and a disk inclination of less than $45°$.

Observations of AB Aur at 10.3 μm (N-band) with AO were taken at 5 different rotations of the interferometer baseline, with every rotation showing spatially resolved circumstellar dust (Figure 2.7). Like HD 100546, the nulls at each rotation show a variation consistent with the presence of an inclined disk. The source

null for each rotation and corresponding position angle are listed in Table 2.3 for each of three different calibrations of the data (see next paragraph). A plot of the data are shown in Figure 2.8.

Observations of the calibrator star, β Gem, were taken before and after the observations of AB Aur. The calibrator shows a significant change in the level of null we were able to achieve during the observations, due probably to changes in observing conditions and the effectiveness of AO wavefront correction. As a result, we calibrate our data (calculate the source nulls) for AB Aur in three different ways to determine how this affects the results. The different calibrations are as follows: 1) We use the first calibrator measurement to calculate all the source nulls; 2) We use a linear fit (in time) between the two calibrator measurements to calculate the source nulls; 3) We use the last calibration to calculate all the source nulls.

All three methods of calibration yield a result in which the dust distribution is significantly more resolved in one PA ($\approx 30^\circ$) than another offset by 90° ($\approx 120^\circ$). This result is suggestive of a flattened or elongated structure as the source of mid-IR excess emission. Assuming two simple brightness distributions (a Gaussian disk and a ring), physical parameters are derived from the fits to the source null vs. position angle (Table 2.8). For each model we have derived the size and inclination of the material needed to reproduce the null vs. position angle profile we have observed. This is repeated for each of the three calibrations, allowing us to assess the error introduced by the calibration issues described above. All three calibrations yield similar results and indicate that the 10.3 μm emission originates from a separation 12 to 17 AU from the star. The presumed disk has a significant inclination, 45 to 65 degrees from face-on and the position angle (PA) of the major axis of the disk is $30^\circ \pm 15^\circ$. If the actual distribution of warm dust is a combination

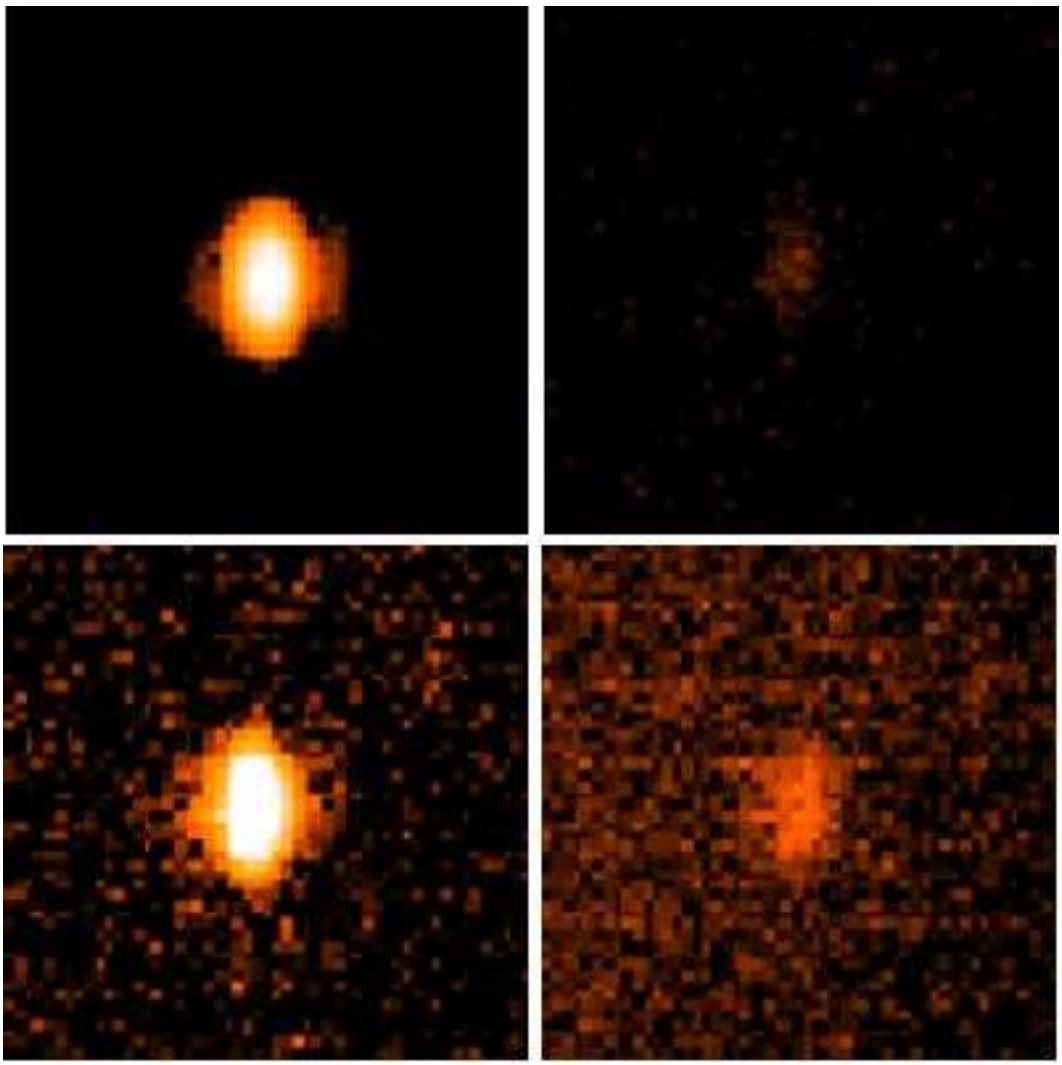

Figure 2.7 *Top panels:* Constructive and destructively interfered images of a point source calibrator star (β Gem) showing a residual flux of 5 %. *Bottom panels:* The same as above for AB Aur. The residual in the destructive image is 26% of the full flux and indicative of spatially resolved emission. The elongation in the images are due to the elliptical subapertures.

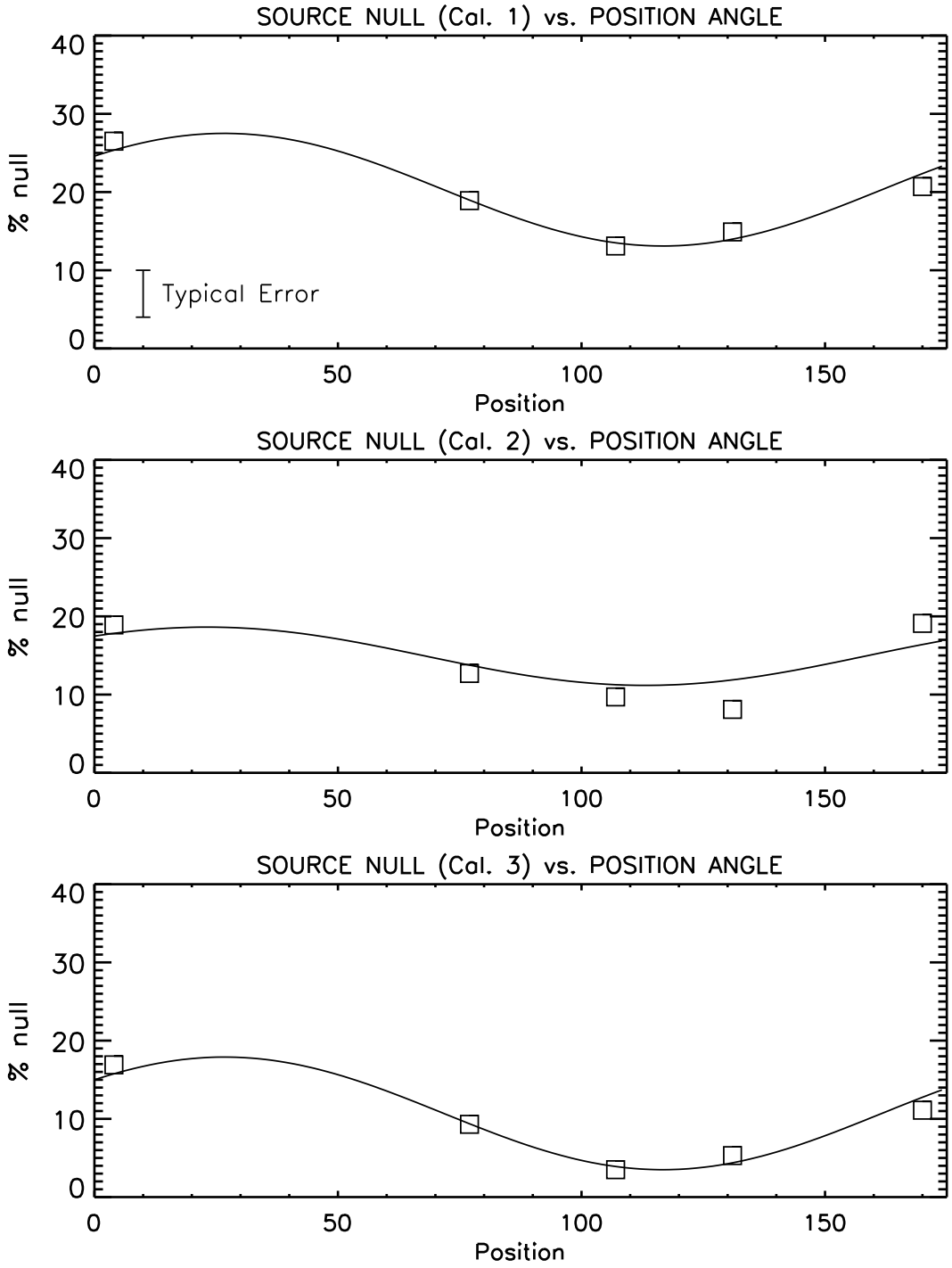

Figure 2.8 Source nulls vs. rotation of interferometer baseline derived for AB Aur for each of three calibrations described in the text. The variation in null is consistent with the presence of an inclined disk.

Table 2.8. Derived Parameters for AB Aur Disk

Cal. Set	Guassian FWHM (AU)	Incl.(°)	Ring Diameter (AU)	Incl.(°)
1	30 ± 3	47 ± 5	34 ± 3	45 ± 5
2	27 ± 3	52 ± 5	30 ± 3	50 ± 5
3	24 ± 2	64 ± 6	28 ± 3	63 ± 6

of a flattened structure and a uniform symmetric component (such as a disk plus envelope), then the disk component would need to be more inclined to account for the amplitude in null variation.

Previous studies have also observed AB Aur at mid-IR wavelengths. Chen & Jura (2003) used the Keck I telescope to observe the star at 11.7 and 18.7 μm. They find that it is marginally resolved at the longer wavelength. At 18.7 μm, they find an angular diameter of about 1″ at the half-maximum flux level. This suggests that the 18 μm emission is originating from a separation of about 70 AU, several times greater than the 10 μm emission. A study by Marsh et al. (1995) finds evidence for resolved emission at 11.7 and 17.9 μm and derives diameters of 40 and 80 AU for the emission, respectively. Taking into account the derived size scales from this and both previous mid-IR studies (separations of 12-17 AU, 20 AU, and 40-70 AU for the 10.3, 11.7, and 18 μm emission, respectively), we note that the wavelength vs. separation profile agrees with the radial temperature profile expected for a flared disk, $T \sim r^{-1/2}$ (Chiang & Goldreich, 1997), assuming that the emission is primarily thermal in nature. We also note that the near-IR study of (Millan-Gabet et al., 2001) finds that the thermal 2μm disk size is about

0.7 AU, which is also roughly consistent with a continuous flared disk.

Studies at other wavelengths include near-IR studies (e.g. Fukagawa et al. (2004); Eisner et al. (2003)), and millimeter observations (Natta et al., 2001; Mannings & Sargent, 1997). Mannings & Sargent (1997) found that AB Aur is resolved in molecular line emission at 3 mm. They find a major axis PA of 79° with an inclination of 76° from face-on. The significant inclination of the disk agrees with the derived inclination of this study. However more recent studies in the millimeter (Natta et al., 2001, and references therein) cite a much smaller inclination ($< 30^\circ$). A recent near-IR study by Fukagawa et al. (2004) using AO coronagraphic observations finds a scattered light disk in H-band with a PA of 58° and a significantly smaller inclination of 30° from face-on. Eisner et al. (2003) used the Palomar Testbed Interferometer to obtain K-band observations of inner (< 0.5 AU) disk surrounding AB Aur and find the inclination to be small, within 30° of face-on, in agreement with Fukagawa et al. (2004). The observations of this study suggest a greater inclination for the mid-IR emission. One also notes that the major axis PA derived for the mid-IR emission in this study differs significantly (50-70°) from previous studies both in the near-IR and millimeter. This points to a difference in geometry for the dust between the inner (a few AU) and outer (hundreds of AU) system. The biggest difference between this study and those at other wavelengths is in the inclination of the disk. Previous studies at several different wavelengths all agree on a significantly smaller inclination than found by this study. This, in combination with the discrepancies in the PA of the disk suggest that the structure may be more complex than a disk alone, where emission at different wavelengths are dominated by material with a different distribution. Significant substructure in the disk at large spatial scales has been detected by Fukagawa et al. (2004) and may also play a role if this substructure is also present

on smaller scales (i.e., the detected null vs. PA signature may be a result of and elongated structure other than an inclined disk).

2.4.3 HD 179218

One of the most distant object in our sample (244 pc; Perryman et al. (1997)), the SED of this object shows significant levels of crystalline silicates (M01), evidence for an advanced evolutionary state. Initial observations without AO failed to resolve this star, resulting in a source null of $3 \pm 3\%$ at a PA of 162° (Hinz et al., 2001). Given the greater precision with the use of AO, follow-up observations were made in 2005 June. These follow-up observations have positively detected resolved emission at a levels from 3 to 7% (0.7 to 1.6 Jy). A plot of source null vs. PA is shown in Fig. 2.9. An average of the source nulls implies a FWHM of 20 ± 4 AU for the Gaussian disk model or diameter of 27 ± 5 AU for a ring distribution of dust. The low source nulls may also suggest flaring in the dust which is small; significantly less than the vertical hydrostatic equilibrium case. The S vs. rotation relation does not show significant variation, consistent with circular symmetry, though significant inclinations cannot be ruled out, as a hypothetical disk with an inclination of 45° results in a variation in the source null of about 3%, within the errors of the measurement. The presence of significant silicate emission in the ISO spectra of M01 also seems to rule out a large inclination for the object, which would result in a drop off in emission intensity at wavelengths shorter than about 10 μm (Chiang & Goldreich, 1999). However, we do not make any definite conclusions regarding the spatial orientation of the dust.

2.4.4 V892 Tauri

V892 Tau is a HAe star located in the Taurus-Auriga star forming region, at a distance of about 140 pc (Elias, 1978). Near-IR speckle interferometry of the star

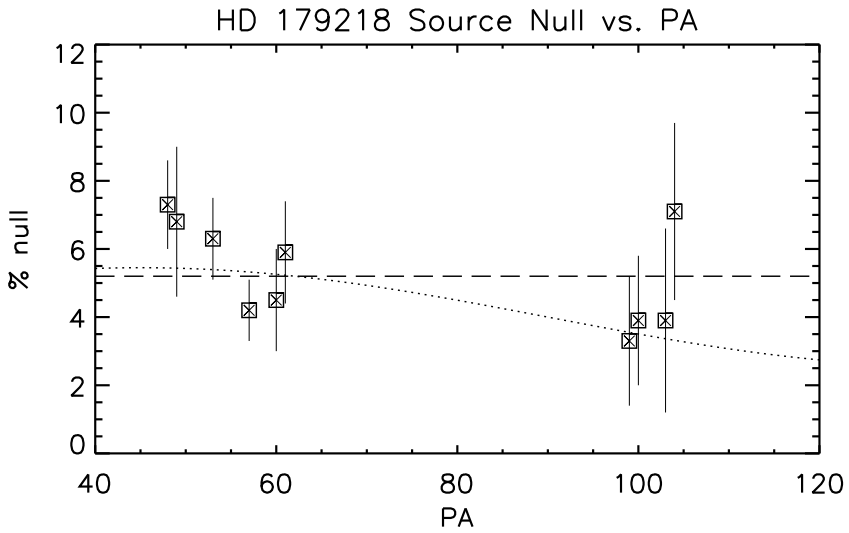

Figure 2.9 Source null vs. PA for HD 179218, spatially resolved with AO observations. The horizontal dashed line is the mean of the measurements, and expected signature (no variation in null vs. PA) from a circularly symmetric source. The dotted line shows the expected variation in null for a 20 AU diameter, Gaussian intensity distribution inclined at $45°$.

revealed an elongated structure with a PA of $90°$. The source of emission is speculated to be either a highly inclined disk or a bipolar outflow (Haas, Leinert, & Richichi, 1997). Observations at 11.7μm without AO, and at 10.3μm, using AO, show resolved emission at a level of about 3 Jy from this source. The emission is detected at a PA of $164°$, but no information can be derived as to the overall orientation of the emission, as data was taken at only one rotation. Using an average of the source nulls obtained in the two data sets at 11.7 μm and assuming a Gaussian intensity distribution for the dust, the FWHM is 18-28 AU. The ring distribution yields a diameter of 25-37 AU. At 10.3 μm, these sizes are 12-16 and 17-23 AU, respectively. The relative sizes of the emission at the two wavelengths is consistent within errors to the expected $T \sim r^{-0.5}$ relation for a CG97 flared disk, assuming purely thermal emission. Signs of flaring can also be inferred from the higher level of resolved emission in the 11.7 μm observations, but, when considering flaring as the sole factor affecting the extent of the emission region, suggests that the dust lies in a flatter distribution than the vertical hydrostatic equilibrium case, though this may also be an indication of larger grains.

2.4.5 R Coronae Australis

This object was observed without AO at Magellan I and shows marginal evidence for resolved emission. The object was observed at two rotations of the interferometer and one of the two rotations yielded a positive detection at the 2σ level. The level of resolved emission is 8% and suggests a spatial extent for the dust of 15 ± 4 AU using a Gaussian dust distribution and 20 ± 4 AU using a ring distribution. As with V892 Tau, the source nulls are possibly indicative of less flaring than a hydrostatic equilibrium situation would expect, or larger grains than ISM sizes.

CHAPTER 3

OBSERVATIONS OF MAIN SEQUENCE STARS

This chapter describes observations of main sequence stars. The primary purpose of these observations is the characterization of their debris disks. Specifically, we wish to establish dust densities and distributions (or, in the case of non-detections, their limits) in order to infer the physical processes which govern the evolution of circumstellar matter at a spatial scale corresponding to the habitable zones of these systems. We interpret the source nulls determined in the observations by using a scaled zodiacal dust model based upon Kelsall et al. (1998) to infer a dust density (or limit on density). When combined with results from theoretical models of dust evolution (Dominik & Decin, 2003) and other observational studies at different wavelengths, the observations presented here provide an important part of interpreting the history of debris in each system. I first describe our observational methods and data reduction procedures. I then present results and discuss physical interpretations for the data in the context of previous results, both for the sample as a whole and for individual objects in our sample.

3.1 Observations and Data Reduction

3.1.1 Target Selection

The targets of this study were chosen to maximize the chances to spatially resolve a warm debris disk, as well as take advantage of previous observations of the objects at different wavelengths (i.e., our high spatial resolution 10 μm observations will complement observations that already exist in the literature). Five of the 6 objects are intrinsically luminous (A or F-type), so that the circumstellar debris will be heated out to a large radius. Assuming a blackbody grain temperature

law of $T_g = 278 L_*^{1/4} r_{AU}^{-1/2}$ (Backman & Paresce, 1993), the habitable zone should lie at separations ranging from 4 to 7 AU. Objects within 40 pc are chosen for the same reason (ability to spatially resolve the emission), and all objects have 10 μm fluxes greater than 1 Jy to ensure sensitivity to the object. Finally, each of the A-type stars has a 24 μm excess detected by Spitzer (Rieke et al., 2005), which make them ideal candidates for 10 μm observations to complement the longer wavelength observations, thus giving a more complete picture of the circumstellar dust at different spatial scales. Also included in the target list is the K-type star ϵ Eri. The star lies at a distance of 3 pc, making a hypothetical 10 μm disk around the star resolvable. Previous studies have found that the star has 25, 60, and 100 μm excess detected by *IRAS* (Backman & Paresce, 1993; Silverstone, 2000). The final target, γ Ser has no detected 25 μm excess, but does have a 60 μm excess detected by *IRAS* (Backman & Paresce, 1993). The complete list of targets is shown in Table 3.1.

Observations of the six main sequence targets were made between 2003 May and 2006 June at the MMT 6.5 m telescope. All observations of these objects made use of the MMT's adaptive optics secondary, with the additional benefits described in §1.3.3. The configuration and setup of the BLINC-MIRAC instrument were otherwise identical to observations described in previous chapters. Images were taken in the N-band (10.6 μm, 50% bandpass). Due to the increased stability in null afforded by AO, integrations were generally 1 s per frame (compared to the 50 ms frames needed for non-AO observations), resulting in a signal-to-noise in a full flux image of 20 for a 10 Jy source. The procedure for observations was the same as those for AO observations of Herbig Ae objects; in this case, we take 3 sets of 10 frames (a total of 30 s integration) on the object tuned to destructive interference, followed by 10 frames of the object in constructive interference. After

Table 3.1. Main Sequence Target List

Name	Alt. Name	Spec. Type	d (pc)	Est. Ages (Myr)	Refs.*
α CrB	Alphecca, HD 139006	A0	23	350	1,2,3
α Lyr	Vega, HD 172167	A0	7.8	365	1,2,3
β Leo	Denebola, HD 102647	A3	12	50, 520	1,2,3
γ Ser	HD 142860	F6	11	1600, 3200	1,2,4
ϵ Eri	HD 22049	K2	3.2	800	1,2,5
ζ Lep	HD 38678	A2	22	180, 231, 330	1,2,3 and 4

Note. — * - Spectral Type, distance, and age references, respectively.

References- 1) SIMBAD; 2) Perryman et al. (1997); 3) Rieke et al. (2005) and ref. therein; 4) Chen et al. (2006) and ref. therein; 5) Benedict et al. (2006) and ref. therein

three repetitions of this sequence, a set of 10 off-source sky frames is taken with the same integration time per frame. This procedure is repeated as many times as possible for both science objects and point source calibrator stars, allowing for overhead spent for the operation of the AO system. In general, observations of each science object are limited to one or two rotations of the interferometer baseline. Table 3.2 lists the dates and number of nulled frames taken for each object.

Determining the nulls for the main sequence objects was not as straightforward for this sample compared to observations of Herbig Ae stars. This was because, except for Vega, the objects were faint enough that, when destructively interfered, the image of the object dropped below the noise level in the frames, or the signal-to-noise of the image was so poor that accurate photometry could not be extracted. For this reason, we used a combination of techniques in order

Table 3.2. Main Sequence Summary of Observations

Star	Dates	# Destr. Frames
α CrB	2005 June 26	60
α Lyr	2003 May 10-12	140
β Leo	2005 June 26, 2006 Feb. 11	660
γ Ser	2006 June 17-18	150
ϵ Eri	2006 Feb. 11	150
ζ Lep	2006 Feb. 11	30

to assess an upper limit on the instrumental null for the five objects in question. The first technique used to estimate the upper limit on the null was a series of artificial star tests. Artificial stars were created using the constructively interfered images of the object and scaled to a percentage of the full flux. The artificial star was then added to the data frame, to see if the star was detectable over the noise of the frame. This was repeated for artificial stars of increasing flux until the level of the noise could be assessed. Figure 3.1 shows an example of an artificial star added to a data frame with a destructive image of ζ Lep.

For those stars for which there were a large number of frames taken, we stacked the frames in order to improve the signal-to-noise. In some cases this allowed us to estimate an instrumental null for the object. Finally, we used the signal-to-noise in the constructively interfered frame to estimate the null that would be detectable in a destructive frame (i.e., if the full flux frame has a signal-to-noise of 10, we estimate that any null greater than 10% would be measurable).

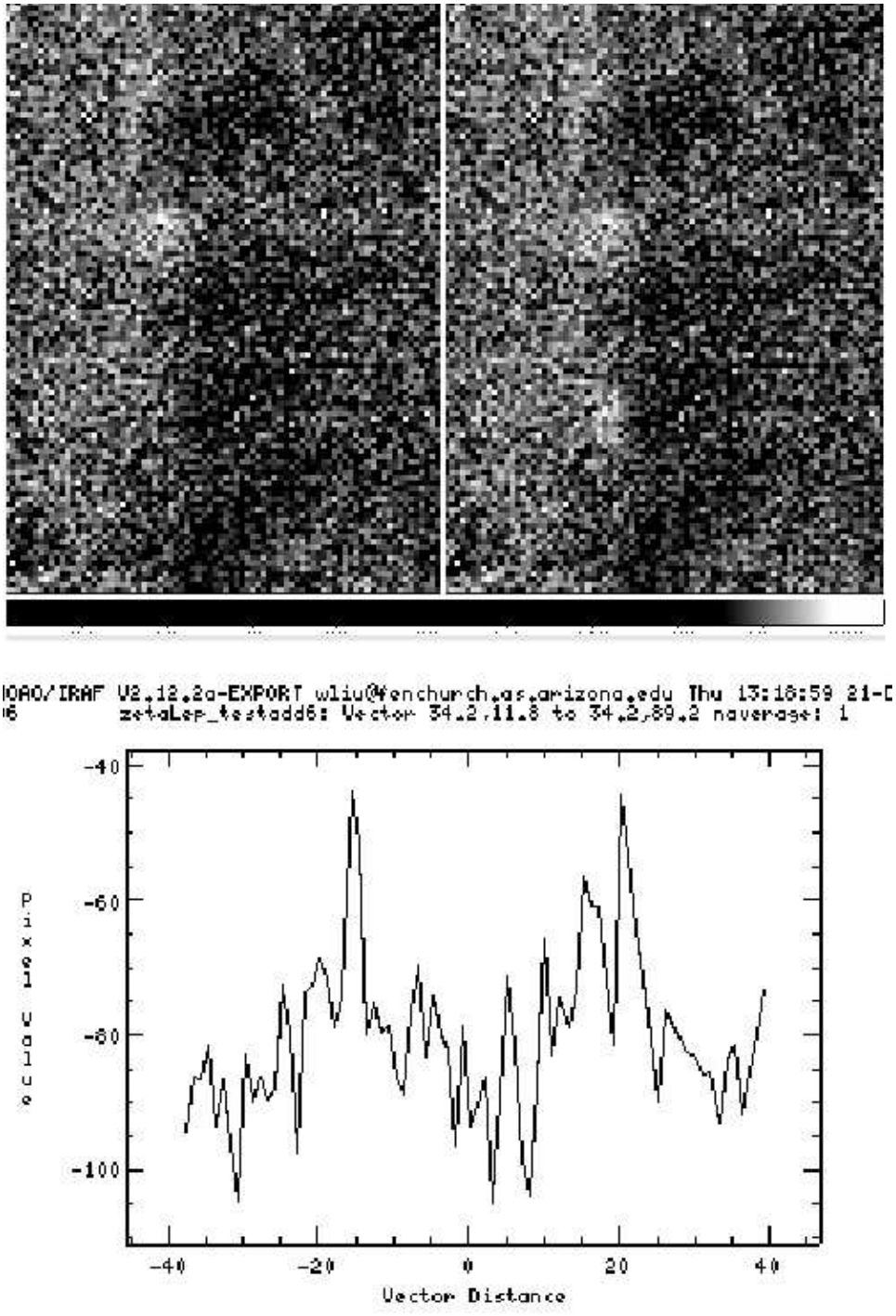

Figure 3.1 *Top panel:* The original nulled image of ζ Lep (left), and one with an artificial star added below the actual image (right). The artificial star has a flux of 10 % of the full flux of the star. *Bottom panel:* A vertical cut through both the artificial image (left peak) and the actual image (right peak).

The latter is the least accurate and precise of all the techniques used and provides only a very rough estimate of the upper limit on the instrumental null. Table 3.3 shows the instrumental and source nulls achieved for each object (science and calibrator), along with the method used to assess the null.

For the objects in this sample, many with much fainter 10 μm fluxes than the Herbig Ae objects (well below 10 Jy), the noise level becomes significant, thus the precision of photometry is affected. Improvements in wavefront correction with AO has also decreased phase variation, making the photometric error the larger contributor to the error in many cases. A typical example of error contributions is seen in the observations of γ Ser, which has a error in source null of $\pm 2.6\%$. This value is derived by adding in quadrature the contributions from the photometric error ($\pm 2.2\%$) and the phase variation ($\pm 1.4\%$).

3.2 Results from the Full Sample

The source nulls for all six objects show no spatially resolved circumstellar emission. The upper limits in the source nulls represent different upper limits for warm habitable zone dust density in each system. In order to assess these dust density limits, we use a scaled solar zodiacal dust model based upon Kelsall et al. (1998, see Appendix C).

The Kelsall et al. (1998) zodiacal dust model incorporates several components to model our solar system's inner dust, including a "smooth cloud" component as well as several dusty asteroid rings. For the purpose of this analysis we consider only the smooth cloud component, which dominates the detectable dust. This component is an optically thin cloud with a power law falloff in density with increasing separation from the star and a dependence of $r^{-1.3}$. Additionally the cloud has a vertical density profile which decreases exponentially with increasing

Table 3.3. Main Sequence Nulls

Name	Date	Method[1]	Instrumental Null (%)	Calibrator 1 Null[2]	Cal. 2 Null	Source Null
α CrB	2005 Jun	S	15 ± 4	6.2 ± 0.1	N/A	8.8 ± 4
"	2005 Jun	E	10 ± 4	6.2 ± 0.1	N/A	4 ± 4
α Lyr	2003 May	N	3.7 ± 0.7	3.6 ± 0.5	3.4 ± 0.4	0.2 ± 0.7
β Leo	2006 Feb.	N	4.6 ± 2.3	5.8 ± 0.7	4.9 ± 0.8	-0.8 ± 2.4
"	2006 June	S	4.0 ± 1.2	3.6 ± 0.4	3.4 ± 0.4	0.5 ± 1.3
γ Ser	2006 June	A	5.9 ± 2.6	2.8 ± 0.1	4.6 ± 0.2	2.2 ± 2.6
ϵ Eri	2006 Feb.	A	3 ± 2	4.5 ± 0.4	3.5 ± 0.5	-1 ± 2
"	2006 Feb.	E	6 ± 2	4.5 ± 0.4	3.5 ± 0.5	2 ± 2
ζ Lep	2006 Feb.	A	10 ± 5	3.5 ± 0.5	4.6 ± 0.3	6 ± 6

Note. — 1 - N: Normal reduction procedure; A: Artificial star tests; S: Stacked frames; E: Signal-to-noise estimate

2 - All calibrator nulls assessed using normal reduction procedure. Cal. 1 data were taken before the science object, Cal. 2 were taken after.

height from the midplane (Kelsall et al., 1998, eqns. 6 and 7). For our model we set the inner boundary of the cloud at the dust sublimation radius and the outer boundary at 10 AU, outside the 10 μm emitting region for our objects.

This model was used to predict the flux from an exozodiacal cloud surrounding each star and convolved with the transmission function of the nulling interferometer in order to simulate the observed null. Stellar parameters (e.g., M_*, R_*, L_*) adopted for each star were taken to be the typical values for each spectral type, as listed in Cox (2000). Values for the stellar fluxes were adopted to be the IRAS 12 μm fluxes (Backman & Paresce, 1993). The density of the exozodiacal cloud in the model was varied in order to match the output to the actual observed nulls. For the upper limits in source null we use a 3 σ limit; for stars with more than one method used for deriving the null, we use the larger of the two errors. Once a limit on the density was calculated for each star, this was converted to a dust mass. The density limit for each star was converted to an effective emitting area using a value for the solar zodiacal cloud of 1 zody $\approx 10^{21}$ cm^2 multiplied by the factor for the density limit determined using the Kelsall et al. (1998) model described above. For the size distribution of grains, we adopt a power law dependence of

$$n(a)da = n_o a^{-p} \tag{3.1}$$

where n is the number of grains of a given radius a, and p is 3.5 (Mathis et al., 1977; Greenberg & Nolan, 1989). The lower limit for grain size was taken to be the blowout size of each star (Artymowicz, 1988),

$$a_{min} = 3L_* Q_{pr}/16\pi M_* c\rho \tag{3.2}$$

where $Q_{pr} \approx 1$ and ρ is the density of grain material, taken to be 2.5 g/cm^3 (Grun et al., 1985). The upper limit used in the calculation of dust mass was 1000 μm.

Thus the masses derived can be considered as the upper limit for the total mass found in grains smaller than 1 mm. The derived values for the total disk mass depend on the largest size of grain (or planetesimal) considered. If the size of the largest object is increased by a factor of 10^6 to 1 km; the total mass will increase by a factor of about 10^3. The total emitting surface area remains roughly the same. In other words, the total surface area of debris is dominated by small grains, but the the total mass is dominated by the largest bodies. Values for the dust density, blowout size and dust mass can be found in Table 3.4. We find the 3 σ source null upper limits generally correspond to densities of 10^3 to 10^4 Zody and dust masses on the order of $10^{-6} M_{\oplus}$.

In addition, we estimate the limit for fractional dust luminosity $f_d = L_{dust}/L_*$ by assuming 1 Zody = 10^{-7} in f_d (Beichman et al., 2005). These values are also listed in Table 3.4, and the values are in the range of $f_d = 10^{-3}$ to 10^{-4}.

A further analysis can be made by comparing the observed limits on dust to an estimate of the expected density of our own zodiacal dust *at the age of each observed star*. In this way we can compare "apples to apples" with regard to stellar age. For a collisionally replenished disk with a dust removal timescale much shorter than the lifetime of the system, we expect $f_d \sim t^{-2}$ for a Poynting-Robertson drag dominated disk (Spangler et al., 2001). Using this relation we find that the density of solar system zodiacal dust at the age of Vega (365 Myr), for example, would be 150 Zody. Our limit of 500 Zody results in a limit on warm dust in the Vega system of about 3.3 times our own zodiacal dust, after accounting for dust evolution. If the fractional dust luminosity follows a evolutionary trend of $f_d \sim t^{-1}$ for a disk dominated by collisional removal of grains as predicted in Dominik & Decin (2003), we would expect a dust limit of about 41 times solar. Table 3.5 shows the density of dust in each system as a factor of solar level, after

Table 3.4. Derived Limits on Dust Properties Using a Scaled Zody Model

Name	Null Limit (%)	Density (Zody)	Surf. Area (cm^2)	a_{min} (μm)	Mass[1] ($M_\oplus$)	f_d
α CrB	12	1.2×10^4	1.2×10^{25}	4.3	5.4×10^{-5}	1.2×10^{-3}
α Lyr	2.1	5.0×10^2	5.0×10^{23}	4.3	2.2×10^{-6}	5.0×10^{-5}
β Leo	7.2	1.7×10^3	1.7×10^{24}	1.9	1.0×10^{-6}	1.7×10^{-4}
γ Ser	7.8	1.5×10^4	1.5×10^{25}	0.5	4.7×10^{-6}	1.5×10^{-3}
ϵ Eri	6.0	7.5×10^3	7.5×10^{24}	0.1	1.0×10^{-6}	7.5×10^{-4}
ζ Lep	18	2.2×10^4	2.2×10^{25}	1.8	1.3×10^{-5}	2.2×10^{-3}

Note. — 1 - Grains ranging in size from blowout size to 1 millimeter, assuming the dust lies between the dust sublimation radius and 10 AU.

Table 3.5. Evolution Adjusted Dust Limits (Multiples of Solar Level)

Name	$f_d \sim t^{-2}$	$f_d \sim t^{-1}$
α CrB	73	930
α Lyr	3.3	41
β Leo	6.8	110
γ Ser	4.3×10^3	8.0×10^3
ϵ Eri	240	1.3×10^3
ζ Lep	56	1.1×10^3

accounting for dust evolution. For stars with multiple age determinations, an average was used.

As mentioned above in the description of the target selection criteria, all targets have excesses detected at longer wavelengths by previous studies. The amounts of long wavelength dust emission varies across the sample. The A-stars in the sample all had fairly large 24 μm excesses, reported in Rieke et al. (2005), of 29%, 15%, 42% and 143% above the stellar photospheric level, for α CrB, α Lyr, β Leo, and ζ Lep respectively. If these same excesses were present at 10 μm, they would have been easily detected with our nulling observations. Since this is not the case, we can infer that these systems are relatively clear of material in the inner system (i.e., a few AU in separation) compared to larger radii. A further discussion of the well studied debris disks around Vega and ζ Lep is contained in the sections below. The star γ Ser is somewhat puzzling, as it had an significant excess at 60 μm detected by *IRAS*, with no excess at 25 or 100 μm. However, re-

cent *Spitzer* MIPS observations at 70 μm failed to find any excess emission. This would seem to suggest that the positive detection by *IRAS* may have been due to confusion from its large beam size. If this is the case, then it would point toward the γ Ser system to be devoid of solid debris at a range of spatial scales, from a few to hundreds of AU. Finally, ϵ Eri has a well established debris disk detected at submillimeter wavelengths containing a large quantity of material (several earth masses) at radii of tens of AU. Again, this implies the existence of a clearing process keeping the inner system relatively devoid of material. We examine this star in depth in the section below.

To assess the physical scale of the inner clearing in the five systems with confirmed excess at longer wavelengths, we again use an optically thin, scaled solar zodiacal dust model based on Kelsall et al. (1998). The model is scaled up to a density which corresponds to the positive detection of excess at longer wavelengths. For the four A-stars, this is the excess reported in Rieke et al. (2005) for 24 μm emission. For ϵ Eri, we adopt the 25 μm excess detected by *IRAS*. We then introduce an artificial inner edge to the disk (replacing the dust sublimation radius) and vary the radius of the inner edge to match the detection limit of the nulling observations. For the purposes of this analysis, the outer radius of the disk is set to 80 AU, roughly 2 to 3 times the radius at which one would expect the 24 μm to peak for the A-stars. This is very likely to be an over simplified model, as will become evident in §3.3 below, but gives us a rough scale for the (minimum) inner clearing sizes in these systems. The values of the derived inner gap radius for each star are listed in Table 3.6 and can be interpreted as a minimum value. The source null derived using the model is fairly sensitive to changes in the inner hole size. As a typical example, changing the hole size of the β Leo disk by $\pm 10\%$ results in a range of source nulls between and 5.5 and 10.3 %, corresponding to a

Table 3.6. Derived Inner Gap Sizes

Name	Excess Ratio[1]	Min. r_{hole} (AU)
α CrB	1.29	13
α Lyr	1.15	13
β Leo	1.42	12
ϵ Eri	1.12	2.5
ζ Lep	2.43	26

Note. — 1 - 24 μm excess detected by *Spitzer* and reported by (Rieke et al., 2005), except for ϵ Eri which uses the 25 μm excess measured by *IRAS* and reported in Backman & Paresce (1993).

2 σ error in the null.

Finally, a more general treatment of an optically thin disk can be made, following the model of Mamajek et al. (2002), which incorporates spherical grains of a single size, $< a >= 5a_{min}/3$, which represents an average size for the power-law size distribution described above. The grains lie in an annular distribution from the dust sublimation radius out to a radius where there is no longer significant 10 μm emission (about 25 AU for A-type stars). The derived parameters for dust mass and fractional dust luminosity are shown in Table 3.7, and generally agree to within an order of magnitude of the levels of dust found using a scaled

Table 3.7. Limits on Dust Properties (using General Opt. Thin Model[1])

Name	$< a >$ (μm)	Mass ($M_\oplus$)	f_d
α CrB	9.2	1.5×10^{-5}	1.7×10^{-4}
α Lyr	9.2	2.2×10^{-6}	2.5×10^{-5}
β Leo	4.0	1.2×10^{-6}	6.7×10^{-5}
γ Ser	0.9	5.7×10^{-7}	2.5×10^{-4}
ϵ Eri	0.1	2.4×10^{-7}	4.7×10^{-4}
ζ Lep	3.8	3.4×10^{-6}	2.0×10^{-4}

Note. — 1 - Mamajek et al. (2002)

zodiacal disk model above.

The lack of warm debris in the main sequence sample is perhaps not surprising, in light of recent observational and theoretical results. A recent N-band photometric survey of 14 T Tauri stars in the Tucana-Horologium association finds that none has a significant excess (Mamajek et al., 2004). Assuming an optically thin disk, this constrains the mass in the inner 10 AU of these systems to less than $10^{-6} M_\oplus$, similar to the mass limits established for the sample in this study. As the Tuc-Hor stars have lower masses than many of the objects in the nulling sample presented in this dissertation, this appears to be evidence that debris clearing is common in all main sequence stars. Furthermore, the ages of the T Tauri sample in the Mamajek et al. study ($\sim$30 Myr, an order of magnitude or more younger than the nulling sample) implies that debris clearing in the inner system occurs

relatively early in the main sequence lifetime, even in low mass stars where it is reasonable to believe that radiation pressure forces would be less of a factor than in the A-stars observed with nulling. Thus, one might expect that the stars observed in this study would have no detection of exozodiacal dust. Theoretical models for solar mass stars show that 10 μm excesses peak for stars during terrestrial planet formation, at less than 1 Myr, and then drop off significantly after that, becoming undetectable by current techniques by 10 Myr (Kenyon & Bromley, 2004). This result appears to be similar to models of debris around intermediate-mass stars with ages ranging from 10^8 to 10^9 yr, which predict excesses at 10 μm to be a factor of 10^{-2} to 10^{-3} times the stellar photosphere at that wavelength (Kenyon, private communication). Thus we find our observations to be consistent with the current models for dust evolution, and previous observational results.

3.3 Results from Individual Objects

In this section we consider three of the objects in our sample which have debris disks which are well studied at longer wavelengths, α Lyr, ϵ Eri, and ζ Lep. For each system, we examine the recent literature and attempt to build a picture of the debris, describing its distribution and likely physical processes occurring in each system.

3.3.1 Vega (α Lyr)

Vega is one of the closest stellar systems to our own (d=8 pc; Perryman et al. (1997)), intrinsically luminous, and has an age well into the main sequence (365 Myr; Rieke et al. (2005)). The source null derived for Vega is 0.2% $\pm$ 0.7% (1 σ error), consistent with zero, which indicates that we are not detecting resolved emission at our current levels of sensitivity and spatial resolution (Figure 3.2)

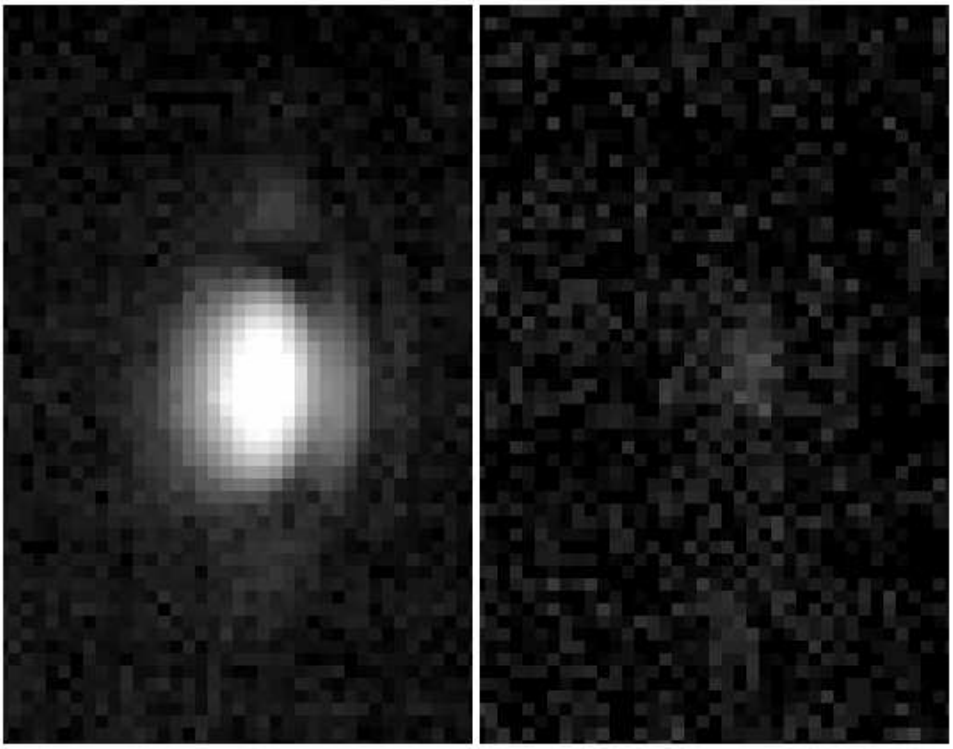

Figure 3.2 Full flux (left) and nulled (right) images of Vega. The source null calculated for this object was 0.7%.

This allows us to place constraints on the distribution and amount of exozodiacal dust surrounding Vega. We are confident (3 σ) that there is no resolved emission at 10.6 μm around Vega above the 2.1% level (0.9 Jy) outside of 0.8 AU from the star. The Kelsall model would result in a nulled flux of 1.8 mJy (or 0.0042% of Vega's flux) if placed at the distance of Vega. Scaling up this solar model to our 3 σ source null limit for Vega corresponds to a dust density limit of about 500 times our solar system's zodiacal dust. Additionally, we find that the null does not vary significantly with observations at different rotations of the interferometer baseline (over a range of about 90 degrees), indicating that there is no evidence of an inclined disk-like structure.

3.3.1.1 Physical Interpretation in Light of Previous Results

The well studied nature of the debris in the Vega system provides an excellent opportunity to place our 10 μm nulling observations of warm dust in context with dust studies at other wavelengths (hence spatial scales). Recent results from the *Spitzer Space Telescope* have shed light on the distribution of dusty debris in the Vega system, and when viewed together with the nulling results presented here, are illustrative of the power of multi-wavelength observations. Su et al. (2005) has found spatially extended emission indicative of cold dust at wavelengths of 24, 70, and 160 μm. The emission is found to be at separations of 300 to 800 AU, with a circularly symmetric and smooth distribution. They have attributed the presence of dust to a large collisional event, followed by a collisional cascade which produces grains smaller than the blowout size. These grains would then be removed by radiation pressure blowout, populating the outer system to large radii. The total dust mass is inferred to be $\sim 10^{-3}$ $M_{\oplus}$. The results of our observations show a relative dearth of material in the inner few AU of the system. The lack of material in the inner system would seem to support the fact that the

vast majority of the grains are collisionally broken down to smaller than blowout size and subsequently pushed outward. However, the presence of a low density of dust removed by P-R drag, or the presence of a planetary companion are not ruled out by these observations.

In order to rule out the possibility of a Poynting-Robertson (P-R) drag dominated scenario in the Vega system, we ignore, for the time being, collisional removal of grains and consider only P-R drag removal following the hypothesized collisional event. From P-R drag one may expect that the material from the outer system material would migrate inward and populate inner regions with material, which could be detected at mid-IR wavelengths. If one assumes a conservative value for the excess flux at 25 μm (1.08 Jy, Backman & Paresce (1993), a level of excess corroborated by the recent *Spitzer* observations) and takes the temperature of grains as a function of distance from the star as T $\sim r^{-0.5}$ (Backman & Paresce, 1993), and makes the conservative assumption that the optical depth profile of the circumstellar material is constant with radius [1], one would expect a flux of 11 Jy from blackbody grains at 10 μm. This flux is calculated assuming thermal blackbody emission from the grains by integrating the product of the Planck function and optical depth over the spatial extent of the zodiacal dust [2]. When this signal is observed through the transmission pattern of the interferometer, we estimate the final signal to be over 5 Jy. Using the 60 μm excess (7.75 Jy, Backman & Paresce (1993)), with the same assumptions as above, the calculation yields an even greater detected excess of 470 Jy at 10 μm. These expected 10 μm fluxes

[1] For reference, the solar system's radial optical depth profile is $\sim r^{-0.4}$ in the inner system (r $<$ 30 AU) and $\sim r^{-4}$ for 30 AU $>$ r $>$ 100 (Backman et al., 1997). For our analysis, we assume that the grains are large enough to be considered blackbodies.

[2] We set the inner radius of the disk at the dust sublimation radius of 0.25 AU, corresponding to a temperature of 1500 K, and the outer radius of the disk to the distance at which we expect the thermal emission at a given wavelength to peak given the T vs. r relation in Backman & Paresce (1993). The dust is assumed to be optically thin.

would have been easily detectable with our observations. However, we do not find this large excess, which indicates that the inner region of the Vega system is relatively clear of material compared to the outer region. This appears to be further evidence in support of a collisionally dominated removal of grains in the Vega system, as opposed to one which is dominated by P-R drag. This result is consistent with other previous conclusions (Lagrange et al., 2000; Backman & Paresce, 1993) as well, though our observations are able to better constrain the upper limit of dust density in the Vega system by a factor of ≈ 3.6 times compared to IRAS observations, which provided an upper limit for warm dust density of 1800 times our solar system (Hinz , 2001; Aumann et al., 1984).

We also consider other possible mechanisms for the relative clearing in the inner system. One may draw a comparison to the HR 4796A system which was observed by Jura et al. (1998) to have a similar lack of warm material in the inner system. For the case of HR 4796A, they suggest two possible scenarios for the lack of warm dust in that system: the existence of a companion clearing out material, or the destruction of ice particles by stellar radiation. First, we consider these same explanations for the absence of material in the inner Vega system. For the latter scenario, we would expect water ice to sublimate at temperatures above 110 K (Pollack et al., 1994), and in fact we may already see evidence of this effect in the 25 μm emission which probes temperatures near the sublimation temperature, and shows a smaller than expected excess compared to longer wavelengths. If the lack of material in the inner system is due to sublimation of ice grains, we can constrain the composition of the outer debris disk. To estimate this effect we make the simplifying assumption that each grain is composed of either icy material that sublimates at 110 K and thus is totally destroyed inward of about 45 AU, or silicates/metals grains which remain unaffected. Comparing our derived

upper limit on dust flux at 10 μm (0.9 Jy) and the expected 10 μm flux using the 60 μm excess calculated above (470 Jy), and assuming the density decrease in the inner system is due only to the sublimation of ice grains, this would require that the outer disk is comprised of 99.8% icy material, with a density near 1 g/cm^3, assuming optically thin material. Using the 25 μm excess to estimate the density contrast compared to the inner system, we find that the composition must be about 80% water ice, again if ice sublimation is the only cause of grain removal. For comparison, the large Kuiper Belt Objects Pluto and Charon have densities of roughly 2 g/cm^3 (Luu & Jewitt, 2002), indicating higher fractions of silicate material in our own outer solar system than that of Vega, as determined by this study. This either suggests a significant difference in composition, or points to another explanation for removal of the cold dust as it spirals in.

Another explanation for the lack of dust in the inner system is the presence of a planetary sweeper companion. Previous observations in the millimeter and submillimeter (Wilner et al., 2002; Koerner et al., 2001; Holland et al., 1998) have detected dust in the Vega system at separations between $8''$ and $14''$ from the star (projected separations of 60 to 110 AU). The morphology of the dust is suggested to be the result of a planetary perturber. For example Wilner et al. (2002) suggest a planetary companion of 3 M_{Jup} at a separation of about 50 AU. It is conceivable that such a companion could be responsible for the contrast in density of circumstellar material between the outer and inner system found in this and previous studies. However if one assumes that the temperature of grains follows the relation $T_g \sim r^{-0.5}$ (Backman & Paresce, 1993, Eq. 3), the drop off in mid-infrared excess between the 25 μm IRAS detection and the 10 μm observations in this study indicate a significant density decrease between 10 and 40 AU, suggesting that a planetary companion may be located at a closer separation than suggested by

the millimeter observations. Recent near-infrared adaptive optics observations of Vega by Keck (Macintosh et al., 2003) and the Palomar 5 m (Metchev et al., 2003) have attempted to detect planetary mass companions. These studies found no evidence for a massive ($>$ several M_{Jup}) planetary companion. However, the studies note that they do not probe masses for companions as low as those suggested by the millimeter observations. We also compare our results to those of Ciardi et al. (2001), who find near-infrared emission consistent with a circumstellar debris disk within 4 AU emitting at 3% - 6% of the stellar flux. If we take this to be the case, and assume that the optical depth of material drops off as $r^{-0.4}$ (Backman et al., 1997) out to the 10 μm emitting region, we would expect a signal in the range of 1.5 - 3 Jy at 10 μm, which would have been detected by our observations. We do not find this to be the case, which suggests that if a near-infrared disk is present, there is a steeper drop off in the optical depth of dust than the $r^{-0.4}$ assumed here.

3.3.2 ϵ Eridani

Far-infrared excess was detected by *IRAS* observations at 25, 60 and 100 μm (Backman & Paresce, 1993; Backman & Gillett, 1987; Aumann, 1985), an indication of cold solid material in the circumstellar environment of ϵ Eri. From these initially detected excesses, a disk emitting area of 2.6×10^{-2} AU, or about 5200 Zody was inferred using a simple optically thin ring model (Aumann, 1985). Since these early observations, numerous follow-up observations have been performed at different wavelengths. Greaves et al. (2005) recently observed ϵ Eri at sub-mm wavelengths (450 and 850 μm) and found substantial quantities of dust and substructure in the distribution of the dust at large radii. They find that the cold dust lies in a slightly inclined ring with peak emission at 65 AU (a projected angular separation of about $20''$), and an inner cavity. The mass of the ring is significant

and estimated to be 5 to 9 $M_{\oplus}$, and has substantial substructure (i.e., clumpiness). They favor a scenario with a giant planetary perturber at tens of AU. Epsilon Eri has also been the subject of radial velocity planet searches (Cumming et al., 1999; Walker et al., 1995), with a reported detection of a long period planet in Hatzes et al. (2000). Also characterized by an HST astrometric study by Benedict et al. (2006), the planet is estimated to have a mass of 1.6 M_{Jup}, and a period of about 7 yr, corresponding to a orbital separation of about 3 AU, which is a smaller separation than the planetary perturber predicted by the recent sub-mm observations. Benedict et al. (2006) state that radial velocity data over three decades do show a long period trend consistent with a planetary mass object with a 50 to 100 year object, which would be consistent with cold dust observations.

The density of the cold debris in the ϵ Eri system is high enough that one would expect the disk to be collisionally dominated, instead of P-R drag dominated. From this argument, one would not expect dust in the outer system to migrate inward, so the lack of dust in the habitable zone is not surprising. Another removal mechanism that should be considered is stellar wind (corpuscular) drag, which may have a stronger effect than P-R drag for a late type star (Chen et al., 2006). However, even if corpuscular drag is a significant removal mechanism, the presence of one or more giant planets would keep the inner system relatively clear of debris. Our study probes physical separations of a few tenths of AU out to about 3 AU, a separation consistent with the inner giant planet. Thus it suggests that even if the outer planet is not efficiently removing the large amounts of material in the outer system (a assumption supported by the initially detected mid-IR excesses), the inner planet would keep the habitable zone relatively clear of debris migrating inward from the outer system.

As this star is lower mass than the other stars in our sample, it is perhaps

the best star in our sample to compare to our own solar system. The existence of a giant planet of Jupiter mass at about 3 AU, much like our system, and the existence of cold debris, a Kuiper Belt analog, further warrants comparison to our solar system. The primary debris feature in the inner part of our solar system is the Main Asteroid Belt. The mass of objects in the Main Belt is about 1.8×10^{24} g (Cox, 2000) or $3 \times 10^{-4} M_{\oplus}$. If the derivation of the mass limit for warm debris from our nulling observations was taken to include objects up to 1 km in size, we have an upper limit of about $1 \times 10^{-3} M_{\oplus}$. Thus it is conceivable for a asteroid belt-like distribution of debris in the ϵ Eri system to exist below our detection limits, with masses equivalent to our present-day Main Belt asteroids.

3.3.3 ζ Leporis

This object has also been the subject of several studies. Recently, Rieke et al. (2005) found ζ Lep to have one of the largest 24 μm excess in their sample of 76 A-type main sequence stars, a result which confirms the initial *IRAS* detection (Backman & Paresce, 1993). Mid-infrared observations with large aperture telescopes have also been made recently by Chen & Jura (2001) on Keck I and Moerchen et al. (2007) with Gemini South. Both studies found, using PSF subtraction, that the dust was spatially resolved at about 18 μm but not at 10-12 μm. Various models used to interpret this emission places the longer wavelength emission at less than 9 AU. For the mass of dust grains, Chen & Jura (2001) estimate 1.6×10^{22} g or about $3 \times 10^{-6} M_{\oplus}$ as a lower limit, assuming an average grain size of 2.8 μm. These results for dusty material at 18 μm are consistent with our nulling observations which find an upper limit in dust mass derived from our 10 μm observations of $1.3 \times 10^{-5} M_{\oplus}$. Therefore, if some fraction of the dust detected by the previous studies were to migrate inward, it is likely that it would fall below our detection limit. It is important to note that our derived mass is an upper limit, while the

mass determined in Chen & Jura (2001) is a lower limit based on their assumption of grain size. A larger assumed grain size would result in a larger mass. Thus, it is a possibility that a greater quantity of dust is present at larger radii than probed by our study.

The SED shape of ζ Lep differs from other Vega type excess stars, specifically, ζ Lep shows a hotter SED (i.e., a larger excess at around 20 μm compared to 70 and 100 μm). Thus Rieke et al. (2005) makes the argument, based upon models of Moro-Martín et al. (2005), that the system does not harbor a giant planet, and that the dust is the result of a recent large collisional event, similar to that hypothesized for the Vega system. Given the spatial scale of the dust emission, the collisional event occurred at a smaller separation (several AU) compared to the Vega event (near 100 AU). The observations point toward a different post-collision scenario in the ζ Lep system as well. If collisional removal of grains was dominant, as in the Vega system, one might expect the long wavelength excesses to be greater than observed. ζ Lep is less luminous than Vega by a factor of about 2 or more, with a blowout grain size about one-third that of Vega. It is conceivable that following the collisional event, fewer grains were subject to blowout, resulting in a lower level of long wavelength excess. If the remainder of the grains were to migrate inward due to P-R drag, one may expect some level excess at shorter wavelengths, perhaps on the same order as detected at 20 μm. Our nulling observations do not rule out this scenario.

CHAPTER 4

SUMMARY AND CONCLUSIONS

The observations presented in this dissertation highlight the usefulness of nulling interferometry in observing the optically thick primordial disks surrounding Herbig Ae stars, as well as placing constraints on exozodiacal debris around main sequence stars. The primary results from each chapter are summarized below, followed by a discussion of the implications of the results.

4.1 Summary of Results from the Herbig Ae Sample

We have carried out 10 μm nulling interferometric observations of 13 Herbig Ae stars, and reach the following primary conclusions:

- We have conclusively resolved warm dust surrounding 3 objects, HD 100546, AB Aur, and HD 179218, the latter previously unreported. Both HD 100546 and AB Aur show significant variation in source null vs. PA, which is evidence for an elongated structure such as an inclined disk (Liu et al., 2003, 2005). HD 179218 was resolved in recent (2005 June) observations with AO, and preliminary results suggest little variation of null vs. PA, consistent with an axisymmetric distribution (such as a face-on disk) for the dust, though a significant inclination cannot be ruled out given the errors in the measurement.

- The star HD 100546 shows evidence for a large inner gap inferred from the relative sizes of the emitting regions a five difference wavelengths. This gap is possibly the result of the formation of a giant protoplanet, but regardless of the clearing mechanism, points toward disk clearing occurring from the inside-out.

- We have found evidence for resolved emission around an additional two HAe stars, V892 Tau and R CrA. Both the sources show resolved emission at a

level of a few percent of the unresolved flux at 10 μm.

- The spatial extent of the emitting region in the resolved systems range from 15-30 AU in diameter, assuming two models: a Gaussian disk and a ring.

- Both SED slope and fractional IR luminosity appear to be good indicators of the spatial extent of circumstellar dust. Although our sample size is small, it appears that M01 Group I objects are more resolvable than Group II objects, a result consistent with Leinert et al. (2004). This trend is evident in the correlation between disk size vs. sub-mm spectral slope as well as disk size vs. fractional IR luminosity.

- There is a lack of correlation in disk size vs. stellar age, perhaps due to uncertainty in age determination, and/or the fact that time is not the sole or dominating factor in disk evolution.

- Using a model based on CG97, we evaluate the effect of disk flaring on the resolvability of the objects. We find that a hypothetical object with flaring consistent with vertical hydrostatic equilibrium would produce a very large source null in all objects. This suggests that the flaring is not as significant as expected in these systems. Alternatively, another possible explanation for this discrepancy is the grain size. Since larger, blackbody grains at close separations to the star can mimic the emission from ISM-sized grains in a more extended distribution, the larger grains would need to be more flared in order to account for the same source nulls.

- Follow up AO observations should be made on all objects not yet observed with AO, in order to better constrain the limits, or possibly detect, their spatial extent. Observations of Group Ib objects, those without strong 10 μm silicate emission, would also be interesting to assess any correlation between the presence of these emission lines and the spatial resolvability of the objects, and further con-

strain the distribution and orientation of the disks.

4.2 Summary of Results from the Main Sequence Sample

- We find no spatially resolved warm debris in these systems with upper limits on warm dust between 400 and 10^4 Zody, depending on the individual objects (see Table 3.4). This corresponds to dust masses on the order of 10^{-5} to $10^{-6} M_{\oplus}$.

- For all of the objects, these limits contrast with the presence of dust at longer wavelengths (hence greater separations), implying a clearing in dust in the inner system. This suggests that the inner circumstellar environment around intermediate-mass main sequence stars are generally cleared of dusty debris. This result is similar to that of Mamajek et al. (2004), who observed a sample of low mass objects with younger ages.

- In the Vega system the primary process keeping dust out of the inner system appears to be a collisional cascade and radiation pressure blowout, a hypothesis suggested by Su et al. (2005). The nulling observations presented in this dissertation in combination with *Spitzer* MIPS observations at longer wavelengths appear to support this.

- In the ϵ Eri system, the lack of material in the inner system is consistent with other evidence for giant planets. This would prevent the large quantities of debris detected at tens of AU from migrating inward due to P-R drag and populating the inner few AU and habitable zone. However, our observations do not rule out a small amount of debris inside the inner giant planet, with a total mass equivalent to our solar system's Main Belt asteroids (present-day mass).

- The ζ Lep system may have dust in the 10 μm emitting region consistent with the amount of dust detected at 18 μm (Chen & Jura, 2001; Moerchen et al., 2007). Due to the relatively hot SED (larger mid-IR excess vs. far-IR excess) compared

to other debris disk systems, radiation blowout appears to be less of a factor compared to Vega. This fact is also used by Rieke et al. (2005) to speculate that the system lacks a giant planet. If this is indeed the case, a large collisional event may be responsible for populating the circumstellar environment with dust. Our observations do not rule out the possibility that some fraction of this dust migrated inward and is present in the habitable zone. This make ζ Lep an ideal candidate for follow-up nulling observations once suppression levels are improved.

4.3 Implications for Star and Planet Formation and Future Observations

4.3.1 The Herbig Ae Sample

One of the more interesting objects in the sample, and perhaps the one with the most to contribute to the implications of early stellar evolution is HD 100546. This is an object which is believed to be chronologically older than many of its counterparts, and also shows signs for evolution in the disk. It is interesting to note that it shares several characteristics with another well studied member of the sample, AB Aur, such as large fractional IR luminosity and long wavelength SED slope, both indications of disk flaring. SED studies have shown the star to shares many features with the comet Hale-Bopp as well as compositional gradients suggestive of collisional processes occurring in the disk (Bouwman et al., 2003; Malfait et al., 1998). Such evidence has fueled speculation of a giant protoplanet in the system, a hypothesis which is perhaps supported by the evidence uncovered by observations carried out in this study. Since chronological age determinations are notoriously imprecise for pre-main sequence stars, we must ask the question if HD 100546 is a typical of the group, existing at a stage which all Herbig Ae stars will eventually pass through, or if the unique conditions in the system are mimicking an object with different characteristics, (e.g,, the large in-

ner gap and irradiation of an inner rim producing a large mid-IR excess similar to that displayed by an object with pronounced disk flaring). The latter seems to be most plausible, given the preponderance of the evidence from observations in this study as well as the mid-IR spectral studies. The reason for revisiting this particular case is to highlight the fact that each system appears to have its own unique history, and that any classification of these objects into groups should be based upon evidence from a variety of wavelengths and techniques and not just one or two gross characteristics. Increasing the sample size to include more objects with mid-IR spectra or obtaining mid-IR spectral follow-up on objects already observed with high spatial resolution techniques appears to be key in deciphering questions such as how common systems like HD 100546 are.

Increasing the sample size of nulling targets will be achievable in the years to come with the continued improvement of nulling interferometry. The immediate scientific impact of nulling interferometry can be maximized by observing objects that are well studied, but lack high spatial resolution observations at 10 μm. In this way we can piece together the unique history of each system. As nulling develops to larger apertures, longer baselines, and better phase control, the sample size of objects can be expanded to more distant Herbig Ae stars, their lower mass counterparts, T Tauri stars, which demand increased sensitivity and spatial resolution.

The following plots examine the potential for resolving objects with different geometries and greater distances with improvements in the nulling contrast ratio. First, we examine the resolvability of M01 Group II sources, which would have smaller 10 μm emission regions than those of Group I sources. The expected source nulls as a function of emission region size are plotted for different distances. This is done fore two different geometries, a Gaussian intensity

distribution (Fig. 4.1) and a uniform intensity annulus (Fig. 4.2). The horizontal dashed line represents our current 3σ best null achieved for a science object (2.1%) with adaptive optics. We find that achieving a source null of 1% would allow us to detect the nearest disks with sizes down to 4-5 AU in diameter, while disks at several hundred pc must be well over 10-15 AU in diameter to be resolvable. Further improvement of contrast ratios of 1000 or greater would allow one to spatially resolve even the smallest emission regions ($\sim$1 AU) for a large range of distances. In general ring structures are less resolvable than Gaussian disks of comparable size, which is expected due to a relative decrease in emission in a ring compared to a continuous disk.

We also examine the resolvability of hypothetical CG97 disks that have a flaring parameter of zero (i.e., constant H/a) over a range of distances and stellar luminosities. Figure 4.3 shows the expected null for a unflared CG97 disk at different distances, for three spectral types. The 2.1% best null is again shown as a horizontal dashed line. The most luminous Herbig Ae disks are currently resolvable out to about 200 pc with our current limits, with a 1% allowing resolvability out to 300 pc. Less luminous unflared disks are currently unresolvable, but improvement in the contrast ratio by an order of magnitude would allow spatial resolvability over a wide range of distances.

Finally, we explore the possibility of spatially resolving later-type pre-main sequence objects, or T Tauri stars. From Figure 4.3 above, the expected source null from a G or K-type star with a flat disk would be well under 1%. For example, a hypothetical K0 star at 150 pc and flaring would require a 6.4% null to spatially resolve the object, using a CG97 flared disk model. Such an object would be resolvable with current contrast levels achieved at the MMT with AO. An unflared disk would require a null of about 0.5%, or a contrast level a factor of

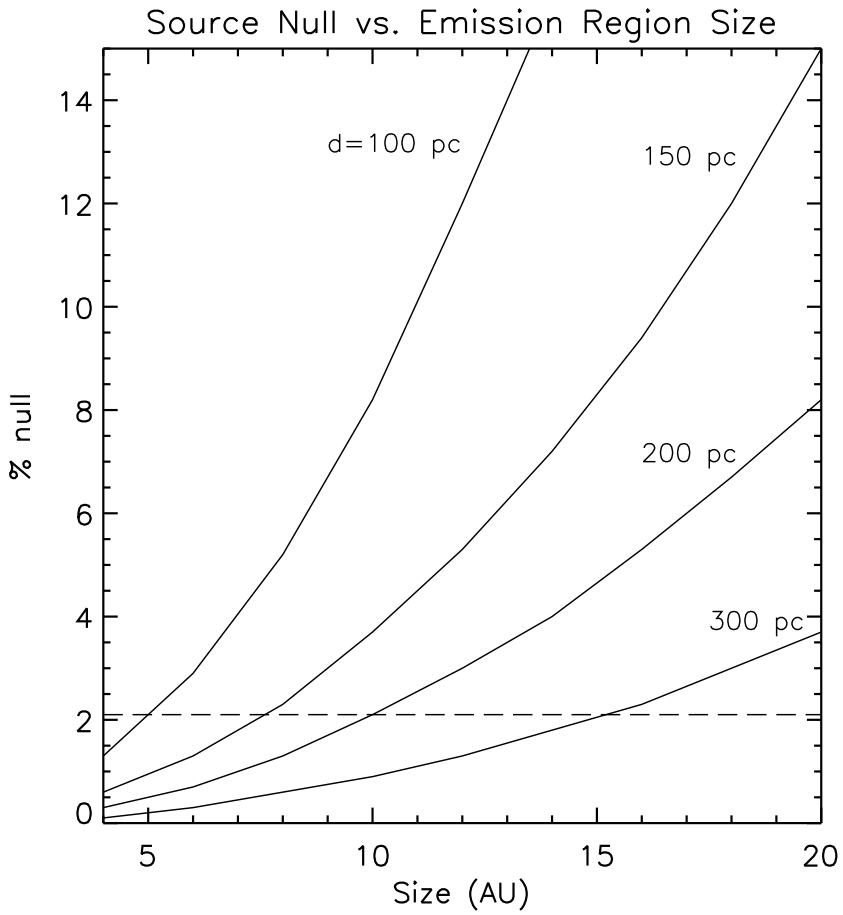

Figure 4.1 Expected source nulls for emission regions with sizes less than 20 AU in diameter (Group II sources) with a Gaussian intensity distribution. The horizonatal dashed line represents the best 3σ limit achieved on a science object to date (2.1%).

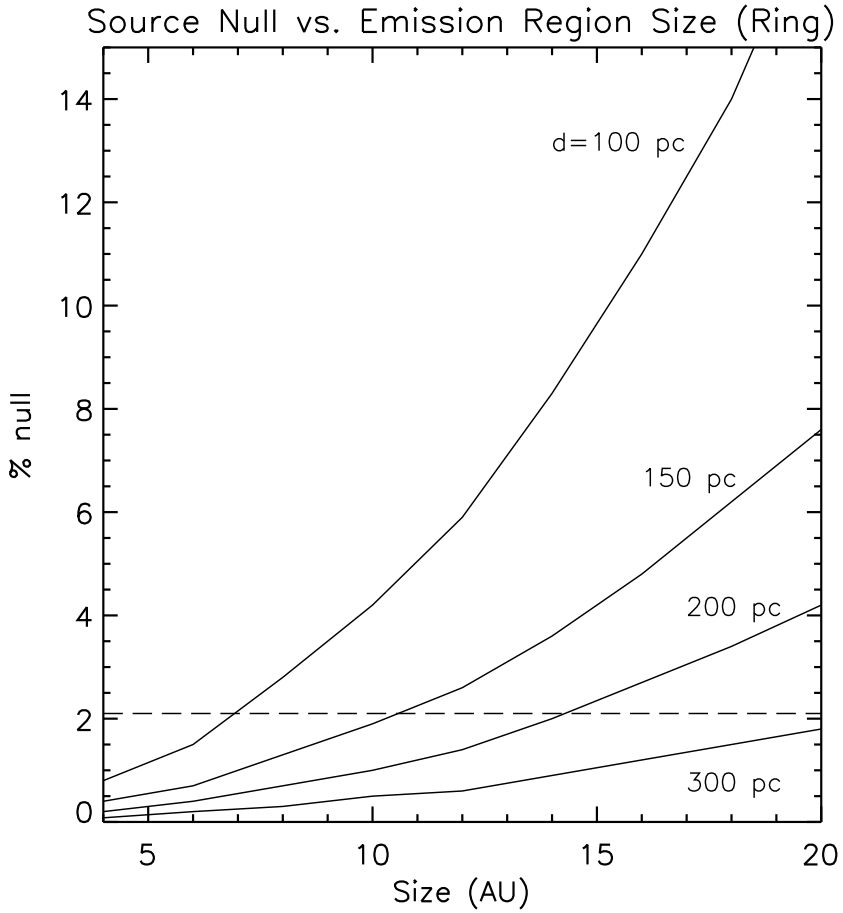

Figure 4.2 Expected source nulls for emission regions with sizes less than 20 AU in diameter (Group II sources) with a uniform ring distribution. The horizonatal dashed line represents the best 3σ limit achieved on a science object to date (2.1%).

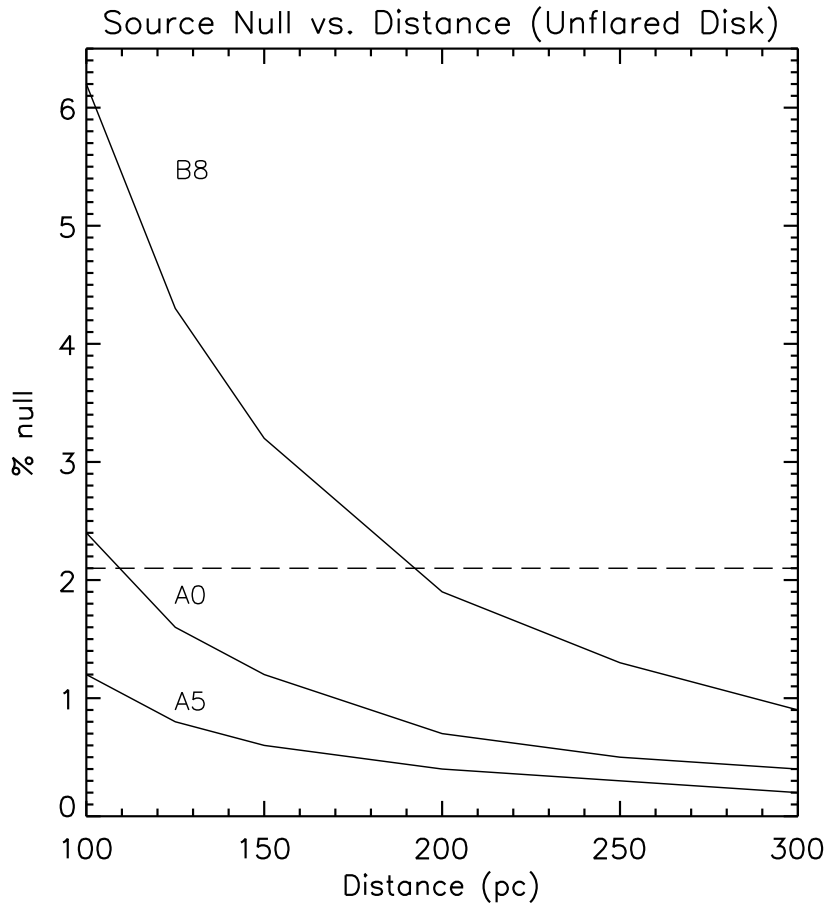

Figure 4.3 Expected source nulls for CG97 disks with a flaring parameter of zero. he horizonatal dashed line represents the best 3σ limit achieved on a science object to date (2.1%).

4 better than what has currently been achieved. The development of BLINC's internal phase control loop should allow one to achieve the contrast levels needed to observe these objects. Older objects, such as transition disks, are expected to be more evolved and perhaps have undergone significant grain growth and settling. Thus the high contrast levels needed to detect flatter distributions of dust are necessary to observe these objects.

4.3.2 The Main Sequence Sample

For the three well studied debris disks in our sample (Vega, ϵ Eri and ζ Lep), we again find that each system has a story to tell. Like the Herbig Ae sample, the value of our 10 μm nulling observations achieve their greatest scientific potential when view in context of previous observations of each individual object. For Vega and ϵ Eri, we find the inner system (on scales of a few AU) to be relatively clear of material compared to larger spatial scales. However, despite this superficial similarity, a closer examination of the evidence show different processes occurring in each system.

In the Vega system, there is strong evidence for a large collisional event and subsequent collisional cascade at many tens of AU, which breaks the solid material down to sub-blowout sizes. The large luminosity of the parent star makes the blowout size relatively large, thus making removal of the grains more efficient and complete. In this particular case, the nulling observations are confirmation of the *Spitzer* observations presented in Su et al. (2005). It is also interesting to note that sub-mm observations of Vega's circumstellar environment show dusty substructure consistent with a giant planetary perturber (Wilner et al., 2002; Koerner et al., 2001; Holland et al., 1998). This suggests that even if a small fraction of grains are present in the inner system, they may be removed dynamically by a giant planet. In the case of ϵ Eri, the density of material detected a longer wave-

lengths also suggests a collisionally dominated regime. There is also considerable evidence in the literature for at least one giant planet, including one existing in the inner system at about 3 AU, at physical separations identical to those probed by our dust observations. The lack of material in the inner couple of AU may also be a result of planetary "sweepers" opening gaps in the debris field, if other removal mechanisms, such as corpuscular drag, have a significant effect. The removal of the dust is rather dramatic, as sub-mm observations show evidence for several $M_{\oplus}$ of dust, compared to our derived upper limit of about $10^{-6} M_{\oplus}$.

The third system, ζ Lep, displays characteristics similar to those of the Vega system in terms of a relatively massive belt of material exterior to the habitable zone. Unlike the Vega and ϵ Eri systems, however, there is no evidence for giant planets. On the contrary Rieke et al. (2005) contend that the SED shape suggests that a planet does not exist in the system. If this is the case, a large collisional event and cascade and radiation blowout would appear to be important for the production and subsequent removal of the dust. However, the relatively hot SED of the system appears to contradict a significant amount of dust removal via radiation blowout. It is a possibility given the less luminous nature of ζ Lep compared to Vega, that P-R drag may play a greater role, and this scenario has not been ruled out by our nulling observations.

Future observations should take advantage of the increased sensitivity and longer baselines of telescopes optimized for observations in the mid-IR. Current contrast ratios of about 100 allow us to achieve dust detection levels 2 to 4 orders of magnitude better than photometric detections at longer wavelengths (with an assumed 5% calibration) for a hypothetical A-type star at 10 pc (Figure 4.4). Ideally, in future ground-based nulling implementations with AO, we hope to achieve contrast levels of 1000, resulting in another order of magnitude improve-

ment in dust detection levels. Experiments at the MMT with an internal phase control loop in the BLINC instrument have a potential to achieve such an improvement. Further down the line, the *Large Binocular Telescope*'s large aperture, long baseline, and thermal IR optimized adaptive optics setup (i.e., deformable secondaries) will prove to be a very useful tool in observing debris disks, pushing levels of detectable dust down to a few zody around nearby stars, or fractional dust luminosities of $\sim 10^{-7}$.

An immediate scientific impact can be made by observing other stars with excesses detected at other wavelengths that are not currently accessible due to small fluxes or larger distances that cannot be spatially resolved with current instrumentation. The scientific value of such observations have been demonstrated in this study. Many stars with excess as detected by Rieke et al. (2005) will be observable in the future. In addition, re-observation of targets in this sample may provide better limits or actual positive detections of dust at levels lower than are possible with the current observational setup. In this way we may assess, for example, the efficiency of different removal mechanisms. Do systems which are cleared by planetary sweepers have less or more debris than systems where collisional removal is thought to be the dominant mechanism? As the detection of planets continue, we may observe the debris in these systems to further constrain the effect of planetary perturbers on debris and solid material in the system. In this way we may be able to predict the survivability of terrestrial planets around nearby stars and find systems which are promising targets for future space missions such as the *Terrestrial Planet Finder*.

4.3.3 General Thoughts, Conclusions, and Implications

In observations of circumstellar dust, either in primordial disks surrounding pre-main sequence stars, or second-generation debris around mature stars, the ne-

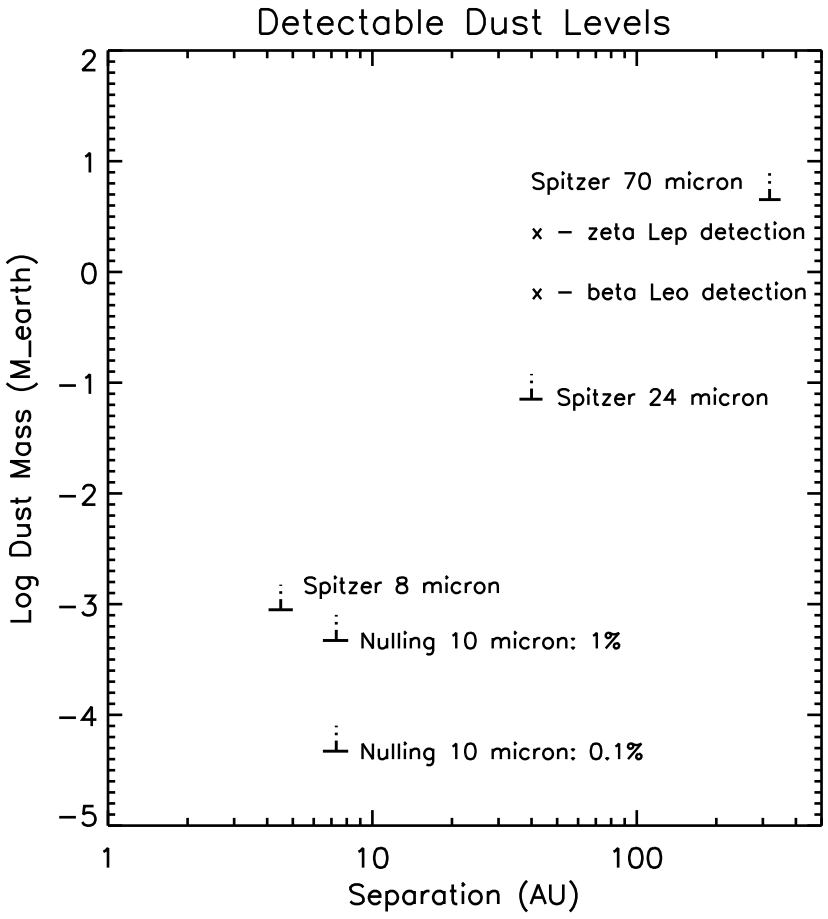

Figure 4.4 This figure shows the limits for levels of detectable dust (in Earth masses) for a range of separations around a hypothetical A-type main-sequence star at 10 pc. Shown are the limits for photometric detections in three Spitzer bands (assuming 5% calibration), as well as nulling interferometric limits for contrast ratios of 100 and 1000. The positive detections for ζ Lep and β Leo by Spitzer are indicated by X's

cessity for multi-wavelength coverage cannot be overstated. While the evolution of warm primordial dust in the inner few AU of a disk, or the presence of planetary debris in the habitable zone surrounding main sequence stars have their own intriguing implications, the true power of the observations presented here lies in their complementary nature to previous studies of individual objects at different wavelengths and/or using different techniques. For example, *Spitzer* observations are unparalleled in photometric sensitivity, but lack the spatial resolution to directly probe the physical distribution of dust in the inner system. We have shown the complementary nature of these datasets in the analysis of the Vega results. For the entire main sequence sample, we have ruled out debris belts in the inner system more massive than 100 to 1000 times our own solar system's Main Belt. Similarly, we have combined our nulling results with previous results from observations of Herbig Ae stars, including SED studies as well as direct imaging at longer wavelengths. From these complementary data we have shown that there are certain characteristics (e.g., sub-mm SED slope and fractional IR luminosity) which are good predictors for the size of 10 μm emission region. We have also examined each particular spatially resolved system and find that, when viewed in context of previous studies and imaging data, these systems actually appear quite different. This also shows that although our tendency is to group these objects together based upon their gross physical characteristics (e.g., amount of infrared excess), further examination may prove to highlight more differences than similarities. In this way we are continuing to build a picture of the disk in each system.

Pre-main sequence objects of intermediate mass do have large amounts of circumstellar dust, and the distribution of the material is found to be consistent with a disk, for those objects which are spatially resolved. One example of disk

clearing may have been observed, occurring in an inside-out fashion in the HD 100546 system. The influence of a giant protoplanet is suspected, and the age of the system is consistent with when the formation of these planets is thought to occur. As intermediate-mass stars evolve onto the main sequence the results of this study support the view that they lose the vast majority of their circumstellar dust in the inner system. This is consistent with current dust models, such as those computed by Kenyon and collaborators, as well as previous observations of low mass main sequence stars of younger age. This is also evidence that most low or intermediate-mass systems lose their inner dust on shorter timescales compared to larger separations. We find this to be the case for intermediate-mass stars, where even those with large amounts of far-IR excesses are often relatively devoid of material in the inner system. This points to various dust clearing mechanisms in these systems, and we have discussed possibilities ranging from collisional removal and P-R drag to giant planets. With a new generation of telescopes and instrumentation soon becoming available, the community should be able to form an even more complete picture of star and planet formation.

Improvements in nulling interferometric observations will have their own contributions to make in the future. They will provide the contrast levels and precision in calibration necessary to observe smaller and more distant disks (with sizes down to a few AU and distances out to several hundred parsecs), as well as late-type objects which are analogous to our sun.

APPENDIX A

NULLING DATA REDUCTION PIPELINE

This section summarizes the data reduction steps for deriving source nulls from raw data. Figure A.1 is a diagram which illustrates the primary steps. The raw data is first converted from MIRAC format to FITS format. The data are then organized into 'sets' depending on whether the data were taken with or without AO. As described in Chapter 2, non-AO data are taken in large sets of fast frames in order to adequately sample the randomly varying phase. Observations taken with AO are taken with a path difference tuned into one of the interferometer beams to achieve destructive interference or a full flux image. Photometry is then extracted for each frame. Due to small variations in the phase even in AO observations, each set of 10 destructive frames is examined for the frame with the best suppression of flux. This is still significantly more efficient than the non-AO case where only 1 out of 500 frames are used. For the AO observations, we use all ten full flux images in each set, median combining those images. For the non-AO case, observations are again relatively inefficient, with 1 out of 500 frames being used, as in the destructively interfered case. The procedure is repeated for the point source calibrators and science objects to determine the instrumental nulls. These nulls are differenced to determine the souce null (see Chap. 2).

The code that follows was written to perform photometry on a set of nulling data, choose the best destructive and full flux images, and calculate the instrumental null. It is written in IDL.

```
pro  null_analyze

;*****************************
; NAME:    NULL_ANALYZE
```

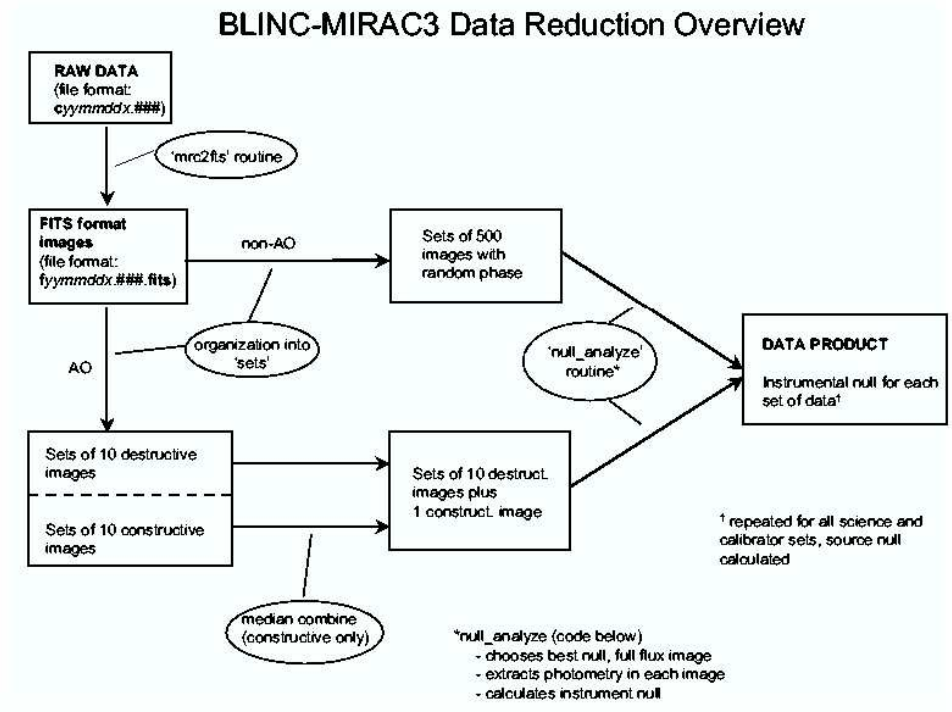

Figure A.1 Data reduction steps. Boxes contain intermediate data products, ellipses contain processes used.

```
;          written   by W. Liu,  Steward   Observatory,    10/02
;
; PURPOSE:    Reads  in a list  of BLINC  image  filenames   and finds  the frame
;             with  the  best  null  and  the  image  with  the  best  constructive
;             frame  of a user  defined  source.    Calculates   the  percent   null
;             of  the  best  nulled  image.
;
; OUTPUTS:    BEST_NULL   - The  frame  with  the  best  null
;             BEST_FULL   - The  frame  with  the  best  constructive    image
;             NULL_PERCENT    - The  percent   null  in  the  best  nulled  image
; PROCEDURES   USED:  APER
;*****************************

imagelist   = ''
read,imagelist,prompt='Please        enter  the  list  of  .fits  files:  '
readcol,imagelist,f='a',images                  ; reads  in the  image  list  file
n_im  = n_elements(images)
flux  = dindgen(n_im)
fluxerr   = dindgen(n_im)
skyval  = dindgen(n_im)
skyerr  = dindgen(n_im)

best_nullflux    = 0.0
best_fullflux    = 0.0

;input  aperture   photometry   parameters

read,xc,yc,prompt='Please       enter  the  x and  y coordinates,    separated   by a space:'
read,apsize,prompt='Please       enter  the  aperture   size  in pix:  '
read,skyin,prompt='Please       enter  the  inner  radius  for  the  sky  annulus:   '
read,skyout,prompt='Please       enter  the  outer  radius  for  the  sky  annulus:   '
phadu=1.
badpix=[-32765.,32767.]
skyarr=[skyin,skyout]

best_null   = 0
best_full   = 0

for  i=0,n_im-1   do  begin
  fits_read,images(i),image1,header1
```

```
  aper,image1,xc,yc,flux1,fluxerr1,skyval1,s          kyerr1,  phadu,  apsize,  skyarr,  badpix  ,$
/FLUX;,/SILENT
  flux(i)=flux1
  fluxerr(i)=fluxerr1
  skyval(i)=skyval1
  skyerr(i)=skyerr1
  if  (i  eq  0)  then  begin          ;First   image:   initialize    values
    best_nullflux    = flux(i)
    best_fullflux    = flux(i)
    best_null   = i
    best_full   = i
  endif
  if  (flux(i)   lt  best_nullflux)    then  begin    ;Tests   for  better   null  than  before
      best_nullflux    = flux(i)
      best_null   = i
  endif
  if  (flux(i)   gt  best_fullflux)    then  begin    ;Tests   for  better   constuctive
     ;  image   than  before
      best_fullflux    = flux(i)
      best_full   = i
  endif
endfor

null_percent    = (best_nullflux/best_fullflux)*100            ;Calculates    null  percent

print,'The    best  null  is  in  the  image  ',images(best_null)
print,'The    best  constuctive    image  is  in  ',images(best_full)
print,'The    best  nulled  flux  percentage    is  ',null_percent,'     \%'

end
```

APPENDIX B

INTERPRETING THE HERBIG AE DATA: MODELS USED IN THE INTERPRETATION OF OBSERVATIONS

Once source nulls are calculated for each object, we use the following codes to infer physical parameters for any resolved disk. In both cases, the output of the code is a theoretical value for the null achieved on the object, given various physical parameters for a theoretical disk. The first code below is used to assess the physical size of a resolved disk using two simple intensity distributions. The first model is a disk where the intensity has a Gaussian dependence vs. distance from the center of the disk, with the free parameter being the FWHM of the Gaussian function. The second model is a uniform intensity ring model with the variables being the separation of the ring from the center of the system, as well as its width. Both these intensity models are then convolved with the transmission function of the interferometer to determine the source null, which are then matched to the observations.

```
;******************************
; NAME:   HERBIG_GAUSSIAN
;          written  by W. Liu,  Steward  Observatory,   10/05
;
; PURPOSE:    Given  stellar  parameters,   grain  properties,   and disk
;             size,  calculates   the theoretical   null  on extended   emission
;      for two simple  models:  a gaussian  intensity  disk,  and a
;             ring
;
; OUTPUTS:    NULL  - The theoretical   null  from  a gaussian  intensity   disk
;             RING_NULL   - Same  as NULL  for a ring  of emission
;******************************
;;;;;;;;;;;;;;;;;;;;;;;;;;;;;;;;;;;;;;;;;;;;           ;;;;;;;  ;;;;;;  ;
;;;;;;;;;;;;;;;;;;;;FUNCTIONS;;;;;;;;;;;;;;           ;;;;;;;  ;;;;;;  ;
;;;;;;;;;;;;;;;;;;;;;;;;;;;;;;;;;;;;;;;;;;;;           ;;;;;;;  ;;;;;;  ;
```

```
;;;;;;;;distance      from   center   calculator

function    rcen,   x,y,   xcen=xcen,    ycen=ycen,    ii=ii,   rota=rota

return,   sqrt(   (  (x-xcen)*cos(rota)      - (y-ycen)*sin(rota)      )^2.  $
                + (  ((y-ycen)*cos(rota)      + (x-xcen)*sin(rota))      )^2.  / ii^2.   )
end

;;;;;;;;;;;;Intensity       calculation    functions

;;;Surface    intensity    (Gaussian);;;;;;;;

function    Itot,   x,y,   xcen=xcen,    ycen=ycen,    ii=ii,   rota=rota,    inner=inner,     $
outer=outer,     Ts=Ts,   Tc=Tc,   AU=AU,   Rs=Rs,   lamb=lamb,    beta=beta,    rg=rg,   pi=pi,$
h1=h1,   nu=nu,   c=c,   kk=kk,   half_width=half_width

return,   (1 / (half_width*(2.*pi)^0.5))        * (exp(-0.5    * (rcen(x,y,    xcen=xcen,    $
ycen=ycen,    ii=ii,   rota=rota)/half_width)^2.))

end

;;;Intensity    (Ring);;;;;;

function    Itot_ring,    x,y,   xcen=xcen,    ycen=ycen,    ii=ii,   rota=rota,    inner=inner,     $
outer=outer,     Ts=Ts,   Tc=Tc,   AU=AU,   Rs=Rs,   lamb=lamb,    beta=beta,    rg=rg,   pi=pi,   $
h1=h1,   nu=nu,   c=c,   kk=kk,   ring_radius=ring_radius,        ring_width=ring_width

ring_inner    = ring_radius    - (ring_width/2.)
ring_outer    = ring_radius    + (ring_width/2.)

if  (rcen(x,y,    xcen=xcen,    ycen=ycen,    ii=ii,   rota=rota)    ge  ring_inner)    AND  $
  (rcen(x,y,    xcen=xcen,    ycen=ycen,    ii=ii,   rota=rota)    le  ring_outer)    then  $
return,1.    else   return,0.

end

;;;;;;;;;;;;;;;;;Transmission          Functions

; Transmission    function   of  interferometer:
```

```
function  Tr,x,  pi=pi,  base=base,  lamb=lamb,  AU=AU,  ds=ds
return,(sin(  pi*(base/lamb)*(x*AU/ds)  ))^2.
end

function  Tr2,x,  pi=pi,  base=base,  lamb=lamb,  AU=AU,  ds=ds
return,(cos(  pi*(base/lamb)*(x*AU/ds)  ))^2.
end


pro  herbig_gaussian


;;;;;;;;;;;;;;;CONSTANTS  AND  NON-VARIABLE  PARAMETERS;;;;;;;;;;;;;;;;;;;

;;  common  constants,  c,  k,  G,  h,  pc,  AU,  Msun,  Rsun,  $
;;  mu,  deg,  pi

;Constants  (all  cgs)
c=2.997925d10
kk=1.380658d-16
G=6.67259d-8
h1=6.6260755d-27
pc=3.08567758d18
AU=1.496d13
mu  =  1.75/6.02d23
deg  =  0.0174533
pi  =  3.14159265

;;  common  stellar,  Ts,  Rs,  Ms,  Tc,  ds

;Stellar  Parameters:
ds  =  244.  *  pc

;;  common  pars,  lamb,  nu,  base,  rg,  beta,  kappag,  incl,  rota,  $
;;  i,  inner,  outer,  omega,  xmax,  ymax,  xcen,  ycen

;Wavelength
lamb  =  10.6d-4  ;cm
nu  =  c/10.6d-4
```

```
;nulling   baseline
base  = 400.  ;cm

;Grain  properties
rg  = 1.d-5  ;cm
beta=1.
kappag=400.    ; opacity:   cm^2  g^-1

;Gaussian   Disk  parameters
incl  = 45.  * deg
rota  = 0.  * deg
ii  = cos(incl)
half_width    = 10.

;Ring  parameters
ring_radius=    13.5
ring_width=2.

inner=1.               ;inner   edge  in  AU
outer=500.             ;outer   edge  in  AU

omega  = AU^2./ds^2.

xmax  = 200
ymax  = 200
xcen  = xmax/2
ycen  = ymax/2


;Calculate   intensity   on an AU map:

rxy  = dindgen(xmax,ymax)                                ;initialize    arrays
Itot_null    = dindgen(xmax,ymax)
Itot_full    = dindgen(xmax,ymax)
Itot_null_ring     = dindgen(xmax,ymax)
Itot_full_ring     = dindgen(xmax,ymax)
trdust   = dindgen(xmax,ymax)
null_flux=0.0
full_flux=0.0
```

```
null_flux_ring=0.0
full_flux_ring=0.0
tr2dust=dindgen(xmax,ymax)

for  x=0,xmax-1    do  begin                                ;for  each  grid  element
  for  y=0,ymax-1    do  begin
      ;calculate    distance    from  center:
      rxy[x,y]    = rcen(x,y,    xcen=xcen,    ycen=ycen,    ii=ii,   rota=rota)

      Itot_null[x,y]     = Itot(x,y,    xcen=xcen,    ycen=ycen,    ii=ii,   rota=rota,    $
                                inner=inner,     outer=outer,     Ts=Ts,   Tc=Tc,   AU=AU,   $
                                Rs=Rs,   lamb=lamb,    beta=beta,    rg=rg,   pi=pi,   h1=h1  $
      nu=nu,   c=c,   kk=kk,   half_width=half_width)       * $
       Tr(x-xcen,    pi=pi,   base=base,    lamb=lamb,    AU=AU,   ds=ds)   * $
                          omega

      Itot_full[x,y]     = Itot(x,y,    xcen=xcen,    ycen=ycen,    ii=ii,   rota=rota,    $
                                inner=inner,     outer=outer,     Ts=Ts,   Tc=Tc,   AU=AU,   $
                                Rs=Rs,   lamb=lamb,    beta=beta,    rg=rg,   pi=pi,   h1=h1,   $
      nu=nu,   c=c,   kk=kk,   half_width=half_width)       * $
       Tr2(x-xcen,    pi=pi,   base=base,    lamb=lamb,    AU=AU,   $
          ds=ds)   * $
       omega


      Itot_null_ring[x,y]      = Itot_ring(x,y,     xcen=xcen,    ycen=ycen,    ii=ii,   $
rota=rota,    inner=inner,     outer=outer,     Ts=Ts,   $
Tc=Tc,   AU=AU,   Rs=Rs,   lamb=lamb,    beta=beta,    $
rg=rg,   pi=pi,   h1=h1,   nu=nu,   c=c,   kk=kk,   $
ring_radius=ring_radius,        ring_width=ring_width)       $
     *omega   * $
     Tr(x-xcen,    pi=pi,   base=base,    lamb=lamb,    AU=AU,   ds=ds)

      Itot_full_ring[x,y]      = Itot_ring(x,y,     xcen=xcen,    ycen=ycen,    ii=ii,   $
rota=rota,    inner=inner,     outer=outer,     Ts=Ts,   $
Tc=Tc,   AU=AU,   Rs=Rs,   lamb=lamb,    beta=beta,    $
rg=rg,   pi=pi,   h1=h1,   nu=nu,   c=c,   kk=kk,   $
ring_radius=ring_radius,        ring_width=ring_width)       $
    * Tr2(x-xcen,    pi=pi,   base=base,    lamb=lamb,    AU=AU,   $
ds=ds)   * $
```

```
    omega


      null_flux    = null_flux    + Itot_null[x,y]
      full_flux    = full_flux    + Itot_full[x,y]

      null_flux_ring     = null_flux_ring     + Itot_null_ring[x,y]
      full_flux_ring     = full_flux_ring     + Itot_full_ring[x,y]

    endfor
endfor
surface,Itot_null

null  = null_flux/full_flux
ring_null    = null_flux_ring/full_flux_ring
print,   'Gaussian    null:   ',null
print,   'Ring   null:   ',ring_null

end
```

The following code was used to determine the effect of disk flaring on the source null of an object. The model closely follows the flared disk model of Chiang & Goldreich (1997), with the only difference being the variable - the exponent in the scale height vs. separation function (this is found in the function 'alpha'). The physical parameters are used to calculate the intensity distribution of a hypothetical disk, which is then convolved with the transmission function of the interferometer to calculate the theoretical source null.

```
;*****************************
; NAME:    HERBIG_DISKMODEL4
;          v.4  written   by  W.  Liu,   Steward   Observatory,     10/05
;
; PURPOSE:     Given   stellar   parameters,     grain   properties,     and  flaring
;              exponent    (see   'a',   CG97,   eq.10),    calculates    the  theoretical    null
;              achieved    on  a hypoyhetical     Chiang   and  Goldriech    (1997)
;              flared   disk
```

```
;
; OUTPUTS:   NULL - The theoretical  null from a CG97 disk
;********************************
;;;;;;;;;;;;;;;;;;;;;;;;;;;;;;;;;;;;;;;;;;;;;       ;;;;;;; ;;;;;; ;
;;;;;;;;;;;;;;;;;;;;FUNCTIONS;;;;;;;;;;;;;;;       ;;;;;;; ;;;;;; ;
;;;;;;;;;;;;;;;;;;;;;;;;;;;;;;;;;;;;;;;;;;;;;       ;;;;;;; ;;;;;; ;

;;;;;;;;distance   from center calculator

function  rcen, x,y, xcen=xcen,  ycen=ycen,  ii=ii, rota=rota

return, sqrt( ( (x-xcen)*cos(rota)   - (y-ycen)*sin(rota)   )^2. $
              + ( ((y-ycen)*cos(rota)   + (x-xcen)*sin(rota))   )^2. / ii^2. )
end



;;;;;;;;alpha  and optical  depth functions

function  alpha, r, Ts=Ts, Tc=Tc, AU=AU, Rs=Rs

flare=10./35.      ; The flaring  parameter
mass=3.4
return,  0.4*(Rs/(r*AU))   + $
( (4.*flare)  * ((Ts/Tc)^(4./7.))   * ((r*AU/Rs)^(flare))   )
end

function  tau, r, Ts=Ts, Tc=Tc, AU=AU, Rs=Rs, lamb=lamb,  beta=beta,  rg=rg, pi=pi
return, alpha(r, Ts=Ts, Tc=Tc, AU=AU, Rs=Rs) * (2.*pi*rg/lamb)^beta
end

;;;;;;;;;;disk   temperature  functions

;Disk surface Temperature:

function  Tsurf, r, Ts=Ts, Rs=Rs, AU=AU, beta=beta
return, (Ts/0.9269)  * (Rs/(2.*r*AU))^(1./(2.+(beta/2.)))
end

;Disk internal Temperature:
```

```
function Tint, r, Ts=Ts, Rs=Rs, AU=AU, beta=beta

return, Tsurf(1, Ts=Ts, Rs=Rs, AU=AU, beta=beta)*(150./550.)       * (r)^(-3./7.)
end

;;;;;;;;;;;Planck      function

function B, T, h=h, nu=nu, c=c, kk=kk

return, 2.*h*(nu^3./c^2.)      * ( 1. / (exp((h*nu)/(kk*T))      - 1.) )
end


;;;;;;;;;;;;Intensity       calculation     functions

;Surface   intensity:

function Isurf, x,y, xcen=xcen, ycen=ycen, ii=ii, rota=rota, inner=inner,     $
outer=outer,     Ts=Ts, Tc=Tc, AU=AU, Rs=Rs, lamb=lamb, beta=beta,     $
rg=rg, pi=pi, h=h, nu=nu, c=c, kk=kk

dist  = rcen(x,y,    xcen=xcen,    ycen=ycen,    ii=ii,   rota=rota)

values  = dist  * 0

okay  = where(dist    ge  inner  AND  dist  le  outer,   nokay)

if  nokay  ne  0L  then  values[okay]    = ( 1.-exp(-1.*tau(dist[okay],        $
  Ts=Ts,   Tc=Tc,   AU=AU,   Rs=Rs,   lamb=lamb,    beta=beta,    rg=rg,   pi=pi))   ) * $
  B(Tsurf(rcen(x,y,      xcen=xcen,    ycen=ycen,    ii=ii,   rota=rota),    Ts=Ts,   Rs=Rs,   $
AU=AU,   beta=beta),    h=h,   nu=nu,   c=c,   kk=kk)   * 10.^19.

return,   values

end

;Internal   intensity:

function Iint, x,y, xcen=xcen,    ycen=ycen,    ii=ii,   rota=rota,    inner=inner,     $
outer=outer,     Ts=Ts,   Tc=Tc,   AU=AU,   Rs=Rs,   beta=beta,    h=h,  $
```

```
nu=nu,  c=c,  kk=kk

    dist  = rcen(x,y,   xcen=xcen,   ycen=ycen,   ii=ii,  rota=rota)

    values  = dist  * 0

    okay  = where(dist   ge  inner  AND  dist  le  outer,  nokay)

    if  nokay  ne  0L  then  values[okay]    = $
      B(Tint(dist[okay],      Ts=Ts,   Rs=Rs,   AU=AU,   beta=beta),    h=h,   nu=nu,   c=c,  $
kk=kk)  * 10.^19.

    return,   values

 end

;Total  intensity:

function   Itot,  x,y,  xcen=xcen,   ycen=ycen,   ii=ii,   rota=rota,    inner=inner,    $
outer=outer,    Ts=Ts,   Tc=Tc,   AU=AU,   Rs=Rs,   lamb=lamb,    beta=beta,    $
rg=rg,   pi=pi,   h=h,   nu=nu,   c=c,   kk=kk

return,   Isurf(x,y,   xcen=xcen,   ycen=ycen,   ii=ii,   rota=rota,   inner=inner,    $
outer=outer,    Ts=Ts,   Tc=Tc,   AU=AU,   Rs=Rs,   lamb=lamb,    beta=beta,    $
rg=rg,   pi=pi,   h=h,   nu=nu,   c=c,   kk=kk)  + $
         Iint(x,y,   xcen=xcen,   ycen=ycen,   ii=ii,   rota=rota,   inner=inner,    $
outer=outer,    Ts=Ts,   Tc=Tc,   AU=AU,   Rs=Rs,   beta=beta,    h=h,  $
nu=nu,   c=c,   kk=kk)
end

;;;;;;;;;;;;;;;;;;Transmission         Functions

; Transmission    function   of  interferometer:

function   Tr,x,   pi=pi,   base=base,   lamb=lamb,   AU=AU,   ds=ds
return,(sin(    pi*(base/lamb)*(x*AU/ds)       ))^2.
end

function   Tr2,x,   pi=pi,   base=base,   lamb=lamb,   AU=AU,   ds=ds
return,(cos(    pi*(base/lamb)*(x*AU/ds)       ))^2.
```

```
end



;;;;;;;;;;;;;;;;;;;;;;;;;;;;;;;;;;;;;;;;;;;           ;;;;;;;  ;;;;;;  ;;;;;;;  ;;;;;;;  ;;;;;;  ;
;;;;;;;;;;;;;;;;;;;;;;;;;;;;;;;;;;;;;;;;;;;           ;;;;;;;  ;;;;;;  ;;;;;;;  ;;;;;;;  ;;;;;;  ;

pro  herbig_diskmodel4

;;;;;;;;;;;;;;;CONSTANTS       AND  NON-VARIABLE    PARAMETERS;;;;;;;;;;;;;;;;;;

;;  common   constants,    c,  k,  G,  h,  pc,  AU,  Msun,   Rsun,   $
;;      mu,  deg,   pi

;Constants    (all  cgs)
c=2.997925d10
kk=1.380658d-16
G=6.67259d-8
h=6.6260755d-27
pc=3.08567758d18
AU=1.496d13
Msun=1.99d33
Rsun=6.96d10
mu  = 1.75/6.02d23
deg  = 0.0174533
pi  = 3.14159265

;;  common   stellar,   Ts,  Rs,  Ms,  Tc,  ds

;Stellar   Parameters:
Ts  = 9750.   ;Kelvin
Rs  = 2.5  * Rsun
Ms  = 3.4  * Msun
Tc  = (G*Ms*mu)/(kk*Rs)
ds  = 144.  * pc

;;  common   pars,   lamb,   nu,  base,   rg,  beta,   kappag,   incl,   rota,   $
;;                i,  inner,   outer,   omega,   xmax,   ymax,   xcen,   ycen

;Wavelength
lamb  = 10.3d-4   ;cm
```

```
nu = c/10.3d-4

;nulling  baseline
base = 400.  ;cm

;Grain  properties
rg = 1.d-5  ;cm
beta=1.
kappag=400.   ; opacity:  cm^2 g^-1

;Disk  inclination/rotation
incl = 0. * deg
rota = 0. * deg
ii = cos(incl)

inner=1.            ;inner  edge  in AU
outer=500.          ;outer  edge  in AU

omega  = AU^2./ds^2.

xmax = 1000
ymax = 1000
xcen = xmax/2
ycen = ymax/2

;;;;;;;;;;;;;;;;;;;;;;;;;;;;;;;;;;;;;;;;;;;;          ;;;;;;; ;;;;;; ;;;;;;; ;;;;;;; ;
;;;;;;;;;;;;;;;;;;;;;NULLING       OUTPUT;;;;;;;;;;;;;;;;;;;;;;;;;;;;;;;;;;;;          ;
;;;;;;;;;;;;;;;;;;;;;;;;;;;;;;;;;;;;;;;;;;;;          ;;;;;;; ;;;;;; ;;;;;;; ;;;;;;; ;

;Calculate  intensity  on an AU map:

rxy = dindgen(xmax,ymax)     ;initialize   arrays
Itot1  = dindgen(xmax,ymax)
trdust  = dindgen(xmax,ymax)
logtrdust=dindgen(xmax,ymax)

null_flux=0.0
full_flux=0.0
tr2dust=dindgen(xmax,ymax)
```

```
for  x=0,xmax-1    do  begin   ;for   each   grid   element
  for   y=0,ymax-1    do  begin
      ;calculate    distance    from   center:
      rxy[x,y]    =  rcen(x,y,    xcen=xcen,    ycen=ycen,    ii=ii,   rota=rota)

      Itot1[x,y]    =  Itot(x,y,    xcen=xcen,    ycen=ycen,    ii=ii,   rota=rota,    $
                                    inner=inner,     outer=outer,     Ts=Ts,   Tc=Tc,   AU=AU,   $
                                    Rs=Rs,   lamb=lamb,    beta=beta,    rg=rg,   pi=pi,   h=h,   $
                                    nu=nu,   c=c,   kk=kk)   ;calculate    intensity

  trdust[x,y]    =  Itot1[x,y]    *  omega   *  $
    Tr(x-xcen,    pi=pi,   base=base,    lamb=lamb,    AU=AU,   ds=ds)   ;transmitted    flux
  tr2dust[x,y]    =  Itot1[x,y]    *  omega   *  $
    Tr2(x-xcen,    pi=pi,   base=base,    lamb=lamb,    AU=AU,   ds=ds)

  if  (trdust[x,y]    eq  0.0)  then  $                              ;log  transmitted    flux
  logtrdust[x,y]=0.0      else  $
  logtrdust[x,y]=alog10(trdust[x,y])

  null_flux    =  null_flux    +  trdust[x,y]                       ;sum  up  nulled   flux
  full_flux    =  full_flux    +  tr2dust[x,y]                       ;sum  up  constr.   flux

  endfor
endfor

print,"Null=",null_flux/full_flux

end
```

APPENDIX C

INTERPRETING THE MAIN-SEQUENCE DATA: THE KELSALL ZODIACAL DUST MODEL IN IDL

The code below is used to physically interpret the source null (or limit) observed for a main sequence object. The model below is based upon the model presented in Kelsall et al. (1998) for the solar zodiacal cloud. The code models only the ″smooth″ cloud component which is the primary component of the Kelsall model. The variable is the cloud density, found in the ′tau′ function. The density is scaled in factors of solar zodiacal cloud level, or ″Zody.″ The model uses this dust density to predict the intensity in a hypothetical debris disk, which is then convolved with the transmission function of the interferometer. Theoretical fluxes are calculated for the destructively and full flux observations, and the stellar flux, which dominates the unresolved flux is added to the full flux image. A source null is then calculated, and matched to the observations to determine a dust density or limit.

```
;******************************
; NAME:    KELSALL
;           written   by  W.  Liu,  Steward   Observatory,    4/07
;
; PURPOSE:     Given  stellar   parameters   and  density   of  debris,
;              calculates    the  theoretical    null  on  emission   from  debris
;       using   a  model   based   upon  Kelsall   et  al.  (1998)
;
; OUTPUTS:     NULL  - The  theoretical    null  from  a  gaussian   intensity   disk
;******************************
;;;;;;;;;;;;;;;;;;;;;;;;;;;;;;;;;;;;;;;;;;;;             ;;;;;;;  ;;;;;;  ;
;;;;;;;;;;;;;;;;;;;;FUNCTIONS;;;;;;;;;;;;;;;             ;;;;;;;  ;;;;;;  ;
;;;;;;;;;;;;;;;;;;;;;;;;;;;;;;;;;;;;;;;;;;;;             ;;;;;;;  ;;;;;;  ;

;;;;;;;;;;;;;distance       from  center   calculator
```

```
function rcen, x,y, xcen=xcen, ycen=ycen, incrmnt=incrmnt, ii=ii, rota=rota
xcen_au=xcen*incrmnt
ycen_au=ycen*incrmnt
x_au= x * incrmnt
y_au= y * incrmnt
return, sqrt( ( (x_au-xcen_au)*cos(rota) - (y_au-ycen_au)*sin(rota) )^2. $
        + ( ((y_au-ycen_au)*cos(rota) + (x_au-xcen_au)*sin(rota)) )^2.)
end

;;;;;;;;;;;;;;;;;Temperature function
function Temp, x,y, xcen=xcen, ycen=ycen, Ts=Ts, Rstar=Rstar, Rsun=Rsun,$
         Temp_1=Temp_1, incrmnt=incrmnt, rota=rota

return, Temp_1 * rcen(x,y, xcen=xcen, ycen=ycen, incrmnt=incrmnt, ii=ii, $
rota=rota)^(-0.467)

end


;;;;;;;;;;;;;;;;;;Function 'gee'
function gee, x,y,z, xcen=xcen, ycen=ycen, ii=ii, rota=rota, mu=mu, $
incrmnt=incrmnt

if (z/rcen(x,y, xcen=xcen, ycen=ycen, incrmnt=incrmnt,ii=ii, rota=rota) lt mu)$
 then return, (z/rcen(x,y, xcen=xcen, ycen=ycen, incrmnt=incrmnt,ii=ii, $
rota=rota))^2. * (1./(2. * mu)) $
else return, (z/rcen(x,y, xcen=xcen, ycen=ycen, incrmnt=incrmnt,ii=ii, $
rota=rota)) - (mu/2.)

end

;;;;;;;;;;;;;;;;;Density (opt. depth)
function tau, x,y,z, xcen=xcen, ycen=ycen, ii=ii, rota=rota, incrmnt=incrmnt,$
mu=mu

;change 1st number below to change density in units of zodi

return, 390. * 1.3d-7 * rcen(x,y, xcen=xcen, ycen=ycen, incrmnt=incrmnt,ii=ii,$
rota=rota)^(-1.34) * exp(-4.14 * gee(x,y,z, xcen=xcen, ycen=ycen, ii=ii, $
```

```
rota=rota,    mu=mu,   incrmnt=incrmnt)^0.942)

end

;;;;;;;;;;;;;;;;;Planck       function

function   B, x,y,  xcen=xcen,    ycen=ycen,    h=h,   nu=nu,   c=c,   kk=kk,   incrmnt=incrmnt,$
rota=rota,    Temp_1=Temp_1
return,   2.*h*(nu^3./c^2.)      * ( 1.  / (exp((h*nu)/(kk*Temp(x,y,xcen=xcen,           $
ycen=ycen,    Ts=Ts,   Rstar=Rstar,    Rsun=Rsun,    Temp_1=Temp_1,     incrmnt=incrmnt,$
rota=rota)))    - 1.)  )
end

;;;;;;;;;;;;;;;;;Intensity        funtion
function   Is,  x,y,z,   xcen=xcen,    ycen=ycen,    ii=ii,   rota=rota,    Ts=Ts,   Rstar=Rstar,$
               Rsun=Rsun,    Temp_1=Temp_1,     h=h,   nu=nu,   c=c,   kk=kk,   inner=inner,$
               outer=outer,     incrmnt=incrmnt,      mu=mu

if  (rcen(x,y,    xcen=xcen,    ycen=ycen,    incrmnt=incrmnt,ii=ii,       rota=rota)    ge  inner)   $
AND  (rcen(x,y,    xcen=xcen,    ycen=ycen,    incrmnt=incrmnt,ii=ii,       rota=rota)    le  outer)$
then  return,   tau(x,y,z,    xcen=xcen,    ycen=ycen,    ii=ii,   rota=rota,    incrmnt=incrmnt,$
mu=mu)   * $
B(x,y,   xcen=xcen,    ycen=ycen,    h=h,   nu=nu,   c=c,   kk=kk,   incrmnt=incrmnt,      rota=rota,$
Temp_1=Temp_1)$
else  return,0.

end

;;;;;;;;;;;;;;;;;Transmission         Functions

; Transmission    function   of  interferometer:

function   Tr,x,   xcen=xcen,    pi=pi,   base=base,    lamb=lamb,    AU=AU,   ds=ds,   incrmnt=incrmnt
x_au=(x-xcen)*incrmnt
return,(sin(     pi*(base/lamb)*(x_au*AU/ds)         )^2.
end

function   Tr2,x,   xcen=xcen,    pi=pi,   base=base,    lamb=lamb,    AU=AU,   ds=ds,   incrmnt=incrmnt
x_au=(x-xcen)*incrmnt
return,(cos(     pi*(base/lamb)*(x_au*AU/ds)         )^2.
```

```
end



;;;;;;;;;;;;;;;;;;;;;;;;;;;;;;;;;;;;;;;;;           ;;;;;;;  ;;;;;;  ;;;;;;;  ;;;;;;;  ;;;;;;  ;
;;;;;;;;;;;;;;;;;;;;;;;;;;;;;;;;;;;;;;;;;           ;;;;;;;  ;;;;;;  ;;;;;;;  ;;;;;;;  ;;;;;;  ;

pro  kelsall

;;;;;;;;;;;;;;CONSTANTS       AND  NON-VARIABLE    PARAMETERS;;;;;;;;;;;;;;;;;;

;Constants    (all  mks)
c=2.997925d8
kk=1.380658d-23
G=6.67259d-11
h=6.6260755d-34
pc=3.08567758d16
AU=1.496d11
Msun=1.99d30
Rsun=6.96d8
mu  = 0.189
deg  = 0.0174533
pi  = 3.14159265
A  = 0.2761

;Stellar   Parameters:
Ts  = 9250  ;Kelvin
Rstar  = 2.4  * Rsun
Mstar  = 2.9  * Msun
ds  = 7.8  * pc
flux_12   = 41.56  ;Jy  - 12  micron   flux  of  the  parent   star

;Wavelength
lamb  = 10.6d-6   ;m
nu  = c/lamb

;nulling   baseline
base  = 4.  ;m

;disk  parameters
Temp_1  = (Rstar/AU)^0.5    * Ts  * (1.-A)           ;central   temp
```

```
omega  = AU^2./ds^2.

inner=  0.02875  * (Temp_1/286.)^(1./0.467)          ;inner  edge  in  AU
outer=  10.                                          ;outer  edge  in  AU
height=  2.       ;height  in  AU

xmax  = 150
ymax  = 150
xcen  = xmax/2
ycen  = ymax/2
incrmnt  = 0.1  ;physical  size  (in  AU)  of  each  grid  element
rota  = 0.
ii=  0.

;;;;;;;;;;;;;;;;;;;;;;;;;;;;;;;;;;;;;;;;;;;;;;;;          ;;;;;;;  ;;;;;;  ;;;;;;;  ;;;;;;;  ;
;;;;;;;;;;;;;;;;;;;;;NULLING        OUTPUT;;;;;;;;;;;;;;;;;;;;;;;;;;;;;;;;;;;;          ;
;;;;;;;;;;;;;;;;;;;;;;;;;;;;;;;;;;;;;;;;;;;;;;;;          ;;;;;;;  ;;;;;;  ;;;;;;;  ;;;;;;;  ;

;Calculate  intensity  on  an  AU  map:

rxy  = dindgen(xmax,ymax)                            ;initialize  arrays
Is1  = dindgen(xmax,ymax)
trdust  = dindgen(xmax,ymax)
tr2dust=dindgen(xmax,ymax)

null_flux=0.0
full_flux=0.0

for  x=0,xmax-1  do  begin                           ;for  each  grid  element
  for  y=0,ymax-1  do  begin

    rxy[x,y]  = rcen(x,y,  xcen=xcen,  ycen=ycen,  incrmnt=incrmnt,$
                  ii=ii,  rota=rota)

    Is1[x,y]  = 0.

    for  z = 0.,height+0.01,incrmnt      do  begin

     ;calculate  intensity:
```

```
      Is_add  = 2.* Is(x,y,z,   xcen=xcen,   ycen=ycen,   ii=ii,   rota=rota,   Ts=Ts,$
                        Rstar=Rstar,   Rsun=Rsun,   Temp_1=Temp_1,   h=h,  nu=nu,   c=c,$
                         kk=kk,   inner=inner,   outer=outer,   incrmnt=incrmnt,   mu=mu)$
*incrmnt^3.

      Is1[x,y]   = Is1[x,y]   + Is_add
     endfor

  ;transmitted   fluxes  (in  Jy):
  trdust[x,y]   = Is1[x,y]   * omega  * $
    Tr(x,  xcen=xcen,   pi=pi,   base=base,   lamb=lamb,   AU=AU,   ds=ds,$
       incrmnt=incrmnt)     * 10.^26.
  tr2dust[x,y]   = Is1[x,y]   * omega  * $
    Tr2(x,  xcen=xcen,   pi=pi,   base=base,   lamb=lamb,   AU=AU,   ds=ds,$
       incrmnt=incrmnt)     * 10.^26.

   null_flux   = null_flux   + trdust[x,y]                    ;sum  up  nulled  flux
   full_flux   = full_flux   + tr2dust[x,y]                   ;sum  up  constr.   flux
  endfor
endfor

print,"Null=",null_flux/(full_flux+flux_12)

end
```

REFERENCES

Andre, P., Ward-Thompson, D., & Barsony, M. 2000, Protostars and Planets IV, 59

Artymowicz, P. 1988, ApJL, 335, L79

Augereau, J. C., Lagrange, A. M., Mouillet, D., & Ménard, F. 2001, A&A, 365, 78

Aumann, H. H. 1985, PASP, 97, 885

Aumann, H. H., et al. 1984, ApJL, 278, L23

Backman, D. E. & Paresce, F. 1993, Protostars and Planets III, 1253

Backman, D. E., Werner, M. W., Rieke, G. H., & Van Cleve, J. E. 1997, ASP Conf. Ser. 122: From Stardust to Planetesimals, 49

Backman, D., & Gillett, F. C. 1987, Cool Stars, Stellar Systems and the Sun, 291, 340

Barrado y Navascués, D., Stauffer, J. R., Song, I., & Caillault, J.-P. 1999, ApJL, 520, L123

Beichman, C. A., et al. 2005, ApJ, 626, 1061

Benedict, G. F., et al. 2006, AJ, 132, 2206

Bouwman, J., de Koter, A., Dominik, C., & Waters, L. B. F. M. 2003, A&A, 401, 577

Bracewell, R. N. 1978, Nature, 274, 780

Brusa, G., et al. 2003, Proc. SPIE, 4839, 691

Calvet, N., Patino, A., Magris, G. C., & D'Alessio, P. 1991, ApJ, 380, 617

Chen, C. H., et al. 2006, ApJS, 166, 351

Chen, C. H. & Jura, M. 2003, ApJ, 591, 267

Chen, C. H., & Jura, M. 2001, ApJL, 560, L171

Chiang, E. I., & Goldreich, P. 1999, ApJ, 519, 279

Chiang, E. I., & Goldreich, P. 1997, ApJ, 490, 368

Ciardi, D. R., van Belle, G. T., Akeson, R. L., Thompson, R. R., Lada, E. A., & Howell, S. B. 2001, ApJ, 559, 1147

Cox, A. N. 2000, Allen's astrophysical quantities, 4th ed. Publisher: New York: AIP Press; Springer, 2000. Editedy by Arthur N. Cox. ISBN: 0387987460

Cumming, A., Marcy, G. W., Butler, R. P. 1999. The Lick Planet Search: Detectability and Mass Thresholds. Astrophysical Journal 526, 890-915.

de Zeeuw, P. T., Hoogerwerf, R., de Bruijne, J. H. J., Brown, A. G. A., & Blaauw, A. 1999, AJ, 117, 354

Dominik, C. & Decin, G. 2003, ApJ, 598, 626

Dullemond, C. P. 2002, A&A, 395, 853

Dullemond, C. P., Dominik, C., & Natta, A. 2001, ApJ, 560, 957

Eisner, J. A., Lane, B. F., Akeson, R. L., Hillenbrand, L. A., & Sargent, A. I. 2003, ApJ, 588, 360

Elias, J. H. 1978, ApJ, 224, 857

Fukagawa, M., et al. 2004, ApJL, 605, L53

Gaidos, E. J. 1999, ApJL, 510, L131

Gezari, D. Y., Schmitz, M., Pitts, P. S., & Mead, J. M. 1993, Catalog of Infrared Observations, 3rd ed., NASA Reference Publication 1294.

Gillett, F. C. 1986, ASSL Vol. 124: Light on Dark Matter, 61

Gomes, R., Levison, H. F., Tsiganis, K., & Morbidelli, A. 2005, Nature, 435, 466

Grady, C. A., Woodgate, B., Bruhweiler, F. C., Boggess, A., Plait, P., Lindler, D. J., Clampin, M., & Kalas, P. 1999, ApJL, 523, L151

Greaves, J. S., et al. 2005, ApJL, 619, L187

Greenberg, R., & Nolan, M. C. 1989, Asteroids II, 778

Grun, E., Zook, H. A., Fechtig, H., & Giese, R. H. 1985, Icarus, 62, 244

Haas, M., Leinert, C., & Richichi, A. 1997, A&A, 326, 1076

Hamaguchi, K., Yamauchi, S., & Koyama, K. 2005, ApJ, 618, 360

Hartmann, L., Kenyon, S. J., & Calvet, N. 1993, ApJ, 407, 219

Hatzes, A. P., et al. 2000, ApJL, 544, L145

Herbig, G. H. 1960, ApJS, 4, 337

Hillenbrand, L. A., Strom, S. E., Vrba, F. J., & Keene, J. 1992, ApJ, 397, 613

Hinz, P. M. 2001, Ph.D. Thesis, University of Arizona

Hinz, P. M., Hoffmann, W. F., & Hora, J. L. 2001, ApJL, 561, L131

Hinz, P. M., Angel, J. R. P., Hoffmann, W. F., McCarthy, D. W., McGuire, P. C., Cheselka, M., Hora, J. L., & Woolf, N. J. 1998, Nature, 395, 251

Hoffmann, W. F., Hora, J. L., Fazio, G. G., Deutsch, L. K., & Dayal, A. 1998, Proc. SPIE, 3354, 647

Holland, W. S., et al. 1998, Nature, 392, 788

Hollenbach, D. J., Yorke, H. W., & Johnstone, D. 2000, Protostars and Planets IV, 401

Jayawardhana, R., Fisher, S., Hartmann, L., Telesco, C., Pina, R., & Fazio, G. 1998, ApJL, 503, L79

Jewitt, D. C., & Luu, J. X. 2000, Protostars and Planets IV, 1201

Jura, M., Malkan, M., White, R., Telesco, C., Pina, R., & Fisher, R. S. 1998, ApJ, 505, 897

Kelsall, T., et al. 1998, ApJ, 508, 44

Kenyon, S. J., & Bromley, B. C. 2004, ApJL, 602, L133

Kenyon, S. J., & Bromley, B. C. 2002, ApJL, 577, L35

Kenyon, S. J. & Hartmann, L. 1987, ApJ, 323, 714

Koerner, D. W., Sargent, A. I., & Ostroff, N. A. 2001, ApJL, 560, L181

Lachaume, R., Dominik, C., Lanz, T., & Habing, H. J. 1999, A&A, 348, 897

Lada, C. J. & Adams, F. C. 1992, ApJ, 393, 278

Lagrange, A.-M., Backman, D. E., & Artymowicz, P. 2000, Protostars and Planets IV, 639

Lecavelier des Etangs, A. et al. 2003, A&A, 407, 935

Leinert, C., et al. 2004, A&A, 423, 537

Liu, W. M., Hinz, P. M., Hoffmann, W. F., Brusa, G., Miller, D., & Kenworthy, M. A. 2005, ApJL, 618, L133

Liu, W. M., Hinz, P. M., Meyer, M. R., Mamajek, E. E., Hoffmann, W. F., & Hora, J. L. 2003, ApJL, 598, L111

Luu, J. X. & Jewitt, D. C. 2002, ARA&A, 40, 63

Macintosh, B. A., Becklin, E. E., Kaisler, D., Konopacky, Q., & Zuckerman, B. 2003, ApJ, 594, 538

Malfait, K., Waelkens, C., Waters, L. B. F. M., Vandenbussche, B., Huygen, E., & de Graauw, M. S. 1998, A&A, 332, L25

Malhotra, R., Duncan, M. J., & Levison, H. F. 2000, Protostars and Planets IV, 1231

Mamajek, E. E., Meyer, M. R., Hinz, P. M., Hoffmann, W. F., Cohen, M., & Hora, J. L. 2004, ApJ, 612, 496

Mamajek, E. E., Meyer, M. R., & Liebert, J. 2002, AJ, 124, 1670

Mannings, V. & Sargent, A. I. 1997, ApJ, 490, 792

Marinas, N., et al. 2006, accepted ApJ, astro-ph #0609119

Marsh, K. A., Van Cleve, J. E., Mahoney, M. J., Hayward, T. L., & Houck, J. R. 1995, ApJ, 451, 777

Mathis, J. S., Rumpl, W., & Nordsieck, K. H. 1977, ApJ, 217, 425

Meeus, G., Waters, L. B. F. M., Bouwman, J., van den Ancker, M. E., Waelkens, C., & Malfait, K. 2001, A&A, 365, 476

Metchev, S. A., Hillenbrand, L. A., & White, R. J. 2003, ApJ, 582, 1102

Millan-Gabet R., Malbet, F., Akeson, R., Leinert, C., Monnier, J., & Waters, R. 2006, Protostars and Planets V.

Millan-Gabet, R., Schloerb, F. P., & Traub, W. A. 2001, ApJ, 546, 358

Miroshnichenko, A., Ivezić , Ž., Vinković , D., & Elitzur, M. 1999, ApJL, 520, L115

Moerchen, M. M., Telesco, C. M., Packham, C., & Kehoe, T. J. J. 2007, ApJL, 655, L109

Moro-Martín, A., Wolf, S., & Malhotra, R. 2005, ApJ, 621, 1079

Moro-Martín, A., & Malhotra, R. 2003, AJ, 125, 2255

Natta, A., Prusti, T., Neri, R., Wooden, D., Grinin, V. P., & Mannings, V. 2001, A&A, 371, 186

Natta, A., Grinin, V., & Mannings, V. 2000, Protostars and Planets IV, 559

Pantin, E., Lagage, P. O., & Artymowicz, P. 1997, A&A, 327, 1123

Pantin, E., Waelkens, C., & Lagage, P. O. 2000, A&A, 361, L9

Perryman, M. A. C., et al. 1997, A&A, 323, L49

Pollack, J. B., Hollenbach, D., Beckwith, S., Simonelli, D. P., Roush, T., & Fong, W. 1994, ApJ, 421, 615

Press, W. H., Teukolsky, S. A., Vetterling, W. T., & Flannery, B. P. 1992, Cambridge: University Press, —c1992, 2nd ed.

Rieke, G. H., et al. 2005, ApJ, 620, 1010

Silverstone, M. D. 2000, Ph.D. Thesis

Spangler, C., Sargent, A. I., Silverstone, M. D., Becklin, E. E., & Zuckerman, B. 2001, ApJ, 555, 932

Strom, S. E., Strom, K. M., Yost, J., Carrasco, L., & Grasdalen, G. 1972, ApJ, 173, 353

Su, K. Y. L., et al. 2005, ApJ, 628, 487

The, P. S., de Winter, D., & Perez, M. R. 1994, A&AS, 104, 315

van den Ancker, M. E., de Winter, D., & Tjin A Djie, H. R. E. 1998, A&A, 330, 145

Vinković, D., Ivezić, Ž., Jurkić, T., & Elitzur, M. 2006, ApJ, 636, 348

Vinković, D., Ivezić, Ž., Miroshnichenko, A. S., & Elitzur, M. 2003, MNRAS, 346, 1151

Waelkens, C., et al. 1996, A&A, 315, L245

Walker, G. A. H., Walker, A. R., Irwin, A. W., Larson, A. M., Yang, S. L. S., & Richardson, D. C. 1995, Icarus, 116, 359

Weinberger, A. J., Becklin, E. E., & Zuckerman, B. 2003, ApJL, 584, L33

Wildi, F. P., Brusa, G., Riccardi, A., Lloyd-Hart, M., Martin, H. M., & Close, L. M. 2003, Proc. SPIE, 4839, 155

Wilner, D. J., Holman, M. J., Kuchner, M. J., & Ho, P. T. P. 2002, ApJL, 569, L115

Wuchterl, G., Guillot, T., & Lissauer, J. J. 2000, Protostars and Planets IV, 1081